

TEM₀₀ mode power scaling in specialty fibers

Von der Fakultät für Mathematik und Physik
der Gottfried Wilhelm Leibniz Universität Hannover
zur Erlangung des Grades

Doktor der Naturwissenschaften
Dr. rer. nat.

genehmigte Dissertation

von

Dipl.-Phys. Malte Karow
geboren am 25.06.1983 in Stadthagen

2013

Referent: Prof. Dr. Karsten Danzmann, Leibniz Universität Hannover
Korreferent: Prof. Dr. Uwe Morgner, Leibniz Universität Hannover

Tag der Promotion: 13.12.2013

Kurzzusammenfassung

Das wesentliche Ziel dieser Arbeit war es, die Herausforderungen bei der Entwicklung von Faserverstärkersystemen für die nächste Generation von Gravitationswellendetektoren (*engl.*: gravitational wave detector, GWD) zu identifizieren und zu verstehen. Obwohl die Laserparameter bis jetzt noch nicht endgültig festgelegt sind, lassen konzeptionelle Arbeiten auf die Verwendung eines linear polarisierten, einrequenten Signals bei einer Wellenlänge von 1064 nm mit ca. 1 kW optischer Leistung in der TEM₀₀-Mode schließen. Die größte Schwierigkeit, ein solches Signal mit faserbasierten Systemen bereit zu stellen, besteht darin, dass einmodige Lichtführung und -verstärkung in konventionellen Stufenindexfasern nur bis zu Modenfelddurchmessern (*engl.*: mode field diameter, MFD) von ca. 21 µm bei 1064 nm möglich ist. Verstärkung von einrequenten Signalen in solchen Fasern ist jedoch durch den Prozess der stimulierten Brillouin-Streuung (*engl.*: stimulated Brillouin scattering, SBS) auf Leistungen bis zu 300 W begrenzt. Die vorliegende Arbeit konzentriert sich daher auf die alternativen Faserkonzepte der photonischen Kristallfasern (*engl.*: photonic crystal fiber, PCF) und der chiral Kern-gekoppelten (*engl.*: chirally coupled core, CCC) Fasern. Diese waren und sind die vielversprechendsten Kandidaten für den effektiv einmodigen Betrieb von Fasern mit sehr großen MFDn.

Durch Verwendung einer PCF mit einem MFD von 30 µm wurde eine Rekordleistung von 203 W in der TEM₀₀-Mode in linearer Polarisation erzielt, nur limitiert durch parasitäre Laserprozesse. Der Überlapp des Kernsignals mit der TEM₀₀-Mode betrug in diesem Fall 91 %. Ein exzellenter TEM₀₀-Modenüberlapp von 95 % wurde für eine CCC-Faser mit einem MFD von 30 µm bei Verstärkerleistungen bis zu 103 W gemessen. Dies zeigt das generelle Potential dieses Faserkonzepts, falls sich der Herstellungsprozess hinsichtlich Performance-Reproduzierbarkeit und -Homogenität entlang der gesamten Faser entsprechend optimieren lässt. Das verwendete Faserstück führte jedoch eine höhere Mode und die Leistung mit linearer Polarisation in der TEM₀₀-Mode war durch den Effekt der transversalen Modeninstabilität (*engl.*: transverse modal instabilities, TMI) auf 182 W begrenzt.

Ein entscheidender Beitrag zur Identifikation verschiedener zu TMI führender physikalischer Prozesse, die zur Zeit noch kontrovers diskutiert werden, wurde durch TMI-Charakterisierung mit verschiedenen experimentellen Methoden geleistet. Unterhalb der Schwellleistung für TMI wurde kein signifikanter Abfall des TEM₀₀-Modengehalts mit steigender Verstärkerleistung festgestellt, sobald transiente Strahlprofilfluktuationen abgeklungen waren. Des Weiteren wurden zum ersten Mal frequenz aufgelöste Intensitätsrauschspektren unterhalb und oberhalb der Schwellleistung direkt gemessen. Dabei wurde ein ansteigendes, breitbandiges Rauschen beobachtet, das keine eindeutigen, ausgeprägten Frequenzen enthielt. Mit steigender Verstärkerleistung wiesen die Rauschspektren immer neue, höhere Frequenzanteile auf.

Obwohl die Eigenschaften der SBS im Vergleich zur TMI sehr gut verstanden sind, erschwert SBS immer noch die Verstärkung von einrequenten Signalen. Deshalb wurde der Einfluss von verstärkter spontaner Emission, der zuvor noch nicht untersucht worden war, numerisch und experimentell evaluiert. Insgesamt stellen die in dieser Arbeit präsentierten Experimente und Diskussionen einen entscheidenden Beitrag zur Entwicklung von Faserverstärkern für die nächste Generation von GWD Systemen dar.

Schlagerworte: Ytterbium Faserverstärker, einrequent, große Modenfelddurchmesser

Abstract

The main subject of this thesis was the identification and comprehension of the challenges arising from designing fiber amplifier systems for application in the 3rd generation of gravitational wave detectors (GWDs). Even though the actual requirements on the laser systems for these future GWDs are not ascertained yet, conceptual design studies indicate that a linearly-polarized single-frequency (SF) signal at 1064 nm with more than 500 W in the TEM₀₀ mode will most likely be required. The major challenge in achieving this arises from the fact that conventional step-index fibers can only be operated effectively single-mode up to mode field diameters (MFD) of about 21 μm at 1064 nm. SF-amplifiers employing these fibers are in turn limited to output power levels of less than 300 W by the nonlinear effect stimulated Brillouin scattering (SBS). The focus of the presented research was therefore on the utilization of advanced fiber design concepts, bendable photonic crystal fibers (PCF) and chirally coupled core (CCC) fibers, as they were and still are the most promising candidates to obtain effective single-mode operation of large mode area fibers.

A record TEM₀₀ mode power in linear polarization was obtained with a PCF of about 30 μm MFD, limited only by parasitic lasing processes. The overlap of the fiber core signal with the TEM₀₀ mode in this case was measured to be 91 %. An excellent overlap of the fiber's fundamental mode with the TEM₀₀ mode (95 %) was demonstrated at power levels up to 103 W for a 30 μm MFD CCC fiber, showing the general potential for this fiber design, if the drawing process can be sufficiently optimized regarding the performance reproducibility and homogeneity along the entire fiber length. The analyzed fiber sample, however, guided one higher order mode, which could not be suppressed anymore at a certain power level. TEM₀₀ mode power scaling in linear polarization was thus limited to 182 W by the onset of a nonlinear effect, commonly referred to as transverse modal instabilities (TMI).

A major contribution to identify various physical processes leading to TMI, which are currently still controversially discussed within the scientific community, was achieved by characterizing TMI with different experimental methods. Below the TMI threshold, no relevant decrease in the TEM₀₀ mode content with increasing amplifier power was observed, once initial beam profile fluctuations had decayed. Moreover, the frequency resolved intensity noise spectra below and above the threshold were measured for the first time directly. A rising broadband noise which contained no distinct frequencies was observed with increasing amplifier power. Moreover, the measured noise spectra contained more and more higher frequencies with increasing amplifier output power.

Even though the process of SBS is well understood compared to TMI, it still aggravates power scaling of SF signals. Hence, a feature which has not been investigated before, namely the impact of amplified spontaneous emission, was evaluated numerically and experimentally. Altogether, the experiments and discussions presented in this thesis largely contribute to the design of fiber amplifier systems for the 3rd generation of gravitational wave detectors.

Keywords: ytterbium fiber amplifier, single-frequency, large mode area

Contents

1	Introduction	1
2	Fundamentals of single-frequency ytterbium-doped fiber amplifiers	5
2.1	General properties of optical fibers	5
2.1.1	Fiber composition and manufacturing	5
2.1.2	Signal transmission losses of optical fibers	7
2.1.3	Fiber modes	9
2.1.4	Polarization mode dispersion and polarization-maintaining fibers	12
2.1.5	Ytterbium-doped fibers	14
2.2	Stimulated Brillouin scattering	17
2.3	Large mode area double-clad fibers	23
2.3.1	Photonic crystal fibers	25
2.3.2	Chirally coupled core fibers	30
2.4	Conclusion	33
3	The impact of ASE on Brillouin scattering of a single-frequency signal	35
3.1	Numerical SBS-threshold calculations of a single-frequency amplifier	36
3.2	ASE counter-propagating to a SF signal in a passive fiber	38
3.2.1	Experimental setup	39
3.2.2	Measurement method and results	40
3.3	SBS threshold measurements on a fiber amplifier with added ASE	43
3.3.1	Experimental setup	44
3.3.2	Measurement method and results	44
3.4	Conclusion	46
4	Beam quality characterization of single-frequency signals	49
4.1	Beam quality measurement methods	49
4.2	Fundamental Gaussian mode content of passive double-clad LMA fibers	50
4.2.1	Standard step-index fibers	51
4.2.2	Photonic crystal fiber	53
4.2.3	Chirally coupled core fiber	56
4.2.4	Conclusion	58
4.3	Beam quality degradation and transverse modal instabilities of amplified signals	59
4.3.1	Transverse modal instabilities (TMI)	60
4.3.2	TMI characterization methods	71
4.3.3	Comparison to other experimental and numerical works	76
4.3.4	Conclusion	80

5	Fundamental mode content of single-frequency ytterbium-doped fiber amplifiers	83
5.1	PM LMA photonic crystal fiber amplifier	84
5.1.1	Fiber geometry	84
5.1.2	Experimental setup	84
5.1.3	Amplifier characterization	87
5.2	Amplifiers with CCC fibers	92
5.2.1	37 μm core diameter fibers	92
5.2.2	55 μm core diameter fibers	98
6	Conclusion and outlook	103
	List of acronyms	107
	Bibliography	109
	Publications in peer-reviewed journals	126
	Publications in conference proceedings	127
	Curriculum vitae	129

1 Introduction

Gravitational waves are a consequence of Albert Einstein's general theory of relativity from 1916 [1]. Their direct detection would revolutionize the field of astronomy and the understanding of the early universe. This arises from the fact that cosmological events could be detected that are impossible to be observed with traditional astronomy. To date, all astronomic measurement techniques are based on the detection of electromagnetic waves, but the early universe was opaque to electromagnetic radiation [2]. Furthermore, gravitational waves are the only way to directly observe black holes as they are the only radiation emitted with sufficient strength [3]. Besides, gravitational waves do not get scattered significantly by any kind of matter, unlike electromagnetic radiation [3, 4].

As gravitational waves are ripples in the curvature of space-time, tidal forces are exerted on masses in the path of the wave [5]. These strain-forces manifest themselves as periodic decrease and increase of the distance between two free objects with a frequency corresponding to that of the wave. The major detection challenge arises from the fact that the strength of the space-time distortion does not only depend on the mass of the source object, but is inversely proportional to the distance between source and observer. When detected on the earth, these strains are in the order of magnitude of less than 1 part in 10^{20} [4]. This corresponds to a maximum relative length change in the order of 10^{-17} m, if a detector baseline of 10^4 m is considered [4].

The frequency of the gravitational waves depends strongly on the source and can exist at frequencies within several bands between 10^{-16} Hz and 10^3 Hz [4]. To measure local space-time distortions by colliding neutron stars or black holes, direct detectors such as the "Laser Interferometer Gravitational-Wave Observatory" (LIGO) have been set up [2]. The current LIGO system, which is also referred to as advanced LIGO (aLIGO), belongs to the second generation of gravitational wave detectors (GWDs). It reaches a strain sensitivity between 10^{-23} Hz $^{-1/2}$ and 10^{-21} Hz $^{-1/2}$ in the frequency range of about 10 Hz to 10 kHz [6]. It is based on a Michelson type interferometer with arm lengths of 4 km [7], and requires the injected signal to be single-frequency with low fluctuations of power as well as frequency, low beam pointing fluctuations, one fixed polarization state and to contain only the TEM $_{00}$ mode [8]. To fulfill these requirements, a nonplanar ring oscillator (NPRO) [9] would be the ideal laser source as it emits a pure TEM $_{00}$ mode signal with a linewidth of about 1 kHz and the emitted elliptical polarization can be easily converted into linear polarization. The laser medium of the NPRO is a Nd:YAG crystal and the emitted wavelength is thus 1064 nm. Even though the intensity and frequency noise levels of the free-running NPRO are well above the requirements for a GWD system, the desired levels have been achieved with external stabilization methods [8].

Besides these advantageous properties of the NPRO as seed oscillator, it has a major drawback. Power levels of only up to 2 W can be directly extracted. Unfortunately, the sensitivity of the Michelson interferometer is limited by shot-noise, which decreases

proportional to the square-root of the laser power [5]. Thus, the emitted signal needs to be amplified before being injected into the interferometer to achieve the required measurement sensitivity. The TEM₀₀ mode power level required for the current generation of GWDs such as the advanced LIGO system was about 165 W in front of the interferometer [10]. It was achieved by preamplification of the NPRO signal to about 35 W in a master-oscillator power-amplifier (MOPA) based on Nd:YVO₄ crystals. Finally, the signal was injection-locked to a Nd:YAG high-power oscillator [11].

For the 3rd generation of gravitational wave detectors, the actual requirements on the laser systems are not ascertained yet, but conceptual design studies have been laid out. Targeted major improvements are the reduction of thermal noise compared to the aLIGO system and the decrease of the lower observation frequency limit to 1 Hz. To meet these objectives, the European project “Einstein Telescope” (ET) considers a xylophone configuration, simultaneously deploying a high- and a low-frequency detector [6]. As the ET would still be an interferometer-based detector, the demanded laser signal would as for the second generation GWDs have to be single-frequency with very low power- and frequency-noise, as well as low beam pointing fluctuations. The low-frequency system would operate at 1550 nm and cover observation frequencies between 1 Hz and 50 Hz. Thermal noise reduction in this frequency range would be achieved by deploying cryogenically cooled silicon mirror substrates. To achieve the targeted detector sensitivity, about 3 W of TEM₀₀ mode power in linear polarization would be required behind the interferometer input mode cleaner [12]. The high-frequency laser system would operate as the second generation GWDs at 1064 nm and cover the GW frequency band between 50 Hz and 10 kHz. Significant thermal noise reduction for this detector would be achieved by changing the transverse beam shape to the Lag₃₃ mode [6]. Additionally, a power level of at least 500 W in front of the interferometer is desired to reduce the photon shot noise level [12]. Given the current state of the art, the most likely concept to fulfill these requirements is mode-conversion from a high power TEM₀₀ mode signal. As conversion efficiencies of no more than 70 % have been achieved up to day [13, 14], about 1 kW of SF signal TEM₀₀ mode power at 1064 nm would be required from a potential laser source.

Amplification of a kHz-linewidth-signal to several 100 W with such an excellent beam quality that a high fractional TEM₀₀ mode content is obtained is still a challenge. Further power scaling of the aLIGO laser system is undesirable, as high fractional TEM₀₀ mode power operation was already difficult to achieve [11]. To reduce the system complexity, a MOPA system would be desirable. Especially in the 1 μm wavelength range, fiber-based MOPA systems are a very promising alternative to crystal-based laser systems. Several kilowatt of continuous-wave (CW) output power have been demonstrated with ytterbium (Yb) -doped fiber amplifier systems [15]. However, when amplifying kHz-linewidth signals, one of the major obstacles is the onset of stimulated Brillouin scattering (SBS). To increase the threshold of this nonlinear power-limiting effect, different approaches have been proposed. As the effect depends on the laser intensity in the fiber core, the simplest attempt to increase the SBS threshold power would be to scale up the fiber core diameter and consequently the mode field diameter (MFD) of the fundamental fiber mode.

Unfortunately, conventional step-index fibers can only be operated effectively single-mode up to MFDs of about 21 μm at 1064 nm [16, 17]. Single-frequency (SF) amplifiers employing these fibers are in turn SBS-limited to output power levels of less than 300 W, even if external mitigation techniques are applied [18].

To overcome these limitations, a lot of effort has been put into developing specialty fibers which can be operated effectively single-mode besides their large fundamental mode area. Current power records for different polarization-maintaining (PM) fiber design concepts employed in SF MOPA systems are 402 W for a step-index large mode area (LMA) PM fiber [19], 511 W for a chirally coupled core (CCC) fiber [20], and 494 W for an acoustically segmented photonic crystal fiber (PCF) [21]. All these fiber designs were customized, and are not yet commercially available. They were primarily tested for their SBS threshold, while the beam quality has been investigated in terms of M^2 -measurements. Even though the output beams were found to be near diffraction limited, with M^2 -values between 1.1 [19] and 1.3 [21], a conclusion about the TEM_{00} mode content cannot be drawn. In fact, M^2 -values of < 1.1 still allow for the fraction of higher order mode beam content to be as high as 30 % [22].

By the time the research for this thesis was started, there had been two high power 1 μm master-oscillator fiber-amplifier systems, for which the fractional TEM_{00} mode content had been measured [23, 24]. The amplifier fiber in Ref. [23] was a non-polarization-maintaining PCF by NKT photonics with a MFD of 22 μm . This system consisted of only a single amplification stage, and was pump- as well as seed-power limited. At a maximum output power of 148 W, the TEM_{00} mode content was measured to be 92.6 %. The second amplifier system [24] employed a PM standard step-index fiber with a MFD of approximately 21 μm by Nufern. The TEM_{00} mode overlap was found to be power independent and around 95 %, but the maximum output power was limited by the onset of SBS to 100 W. Discussing the suitability of Yb-doped SF fiber MOPAs as laser sources for the 3rd generation of GWDs, the modal decomposition with respect to the free-space TEM_{nm} modes of amplifier configurations and fibers, capable of further power scaling, needs to be investigated. This is the main subject of the presented thesis. As bendable PCFs and CCC fibers with MFDs of at least 30 μm were and still are the most promising candidates to obtain effective single mode operation of large mode area fiber cores, the research was focused on these advanced fiber designs. Passive and active fiber versions were tested likewise.

During the last 3 years, a new major power scaling limitation of fiber amplifier systems was discovered. A threshold-like onset of transverse modal power transfer occurs at a certain power level, even in fibers that can be operated effectively single mode below this threshold power [25, 26]. In the literature, this effect is now often referred to as modal instabilities [27, 28] or sometimes transverse modal instabilities (TMI) [29] and it is not fully understood, yet. Therefore, experiments investigating some essential fundamentals of this effect were integrated into the work presented here.

These experiments basically focus on exploiting the suitability of two different measurement techniques to characterize the TMI threshold and the dynamics of the process beyond it. In particular it was tested which TMI characteristics could be detected by the

utilization of the nonconfocal scanning ring cavity that is otherwise deployed to decompose beams into the TEM_{nm} mode set. Moreover, the frequency resolved intensity noise spectra below and above the threshold were measured directly for the first time. Finally, in order to prove some aspects of numerical and phenomenological models developed by several research groups within the last two years, additional pump- and seed-amplitude modulation was applied to an amplifier system, exhibiting TMI.

Eventually, threshold power improvement with respect to this effect might counteract provisions to suppress SBS. Hence, SBS is still an issue, at least if a SF signal is supposed to be amplified. Interestingly, the impact of amplified spontaneous emission (ASE) on the threshold power level of a SF amplifier had not been investigated before. Potentially, ASE photons within the Brillouin gain bandwidth (BGBW) and co-propagating to the Brillouin scattered signal can seed the SBS process. If a SF signal is amplified from a few Watts to several 100 W in a fiber amplifier, the ASE power level can be quite high and the proposed process might affect the SBS threshold significantly. The ASE power level can be lowered by reducing the gain factor in the amplifier, i.e. by increasing the seed power. In case of fiber laser systems for a potential application in the ET-GW detector, the utilization of a preamplification stage is then required. This in turn leads to the injection of ASE photons within the BGBW into the high-power amplifier. The Rayleigh-backscattered fraction of these photons can then potentially seed the SBS process in the high-power amplifier stage. Experiments, investigating the explained issues, were also carried out.

This thesis is organized as follows. Chapter 2 gives a brief overview about the essential fundamentals in order to understand the basics of the Rayleigh- and Brillouin scattering processes as well as fiber modal guiding. Special attention is drawn to the working principles of PCFs and CCC fibers. In Chapter 3, the impact of ASE on the Brillouin scattering of a SF signal is analyzed. Chapter 4 comprises of two parts. First, the measurement setup to analyze the TEM_{00} mode overlap of the beams emitted from the fibers under test is briefly described (Section 4.1). Section 4.2 comprises of the results from applying this measurement technique to passive versions of step-index, photonic crystal and CCC fibers. The second part of Chapter 4 deals with the issue of TMI. It starts with an overview about the essential experimental and numerical results as they are today, but also emphasizes the state of the art by the time the experimental work for this thesis, regarding the TMI phenomenon, was started. After the description of these experiments, a detailed discussion of their outcome and relation to other experimental and theoretical works is given. The main subject of this thesis is contained in Chapter 5. Experimental results regarding the TEM_{00} mode power extraction from SF amplifiers, employing bendable LMA PCFs and CCC fibers are presented. Finally, in Chapter 6 an overall conclusion is drawn, regarding a potentially deployed laser system for the 3rd generation of GWDs.

2 Fundamentals of single-frequency ytterbium-doped fiber amplifiers

This Chapter gives an overview about the theoretical background related to the presented work. It provides a brief description of the essential fundamentals. Detailed information on the introduced subjects can be obtained from the referred literature.

The first Section deals with general properties of the simplest optical fiber structure, the single-mode step-index silica fiber. Its composition, fabrication processes, signal transmission loss sources and set of guided modes are presented. Furthermore, some basic properties of Ytterbium-doped fibers are described. In the second Section, the effect of stimulated Brillouin scattering in optical fibers is introduced. This nonlinear scattering process is a major power limitation for the transmission and amplification of single-frequency signals. One attempt to increase the power threshold of this nonlinear effect was to reduce the optical intensity in the fiber cross-section. Three fiber design concepts to achieve large mode field areas while maintaining effective single-mode operation are presented in Section 2.3.

2.1 General properties of optical fibers

2.1.1 Fiber composition and manufacturing

Optical fibers are dielectric waveguides, whose cylindrical symmetry enables transmission of light with excellent beam quality. They consist in general of a signal core, with radius r_{co} and optical refractive index n_{co} , surrounded by a cladding with radius r_{cl} and a slightly smaller optical refractive index n_{cl} [30]. Light-wave guiding in the core of such a structure can be interpreted in the geometric optics approximation as total internal reflection (TIR) of rays at the transition to the cladding, the optically thinner medium [31]. For mechanical stability against external pressure or stress, optical fibers are typically coated with a high refractive index polymer [32]. The cross-section of such a structure is sketched in Fig. 2.1 (a).

For the most common application, pure signal transmission, so-called step-index fibers are deployed. Their name originates from the sharp index-step between core and cladding, schematically shown in Fig. 2.1 (b). One of the most important parameters of an optical fiber is the numerical aperture (NA). It is defined as

$$\text{NA} = \sin \theta_{\text{NA}} = \sqrt{n_{\text{co}}^2 - n_{\text{cl}}^2}, \quad (2.1)$$

where θ_{NA} denotes the maximum angle of acceptance for ray-coupling into the fiber, and depends on the refractive index step between core and cladding [33].

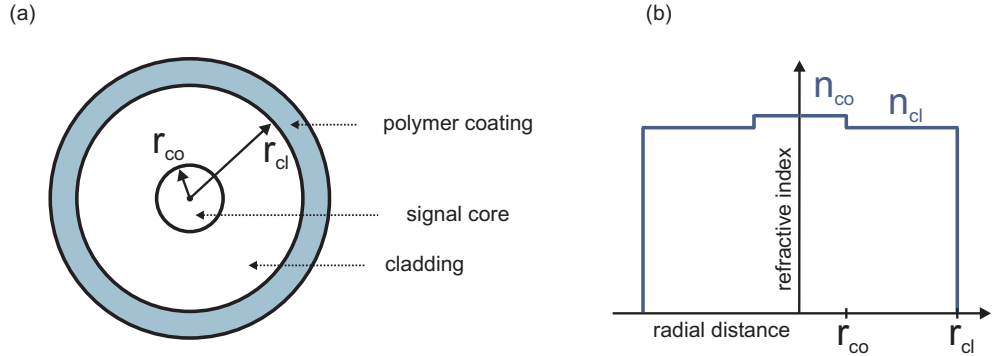


Figure 2.1: Sketch of (a): cross-section and corresponding radial refractive index profile of a step-index fiber, as typically printed in textbooks (e.g. [32]) to visualize the basic concept and geometry of an optical fiber. r_{co} and n_{co} denote the radius and optical index of the signal core whilst r_{cl} and n_{cl} represent the radius and optical index of the cladding. The utilized dimensions do not resemble a real fiber, but are used for visualization purposes only.

The manufacturing process of optical fibers consists of two steps and requires the precise control of the fiber dimensions and refractive indices. In the first step, a cylindrical fiber preform is fabricated, already containing the relative dimensions of core and cladding as well as their refractive indices [32]. The refractive index control is achieved through doping by vapor phase deposition techniques, such as modified chemical vapor deposition (MCVD), plasma-activated chemical vapor deposition (PCVD), outside vapor deposition (OVD) or vapor axial deposition (VAD). Most commonly, the MCVD method is applied. It starts with a hollow silica glass tube, fabricated by fusing SiO_2 molecules [33]. This tube is heated along its entire length and rotated, while gas mixtures containing the molecules for the chemical reactions in the tube's heated zone are injected. The resulting gas particles are then accelerated through thermophoresis towards the tube walls. Usually, pure silica glass layers are deposited first to prevent outside diffusion of loss producing OH-molecules into the reaction area of the tube [33]. For a matched-cladding fiber, the additional deposited cladding layers have the same refractive index as the original silica tube and layers. By bringing molecules such as fluorine or boron into the glass matrix of a cladding layer, it is also possible to produce fibers with a depressed cladding [33].

The fused silica material for the signal core is usually of higher purity, i.e. less contaminated and contains fewer defects as the original outer tube [33]. This ensures lower propagation losses of light guided within such layers. The slightly higher refractive index of the fiber core layers compared to pure fused silica is achieved by bringing in GeO_2 molecules into the glass matrix [32]. For the normalized optical index difference between core and cladding

$$\Delta = \frac{n_{co}^2 - n_{cl}^2}{2n_{co}^2} \quad (2.2)$$

in optical fibers, the weak-guidance approximation

$$\Delta \approx \frac{n_{co} - n_{cl}}{n_{co}} \quad (2.3)$$

is valid [31] and yields typical values around 0.2% for a single-mode fiber [33].

Another dopant that increases the refractive index of pure silica glass is P_2O_5 , but the main purpose of bringing this molecule into the glass-matrix is to reduce the viscosity in the doped layers and the overall vapor deposition temperature. As a first advantage of this, the risk of temperature induced preform distortions is reduced. Moreover, a higher uniformity of the glass layer composition is achieved, yielding a more precise index control [33]. The number of deposited layers depends on the core size and varies between just a few and several tens. It is also possible to alter the refractive indices of the core layers to form graded index fibers for advanced applications [32]. After all layers are deposited at the tube walls, the tube is collapsed in vacuum and under high heat to form a solid preform.

In order to draw the fiber, the preform is vertically placed at the top of a drawing tower, which is at least a few meters high. The glass is molten locally and the fiber diameter can be controlled by real-time measurements and a feedback control loop for the drawing rate and the furnace temperature [33]. The polymer coating is applied in molten form to the already cooled part of the fiber, further down the drawing tower.

2.1.2 Signal transmission losses of optical fibers

Besides enabling a precise control of the core's and cladding's diameter as well as optical refractive index, the production process of an optical fiber needs to account for another challenge. Even though the attenuation per meter in optical fibers is low compared to other waveguides, due to the smoothening of imperfections during the drawing process [34], the signal transmission losses need to be kept as low as possible, as for most applications, at least several meters of fiber are deployed. Loss sources related to the fabrication process are categorized as extrinsic losses to distinguish them from intrinsic losses, arising from fundamental material properties. For signals in the infrared, extrinsic loss sources include e.g. the already mentioned OH-molecules. This loss contributor enters the reaction chamber through diffusion, contamination of the reactant chemicals and leaks in the chemical delivery system [33]. It has a fundamental vibrational resonance at a wavelength of approximately $2.73 \mu\text{m}$, with overtones at $0.95 \mu\text{m}$ and $1.38 \mu\text{m}$. The latter couples to the fundamental vibration mode, yielding an additional sideband at $1.23 \mu\text{m}$ [33]. Even though it is the most difficult loss source to diminish, it is not so critical for the signal wavelength of $1.064 \mu\text{m}$, utilized in the work for this thesis. Other extrinsic loss contributors are transition metals or rare-earth cations.

Intrinsic losses arising from material resonances of fused silica are negligible in the near infrared. Significant absorption occurs only in the ultraviolet region due to electronic

resonances and in the far-infrared beyond $2\ \mu\text{m}$, caused by vibrational modes [32]. Between 970 nm and 1064 nm, the relevant wavelength region for ytterbium (Yb) -doped fiber amplifiers, the main loss mechanism is Rayleigh scattering. It arises from density fluctuations, frozen into the glass matrix of fused silica during the production process [32]. They are related to the fact that the basic unit of SiO_2 consists of a single silicon atom, surrounded by four oxygen atoms, forming a tetrahedra (Fig. 2.2 (a)) [33]. Each of the oxygen atoms is shared by two neighboring tetrahedra, giving rise to a freedom of their relative orientations. While this structure is in thermal equilibrium at elevated temperatures, the rapid cooling of the fiber during the production yields random microscopic density variations, as illustrated in Fig. 2.2 (b). These in turn impose small refractive index variations, scattering light in all directions. In the forward direction, the scattered waves superimpose coherently, leading only to a phase retardation with respect to the incident wave, slowing down its propagation velocity in the fiber [30]. As the light scattered in all other directions has a random phase distribution, its superposition cancels out almost completely [30]. The coherent components of these waves however scatter out of the original propagation direction, yielding power loss of the incident wave.

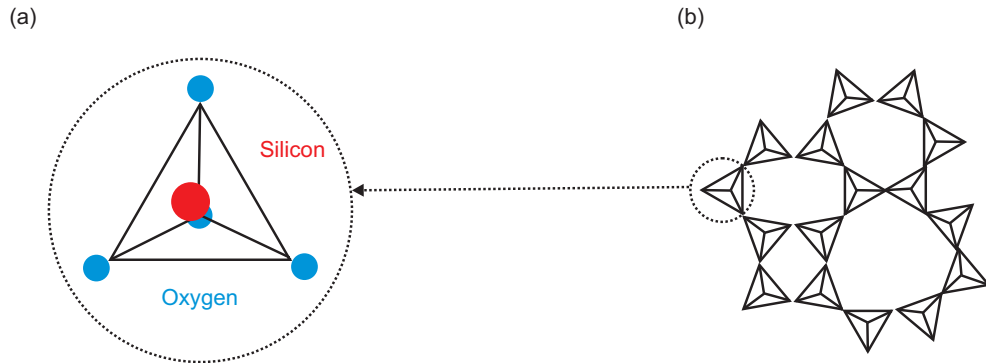


Figure 2.2: (a): Illustration of the basic unit of the SiO_2 molecule, consisting of a silicon atom, surrounded by four oxygen atoms, forming a tetrahedra. (b): All oxygen atoms are shared by two neighboring silicon atoms, giving rise to a freedom in their relative orientation and thus a density variation in the molecular-matrix [33].

As the dimensions of the above described scattering center due to refractive index variations are much smaller than the wavelength under consideration, the classical description of Rayleigh scattering can be applied [35]. It treats the scattering center as an atomic dipole that gets excited by the incident light. The reemitted light has the same frequency as the incident, but it gets radiated in all directions, just as the angular components of the electric and magnetic far-field of a Hertzian dipole [33]. The radiated power density is proportional to the fourth power of the frequency. Hence, the Rayleigh scattering losses in optical fibers increases as λ^{-4} with decreasing wavelength [32]. The same dependence is obtained by a more advanced treatment of Rayleigh scattering, as power loss of a plane wave using the theory of coupled modes [30].

The relation of input power P_{IN} to the transmitted power P_{T} is given by

$$P_{\text{T}} = P_{\text{IN}} \exp(-\alpha L), \quad (2.4)$$

with α being the overall loss coefficient of the fiber at the considered wavelength. This expression can also be used to relate α to the more commonly used loss coefficient in units of dB/km [32],

$$\alpha_{\text{dB}} = -\frac{10}{L} \log\left(\frac{P_{\text{T}}}{P_{\text{IN}}}\right) = 4.343 \alpha. \quad (2.5)$$

A typical value for α_{dB} at a wavelength around $1 \mu\text{m}$ is 1 dB/km [36].

2.1.3 Fiber modes

Optical fibers can guide a finite number of modes over a wide range of frequencies and support additionally a continuum of radiation modes [32]. These modes are distinguished by their propagation constants and spatial electromagnetic field distributions, and differ moreover in the penetration depth of their evanescent field into the cladding [31]. Within a passive fiber this affects the mode confinement in the core and thus the transmission and bending losses [30]. In active fibers, it additionally leads to a different overlap with the doped region and consequently the experienced gain can differ significantly as well. In order to develop fiber laser systems for applications such as GWDs that require the laser power to be contained in one particular cavity mode, i.e. transverse spatial field distribution, it is thus essential to understand the modal properties of optical fibers.

Mathematically, the set of guided modes of a fiber is obtained by solving the Helmholtz-equation for electromagnetic waves in cylindrical coordinates (r, φ, z)

$$\frac{\partial^2 U}{\partial r^2} + \frac{1}{r} \frac{\partial U}{\partial r} + \frac{1}{r^2} \frac{\partial^2 U}{\partial \varphi^2} + \frac{\partial^2 U}{\partial z^2} + n^2 k^2 = 0. \quad (2.6)$$

In this notation, the variable U stands for a Cartesian component of either the electric or the magnetic field, $k = \frac{2\pi}{\lambda}$ is the free-space wavenumber and n denotes the refractive index, either of the core or the cladding [37]. The derivation of Eq. 2.6 from Maxwell's equations can be found in several textbooks [30, 32, 33, 37] and implies some assumptions, holding true for optical fibers, to simplify the mathematical problem. These simplifications include the absence of free charges, no magnetic polarizations and spatial independence of the refractive index. For the induced polarizations, a local medium response is assumed and nonlinear contributions are treated as small perturbations. In standard step-index fibers effects governed by the third-order permittivity χ^3 are assumed to be dominant due to the fiber's cylindrical symmetry [32].

Fourier-transforming Eq. 2.6 and using a separation ansatz yields differential equations, whose solutions are Bessel-functions. By applying appropriate boundary conditions, the

eigenvalue equation for the modes propagation constants β_{qm} is obtained. For guided modes, these boundary conditions are e.g. continuity at the core-cladding boundary and that the field must vanish for $r \rightarrow \infty$. Furthermore, the propagation constant β needs to fulfill [31]

$$n_{\text{cl}} k < \beta < n_{\text{co}} k, \quad (2.7)$$

as only these modes see a refractive index step and can experience TIR. If no further simplifications are considered, their solutions are a general fiber mode set, where each β_{qm} corresponds to a different spatial field distribution [33]. This mode set consists of two-types of hybrid (i.e. electromagnetic) modes that are due to historic reasons labeled as HE_{qm} and EH_{qm} modes [38]. The subscripts q and m are the azimuthal and radial mode numbers, indicating the nodes of the electromagnetic field in the azimuthal and radial direction. For $q=0$, either the electric or the magnetic axial field component vanishes and the resulting modes are analogous to the transverse-electric (TE_{0m}) or transverse-magnetic modes (TM_{0m}) of a planar waveguide [32].

As the weak-guidance condition (Eq. 2.3) is fulfilled in optical fibers, it is reasonable to include this in the mathematical description. This captures a significant characteristic of fiber modes. The general modes become degenerated, i.e. there are at least two linearly-independent transverse mode field distributions to each propagation constant [30]. Hence fiber modes are rather described as composition of super-imposed degenerate modes fields. These mode fields are categorized as linearly-polarized (LP_{lm}) modes, as they have only small longitudinal electric and magnetic field components [31]. In a geometric optics picture this arises from the fact that in order to experience total internal reflection, the waveguide modes have to enter the core-cladding boundary at a very large angle [33].

In order to solve Eq. 2.6 for the transverse mode fields of the LP modes, the separation ansatz

$$U(r, \phi, z) = R(r)\Phi(\phi)e^{-i\beta z} \quad (2.8)$$

can be utilized [37], resulting in differential equations for the azimuthal field amplitude $\Phi(\phi)$ and for the radial field amplitude $R(r)$. Inserting their solutions into Eq. 2.8 yields for the core-region a cos- or sin-like mode field distribution with radially decreasing amplitude. Mathematically this is given by the Bessel functions of the first kind of order l, $J_l(u)$. For the cladding-region, an exponential amplitude-decrease in the radial direction is obtained, mathematically described by the modified Bessel functions of second kind and order l, $K_l(w)$. In order to calculate the propagation constants β_{lm} of the LP modes, the eigenvalue equation

$$u \frac{J_{l-1}(u)}{J_l(u)} = -w \frac{K_{l-1}(w)}{K_l(w)}, \quad (2.9)$$

must be solved [31]. The normalized transverse phase u and the normalized attenuation

constant w are given by

$$u := r_{\text{co}} \sqrt{n_{\text{co}}^2 k^2 - \beta_{lm}^2} \quad w := r_{\text{co}} \sqrt{\beta_{lm}^2 - n_{\text{co}}^2 k^2}. \quad (2.10)$$

Hence, they contain the variation with β and dependence on the wavenumber k , corresponding to the free-space wavelength under consideration $\lambda = \frac{2\pi}{k}$.

The azimuthal mode number of the LP modes l denotes half the number of intensity maxima (or minima) as the azimuthal field amplitude Φ traverses a period of 2π [33]. It is related to the azimuthal mode number of the general modes by [33]

$$l = \begin{cases} 1 & \text{for TE}_{0m}, \text{ TM}_{0m} \\ q+1 & \text{for EH}_{qm} \\ q-1 & \text{for HE}_{qm} \end{cases}. \quad (2.11)$$

The physical significance of m are the number of transverse intensity maxima (or minima) in the radial direction. Thus for every pair (l, m) with $l \geq 1$, two 90° azimuthally rotated field distributions exist. Moreover, the possible field orientations for each LP_{lm} mode give rise to two independent orthogonal polarization states [37].

Mathematically, the subscripts l and m are related to the cut-off conditions for the different LP modes. The value m gives the number of zeros of the quantity $\frac{u}{w}$ in Eq. 2.9 in the interval $[0, V]$, where the parameter V is defined as [33]

$$V = \sqrt{u^2 + w^2} = k \cdot r_{\text{co}} \sqrt{n_{\text{co}}^2 - n_{\text{cl}}^2}. \quad (2.12)$$

Due to its inverse dependence on the wavelength, V is often referred to as normalized frequency [39]. Substituting Eq. 2.1 together with the transverse projection of the free-space wavenumber, $k_{\perp} = k \sin \theta$ into Eq. 2.12 reveals why the V -number carries information about the transverse intensity distribution, as it is simply $V = k_{\perp} r_{\text{co}}$ [39]. From these relations it can be seen that the number of supported modes of one particular fiber depends on its core radius and core-cladding index difference, and for every LP mode a cut-off value V_c can be found. As most applications prefer single-mode emission from of the deployed fibers, the fiber parameters are chosen to achieve

$$V \leq V_c = 2.405, \quad (2.13)$$

which is the cut-off value for the next higher order mode, the LP_{11} . Within $[0, V_c]$, only one solution where $\frac{u}{w}$ is equal to zero in Eq. 2.9 exists, namely the LP_{01} mode [37]. Nevertheless, as Eq. 2.12 is wavenumber dependent, every SM-fiber is still multi-mode for a sufficiently short wavelength.

From Eq. 2.12 it follows that with increasing r_{co} , the index difference between core and cladding needs to decrease in order to obtain a $V \leq 2.405$. Unfortunately, for standard step-index fibers the state-of-the-art manufacturing processes do not allow for an unlimited

index control. The NA of these fibers (Eq. 2.1) is typically limited to 0.06 [40]. For a wavelength of 1064 nm, the core radius of a fiber must therefore be smaller than 7 μm in order to strictly fulfill the single-mode condition.

The transverse field of the fundamental mode can often be approximated by a Gaussian distribution [41]

$$F(x,y) \propto \exp[-(x^2 + y^2)/\omega^2]. \quad (2.14)$$

This enables the calculation of the mode field's effective area [32]

$$A_{\text{eff}} = \frac{(\int \int_{-\infty}^{\infty} |F(x,y)|^2 dx dy)^2}{\int \int_{-\infty}^{\infty} |F(x,y)|^4 dx dy} \quad (2.15)$$

from the beam radius ω as

$$A_{\text{eff}} = \pi \cdot \omega^2. \quad (2.16)$$

If the V -parameter of a given fiber is known and in the range of $1.2 < V < 2.4$, ω can be estimated from the core radius within 1% accuracy by [41]

$$\omega \approx r_{\text{co}} \cdot (0.65 + 1.619 V^{-3/2} + 2.879 V^{-6}). \quad (2.17)$$

2.1.4 Polarization mode dispersion and polarization-maintaining fibers

Even a fiber fulfilling the single-mode condition (Eq. 2.13) is not strictly single-mode, as it can support two orthogonally polarized modes [42]. If a linearly-polarized signal would be launched into a perfectly circular and isotropic fiber, it would remain in its polarization-state [33]. However, real fibers inherit some anisotropies and asymmetries, either induced during the manufacturing process or by fiber bending and twisting. As a consequence, the refractive indices n_x and n_y along these axes become slightly different. The axis with the smaller refractive index is called the fast axis, as the group velocity is larger than for the axis with the higher refractive index [32]. Accordingly, the latter is called the slow axis. The two polarization eigenmodes become nondegenerated, each having a slightly different propagation constant β_x and β_y . This effect is called polarization mode dispersion or modal birefringence. As a measure of its strength, the quantity

$$B_{\text{m}} = \frac{|\beta_x - \beta_y|}{k} = |n_x - n_y| \quad (2.18)$$

was defined [42]. A stronger modal birefringence is accompanied by a shorter beat-length

$$L_{\text{b}} = \frac{\lambda}{B_{\text{m}}} \quad (2.19)$$

between the modes [42], i.e. the periodicity of the modal power transfer. After traveling a distance of L_b , a relative phase shift of 2π between the modes is accumulated. Therefore, the coupling between the modes is most effective, when the average distance between two consecutive perturbations is equal to L_b [33].

In real fibers, B_m and consequently L_b are not constant along the entire fiber length. The power exchange between the two polarization modes occurs therefore in a random fashion, which is intolerable for applications such as interferometric GWDs, where only one fixed linear polarization state can be used. The random power fraction in the other polarization state would be lost.

Nevertheless, polarization-maintaining (PM) fibers can be utilized. Their working principle is based on the following consideration. If sufficient birefringence can be intentionally incorporated between the fast and the slow fiber axis, no coupling to the other mode can be induced by the relative small birefringence perturbations. While conventional fibers typically have beat-lengths in the order of 10 m, acceptable levels of polarization mode coupling were achieved by reducing the beat-length down to about 1 mm [33]. This corresponds to an order of magnitude of the B_m of $\sim 10^{-4}$ [42].

If a linearly polarized signal is launched into one of the principal axes of a PM-fiber, only one polarization mode is excited. The power ratio

$$\eta = \frac{P_y}{P_x} \tag{2.20}$$

of the polarization state excited through mode coupling, P_y , to the launched polarization state P_x , is called polarization cross-talk [43]. Only very little power transfer to the other polarization mode occurs whilst propagating through several 100 meters of fiber length. In fact, cross-talk values of ≥ 30 dB have been achieved by proper fiber design and manufacturing [43, 44].

The necessary birefringence can be achieved by implementing boron-doped stress rods at opposite sides of the signal core into the cladding of the fiber preform. Birefringence due to strain is induced during the drawing process, as the $B_2O_3:SiO_3$ -rods have a different thermal expansion coefficient than the silica cladding [33]. Thus, the value of the obtained B_m depends on the stress-rods shape and increases with their diameter. It is however limited by the offset of the stress-rods from the fiber core, which ranges between 3 and 5 times the core radius [43]. This offset is necessary as $B_2O_3:SiO_3$ exhibits high loss at the transmission wavelength e.g. through OH-ion contamination, even though GeO_2 is typically added to maintain the optical refractive index [43]. Nowadays, a circular symmetric shape, as depicted in Fig. 2.3 (a), is most commonly chosen. It is called PANDA (polarization-maintaining and absorption-reducing fiber [43]) and has prevailed due to the low signal propagation losses compared to other geometries (e.g. bow-tie, elliptical or flat cladding) whilst still acceptable high values of B_m (in the order of magnitude of 10^{-4}) can be obtained [44].

Another method to manufacture a PM-fiber is to introduce shape-birefringence by

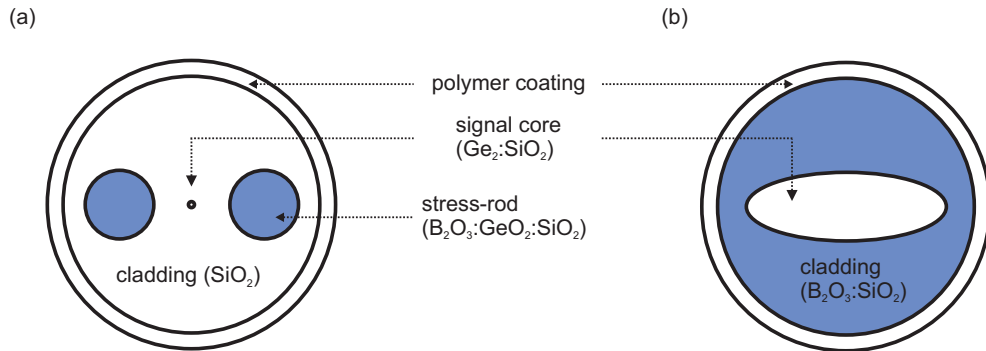


Figure 2.3: (a): The most common PM-fiber geometry is the PANDA-fiber, incorporating two boron-doped circular-symmetric stress-rods, as it combines a sufficiently high amount of induced birefringence and acceptable signal transmission loss [44]. (b): Alternatively to stress-induction, shape-birefringence can be induced, e.g. by an elliptical core. With a B_m of about 10^{-6} the induced amount of birefringence is however two magnitudes lower than for e.g. a PANDA-fiber [32], or the signal transmission loss is intolerable high [44].

fabricating an elliptical core (Fig. 2.3 (b)) [32]. The obtained B_m in this case is however only in the order of magnitude of $\sim 10^{-6}$ [32], corresponding to a beat-length of about 0.5 m [33].

Deviations from the ideal shape of the stress-rods in case of a PANDA fiber or the elliptical core for the shape-birefringence PM-fiber lead to degradation of the polarization-maintenance [44]. Besides this intrinsic factor, there are also some extrinsic issues, degrading the PM-performance. High temperature fluctuations and mechanical perturbations such as too strong bending and twisting can lead to temporal variations in the induced birefringence and thus increase the amount of cross-talk [44].

2.1.5 Ytterbium-doped fibers

One of the great advantages of optical fibers is the possibility to dope the core with laser-active ions. Even with high doping concentrations, the ratio of the doped region to the surface area per unit length is much smaller than for bulk media, yielding much higher thermal damage thresholds [45]. Furthermore, lasers incorporating actively-doped fibers as gain media typically require lower pump power levels compared to bulk systems, e.g. based on laser rods [46]. Another benefit of a fiber-based amplifier or oscillator arises from the fact that their beam quality is determined by the number of guided modes (Subsection 2.1.3). Thus, diffraction limited beam quality can be readily obtained by the utilization of single-mode fibers [47], while for bulk media the geometric parameters of amplifier or oscillator must be carefully chosen [48, 49]. Consequently, fiber lasers and amplifiers started to replace bulk laser media in all applications, where comparable performance in terms of required wavelength, spectral width, average output power, if necessary pulse parameters etc. was achievable [50].

Most commonly, fiber laser sources are utilized, where applications require infrared emission between $1\ \mu\text{m}$ and $2\ \mu\text{m}$ [46, 50]. Within this range there are three major emission bands, achieved by rare-earth ion doping of fused silica. Thulium and Holmium-doped fibers cover the $2\ \mu\text{m}$ spectral region [51, 52], Erbium- or Erbium/Ytterbium-doping yields emission around $1.5\ \mu\text{m}$ [46, 53], and lasing and amplification around $1\ \mu\text{m}$ wavelength is obtained by bringing Neodymium- [46, 53] or Ytterbium-ions [50, 54] into the silica glass matrix. The latter has prevailed due to its simple spectroscopic properties and thus higher optical efficiency compared to the other rare-earth ions [47, 54].

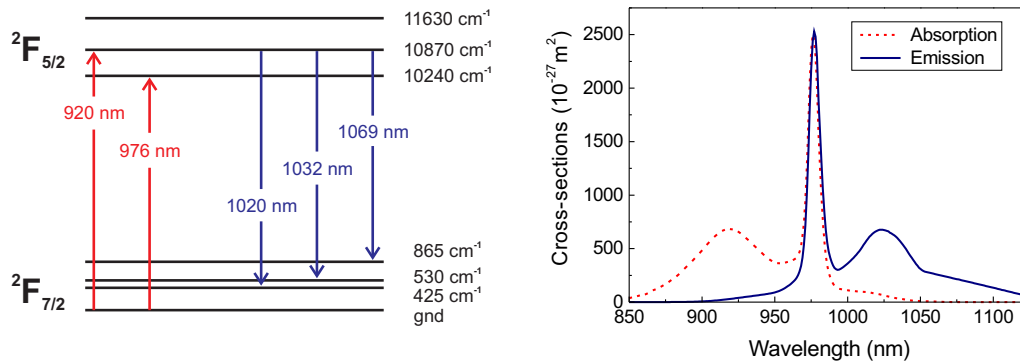


Figure 2.4: (a): Energy levels of Yb-doped silica [55] and (b): Typical absorption and emission cross-sections of Yb-doped silica fibers, as presented in Ref. [54].

Only two level manifolds are relevant for all optical wavelengths. The $^2F_{7/2}$ ground state manifold consists of four sublevels, while the excited state manifold $^2F_{5/2}$ consists of three sublevels (Fig. 2.4(a)) [54]. Nevertheless, instead of discrete peaks in the absorption- and emission spectra, rare-earth doped fibers exhibit broad absorption- and emission bandwidths, even in thermal equilibrium. Typical cross-sections for absorption and emission of Yb-doped silica fibers are depicted in Fig. 2.4(b), whereat the details of the spectra and absolute scaling of the cross-sections depend on the exact composition of the host glass matrix as well as on the Ytterbium-ion concentration [47, 56]. The broad bandwidth of the absorption- and emission-spectra are a consequence of implementing the rare-earth ions into the silica matrix. There are several contributions to this broadening, e.g. the perturbation of the ions' electronic states by presence of the electric fields of the glass-host [46]. This occurs inhomogeneously, as the local surroundings vary from ion to ion. Secondly, the rare-earth ions couple to the quantized lattice vibrations (phonons) of the glass-matrix [57], hence, there is always a slight amount of energy transfer between ion and host-glass. It is quantized for a single ion-phonon pair, but broadens in an ensemble of atoms, as a distribution of phonon energy levels is occupied for a given temperature [46]. Moreover, the electronic states have a finite lifetime (about 0.8 ms for the upper laser-level of a Yb-doped silica fiber [54]), which precludes, according to the energy-time-uncertainty principle, a negligible small energy-bandwidth [35].

For emission in the 1 μm band, most commonly pumping at wavelengths around the 976 nm absorption peak is chosen. As the full width at half maximum (FWHM) bandwidth of this peak is about 10 nm, the utilization of high-power pump diodes with typical emission spectra of 3 nm to 7 nm FWHM is uncritical. Furthermore, slight detuning of the central pump frequency yields the same absorption efficiency. In fact, detuning the pump frequency even to the edges of the absorption peak eventually results in the same absorption efficiency. This effect is caused by ion quenching to a very short lifetime, leading to a strong nonsaturable loss, which also peaks at 976 nm [56]. Another loss mechanism in Ytterbium-fibers is cooperative upconversion, where the energy of two excited Yb^{3+} -ions is combined and one single photon in the green spectral range emitted [58]. Even though this was found to be the main-contributor to the usually clearly visible fluorescence, the gain in the fiber core was found to be negligibly affected by this process at reasonable pump power levels [54]. The other but insignificant source for green fluorescence are Erbium-ion impurities [59]. Blue fluorescence is caused by contamination of the glass matrix with Thulium [60].

In the absence of seed photons, pumping around the 976 nm absorption peak yields a maximum upper state population of 50 %, as the emission cross-section is essentially equal to the absorption cross-section in this wavelength region. The necessary condition to achieve the maximum population inversion is pump power saturation, but for core-pumped standard fibers with core diameters of about 3.4 μm this power level is only about 0.5 mW [54]. The largest gain is now obtained at a wavelength of about 1030 nm. This can be detrimental for the amplification of narrow-linewidth signals at longer wavelengths, where the emission cross-section (Fig. 2.4) is significantly lower.

Spontaneous emission at other than the desired wavelength is unavoidable, as it starts from vacuum noise [57, 61]. Without any guiding mechanisms, the spontaneously emitted photons would be propagating in all directions with a random phase distribution [35, 62]. In active optical fibers, however, the photons whose wave-vectors fulfill Eq. 2.7 will be amplified, while propagating in both directions along the principal fiber axis. This effect is called amplified spontaneous emission (ASE) or fluorescent amplification [62]. Due to the optical waveguiding properties of the fiber, these ASE photons have a large spatial coherence. Their random phase distributions on the other hand yield a low coherence time [63]. This corresponds to a broad bandwidth in the frequency domain [35, 57], and the ASE's spectral shape basically resembles the spectral shape of the emission cross-section as shown in Fig. 2.4 (b) for Ytterbium. Nevertheless, the exact shape of the ASE spectrum of a particular fiber or amplifier strongly depends on parameters such as the pump wavelength and power, as well as fiber length and resulting reabsorption effects.

ASE is a competitive gain effect in fiber lasers and amplifiers and needs to be suppressed for two reasons. First of all, the power contained in the ASE can usually not be utilized in the targeted application of the laser system. Moreover, if the gain becomes too high at a particular wavelength other than the desired one, parasitic laser processes can occur. These often lead to random pulsing of the laser or amplifier, yielding high pulse intensities that can severely damage the fiber and optics nearby, such as coupling lenses. The fiber

end-facets are particularly sensitive to damage through parasitic laser pulses.

2.2 Stimulated Brillouin scattering

Besides the elastic Rayleigh scattering process (Subsection 2.1.3), which is a linear signal power loss mechanism, there are two nonlinear, inelastic scattering processes that significantly limit the maximum signal intensity in an optical fiber. Both processes are interactions of the incoming light with molecular vibrations, governed by the third-order susceptibility $\chi^{(3)}$ [32]. This third-order susceptibility is responsible for the intensity dependence of these processes, as it induces a contribution [32]

$$n_{\text{NL}} = n_2 \cdot |\vec{E}|^2 = n_2 \cdot I_s \quad (2.21)$$

to the refractive index of the material, where n_2 is given by

$$n_2 = \frac{3}{8n_{\text{lin}}} \text{Re} \chi^{(3)}. \quad (2.22)$$

The subscript “NL” denotes the quadratic, thus nonlinear dependence of n_{NL} on the electric field amplitude $|\vec{E}|$, but for practical purposes it is more convenient to express this as linear dependence on the signal intensity I_s . The total refractive index n_s for a signal launched into a silica fiber is the sum of n_{NL} and a material contribution, n_{mat} , which is independent of $|\vec{E}|$. Effects from the second-order susceptibility vanish in silica fibers, as the SiO_2 molecule is symmetric [32].

There are basically two molecular vibrations in the silica matrix of an optical fiber that need to be distinguished as they lead to different interactions with the electric field of the guided light. These vibrations are exemplarily depicted in Fig. 2.5 for a SiO_2 molecule. Fig. 2.5 (a) shows the case, where the atoms constituting the SiO_2 molecule vibrate or rotate in such a way that the electric polarization of the molecule, i.e. its dipole moment changes. This yields an oscillation frequency in the optical range [64]. A photon, scattered at such a rotational or vibrational mode of an individual molecule, experiences a frequency shift of typically about 13 THz in fused silica [32]. This process is called Raman scattering.

The molecular vibrations, associated with the other inelastic scattering process in optical fibers, are sketched in Fig. 2.5 (b). In this case, the atoms of the SiO_2 molecule vibrate in a way that the electric dipole moment does not change and with a frequency in the acoustic range [64]. This results in density variations, moving through the fiber as acoustic waves, and referred to as phonons, i.e. quantized lattice vibrations [64]. This denotation is commonly used, even though a quantum-theoretical description of the light-molecule interaction is only necessary for much lower photon density levels as typically present in an optical fiber [65]. Contrary to the Raman process, photons of the incident light get in this case scattered rather at an ensemble of molecules, i.e. the acoustic wave, and no changes in molecular dipole moments are involved. This process is called Brillouin scattering. The

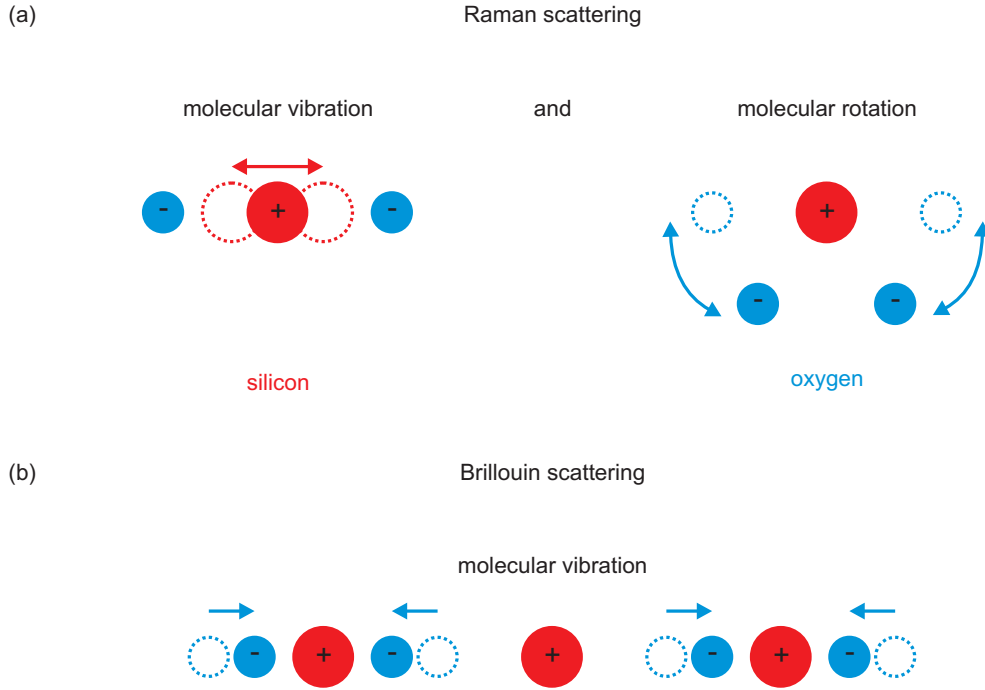


Figure 2.5: Illustration of the two types of molecular vibrations of a three atomic molecule such as SiO_2 , leading to different inelastic interactions with the electric field of incident light. (a): Molecular vibration and rotation associated with Raman scattering. They yield a change in the electric dipole moment and the scattered photon experiences a frequency shift in the optical range. (b): Molecular vibration leading to Brillouin scattering of incident photons. Scattering occurs not at single molecules, but at the traveling wave of density changes in the SiO_2 matrix. The Brillouin frequency shift is in the acoustic range.

frequency shift of the Brillouin scattered photons is three magnitudes lower compared to Raman scattering, corresponds to the frequency of the acoustic wave and can be calculated by [66]

$$\nu_B = \frac{2nv_a}{\lambda_s}. \quad (2.23)$$

With typical values for silica fibers of 1.45 for the refractive index n and 5.96 km/s for the acoustic velocity v_a [32] this yields about 16.2 GHz at a signal wavelength λ_s of 1064 nm. As stated in Ref. [67], the Brillouin gain profile $g(\nu)$ is Lorentzian shaped and can be written as

$$g(\nu) = g_B \frac{(\Delta\nu_B/2)^2}{(\nu - \nu_B)^2 + (\Delta\nu_B/2)^2}, \quad (2.24)$$

with ν being the frequency of the launched signal. Its FWHM $\Delta\nu_B$ has in silica fibers a typical magnitude of less than 100 MHz, while the FWHM of the Raman gain spectrum can extend to several 100 THz [32]. The parameter g_B in Eq. 2.24 is the Brillouin gain coefficient

$$g_B = \frac{2\pi n^7 p_{12}^2}{c\lambda_s^2 \rho_0 v_a \Delta\nu_B}, \quad (2.25)$$

and depends e.g. on material parameters such as the longitudinal elasto-optic coefficient p_{12} and the material density ρ_0 [67]. To illustrate the parameters g_B , $g(\nu)$, $\Delta\nu_B$ and ν_B , Fig. 2.6 schematically shows a Lorentzian-shaped gain profile.

While the Raman peak gain g_R in silica fibers is in the order of magnitude of 10^{-14} m/W, the Brillouin peak gain is about three magnitudes larger [32]. For narrow linewidth signals, SBS is usually the power scaling limitation. As the effective Brillouin gain decreases proportional to a factor $\Delta\nu_s/\Delta\nu_B$ [32], with $\Delta\nu_s$ being the signal bandwidth, power scaling of very broadband signals is rather limited by SRS. Naturally, whether power scaling of a system is limited by SBS or SRS depends on the exact values of g_R , g_B , $\Delta\nu_B$ and $\Delta\nu_s$.

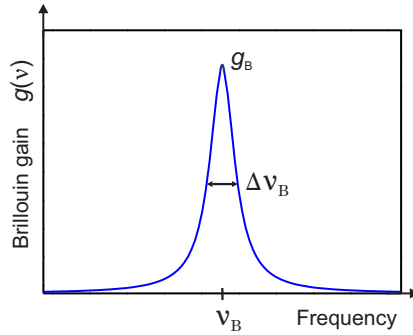


Figure 2.6: Lorentzian-shaped Brillouin gain profile $g(\nu)$ versus frequency, with a full width at half maximum (FWHM) bandwidth of $\Delta\nu_B$ and a maximum Brillouin gain coefficient g_B , centered around the Brillouin shift frequency ν_B .

At low launched signal photon densities, the BS process occurs spontaneously. Some phonons are thermally excited and get annihilated, i.e. the incoming photon absorbs the energy of the lattice vibration, and the scattered photon experiences an Anti-Stokes frequency shift towards a higher frequency [65]. If the scattered photon gets Stokes shifted, a new phonon is generated. In thermal equilibrium at room temperature, the first excited phonon state is only slightly populated, so that the Stokes signal peak in a measured optical spectrum has typically a higher intensity than the Anti-Stokes component [65].

As the thermally excited phonons are random in phase, the scattered photons are incoherent [64]. For the Stokes-light generating case, the process can, nevertheless, become stimulated as the intensity of the incoming light is increased. The induced phonons act as scattering centers themselves, but the photons scattered from these centers are now

in phase with the originally scattered photons. As this process recurs, the emission of Brillouin-scattered photons gets stimulated. The exact definition of the threshold power for the stimulated process is ambiguous in the literature, however, the Brillouin scattered power fraction increases exponentially until all signal photons get scattered.

To describe the phonon induction, a semi-classical model is usually deployed. The electric-fields of the incoming and scattered photons interfere, yielding an electro-magnetic wave with intensity maxima and minima at half the beat frequency. This creates density fluctuations, i.e. a traveling refractive index grating with a period corresponding to the phonon frequency through the process of electrostriction [33]. In this way, new phonons are generated, which coherently couple to the electric-field of the incoming light wave through the third-order polarization [65].

As a consequence of energy and momentum conservation, SBS mainly occurs in the backward direction [33]. Conservation of momentum requires

$$\vec{k}_p = \vec{k}_s - \vec{k}_{BS} \quad (2.26)$$

for the wave-vectors of the phonon \vec{k}_p , the signal photon \vec{k}_s and the Brillouin scattered photon \vec{k}_{BS} , and from energy conservation it follows that [64]

$$k_p^2 = k_s^2 + k_{BS}^2 - 2k_s k_{BS} \cos \Theta. \quad (2.27)$$

Since the acoustic phonon frequency $\omega_p = \frac{ck_p}{n_s}$ is much smaller than the optical frequencies of the signal and Brillouin scattered photons, $\omega_s = \frac{ck_s}{n_s}$ and $\omega_{BS} = \frac{ck_{BS}}{n_s}$, $n_{BS} \cong n_s$ and $\omega_s \gg \omega_p$ can be assumed. This yields from Eq. 2.27 [64]

$$\theta = \begin{cases} 0^\circ & \text{(forward-scattering)} & k_p = \frac{n_s \omega_p}{c} \\ 180^\circ & \text{(backward-scattering)} & k_p = 2\frac{n_s \omega_s}{c} = 2k_s \end{cases}. \quad (2.28)$$

Hence, the magnitude of k_p is extremely small for $\Theta = 0^\circ$, i.e. forward scattering. It maximizes on the other hand for the backward direction, corresponding to $\Theta = 180^\circ$. The relationship between the wave-vectors is illustrated in Fig. 2.7.

To describe the SBS process mathematically, the simplest model considers plane-wavefronts of the incident and the Brillouin scattered beam and therefore neglects transverse derivatives [65]. For continuous-wave (CW) or quasi-CW signals, the steady-state approximation is valid [32], and the SBS dynamics can be described by the two coupled differential equations

$$\frac{dI_s}{dz} = -g_B I_s I_{BS} - \alpha I_s. \quad (2.29)$$

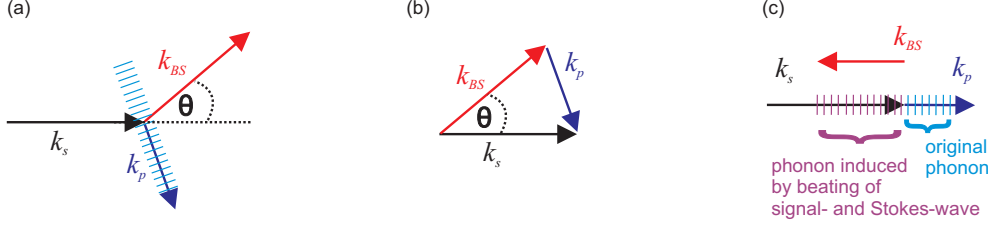


Figure 2.7: (a): A signal-photon with corresponding wave-vector \vec{k}_s gets scattered at an acoustic phonon (\vec{k}_p), yielding the emission of a Stokes-scattered photon (\vec{k}_{BS}). (b): Illustration of the wave-vector relations, required by conservation of momentum. (c): Wave-vector orientations for backward-scattering, which is the relevant direction in optical fibers. Beating of the counter-propagating signal- and Stokes-waves induces new phonons that act as new scattering centers [64, 65].

and

$$\frac{dI_{BS}}{dz} = -g_B I_{BS} I_s + \alpha I_{BS}. \quad (2.30)$$

Here, I_s is the intensity of the launched signal, while I_{BS} abbreviates the intensity of the Brillouin scattered Stokes light. The parameter α accounts for all intrinsic fiber losses. In the undepleted pump limit, which is valid for small fractions of Brillouin scattered light and usually applied to estimate the Brillouin threshold power, Eq. 2.29 can be solved by $I_s(z) = I_s(0)e^{-\alpha z}$ [32]. Applying this solution to Eq. 2.30 and integrating over the fiber length L yields

$$I_{BS}(0) = I_{BS}(L) \exp(g_B P_0 L_{\text{eff}} / A_{\text{eff}} - \alpha L) \quad (2.31)$$

for the Stokes power at the fiber signal input $z=0$. A_{eff} is the effective mode area as defined in 2.16 and $P_0 = I_s(0)A_{\text{eff}}$. The fiber length relevant for the nonlinear interaction is called the effective fiber length L_{eff} and is defined as [32]

$$L_{\text{eff}} = \frac{1 - e^{-\alpha L}}{\alpha}. \quad (2.32)$$

It corresponds to the length over which a signal would propagate through the fiber if it had a constant amplitude over that length and zero amplitude beyond [68].

A general characterization of a fiber's intrinsic Brillouin scattering properties is typically obtained with a pump-probe method [43, 67, 69]. This yields parameters that only depend on the material composition and the signal wavelength, such as the shape and bandwidth of the Brillouin gain spectrum, as well as the Brillouin shift frequency (Eq. 2.23). For passive fibers, the Brillouin gain coefficient g_B (Eq. 2.25) and the effective Brillouin gain $g(\nu)$ (Eq. 2.24) can easily be calculated from these measurements.

Active fibers, however, bear some challenges, as all launched signals experience some degree of amplification and/or absorption. Even though only low power levels are deployed for pump-probe measurements, the exact value for the absolute Brillouin gain cannot be measured. Therefore, additional measurements and numerical modeling of the SBS process are usually carried out for SF amplifier operation. The Brillouin gain is then iteratively obtained by comparing the numerically calculated threshold powers to the measured results. To provide sufficient data, the SBS threshold can be determined for different seed power levels, fiber lengths and pump schemes, as they all influence the threshold power. The onset of SBS is typically monitored by measuring the evolution of the total backscattered power [19, 70, 71], the Brillouin peak in the backward detected optical spectrum [23, 72, 73] and the relative intensity noise at the amplifier output with increasing signal power [74–76].

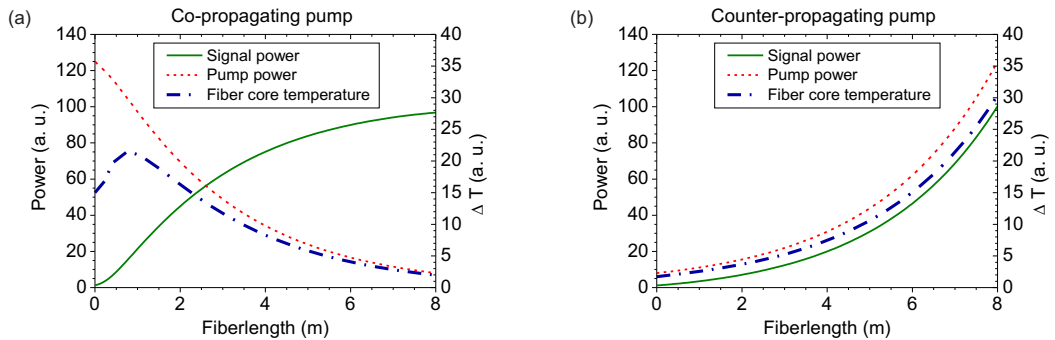


Figure 2.8: Schematic evolution of the signal-, pump-power as well as the fiber core temperature of a (a): co-pumped and (b): counter-pumped fiber amplifier. The curves do not represent a particular amplifier configuration, but are adapted from Ref. [77, 78] for illustration purposes only.

The dependence of the SBS threshold power on the fiber length can be directly anticipated from Eq. 2.31. It is also straight forward to see, why a counter-pumped amplifier has a higher SBS threshold than a co-pumped system. As illustrated in Fig. 2.8 (a), the signal amplification for the co-pumping scheme is highest towards the seed input fiber end. Consequently, the signal propagates with a high intensity through a long part of the fiber. In the counter-pumped case (Fig. 2.8 (b)), the signal experiences the highest amplification towards the output end of the fiber, and the propagation distance with high intensity is comparably smaller. Additionally, the counter-signal pumping yields a stronger temperature gradient than the co-pumped amplifier. A change in temperature in turn is accompanied by a change in the acoustic velocity v_a . The latter affects the Brillouin gain g_B (Eq. 2.25) as well as the Brillouin shift frequency ν_B (Eq. 2.23). As a result, more phonon frequencies can potentially participate in the stimulated process along the whole fiber length and the fiber’s overall Brillouin gain spectrum broadens [67, 79, 80]. For a sufficiently strong temperature gradient, the Brillouin scattered photons from the amplifier output end are incoherent with the photons that get scattered at positions towards the

seed end. Thus, they cannot seed the stimulated process at these positions and the overall threshold power is eventually decreased.

This spectral broadening, caused by a temperature gradient along the fiber, is also experienced by the Stokes spectrum, emitted in the backward direction of the fiber. In the absence of a temperature gradient, on the other hand, the backscattered Stokes spectrum experiences gain narrowing. Eventually, the gain narrowing effect outbalances the spectral broadening of the Stokes spectrum due to a temperature gradient in amplifier operation and the Stokes spectrum might even change its shape from a Lorentzian to a Gaussian [78].

Naturally, the actual effect of a temperature gradient on the Brillouin gain spectrum, the SBS threshold power, as well as the backscattered Stokes spectrum depends strongly on the exact amplifier configuration. Nevertheless, most of the external and internal SBS mitigation techniques rely on modifying the Brillouin gain spectrum in terms of broadening it or the generation of several small resonance peaks that do not overlap with each other. Established external mitigation schemes besides the temperature gradient [76–78] are temperature segmentation [81, 82] and the application of a strain distribution [83, 84]. Internal mitigation techniques pertain the glass composition to obtain a variation in the acoustic velocities either in the longitudinal [70, 85] or the transverse fiber direction [86, 87].

The influence of the seed power, however, is two-sided. If a higher seed power level is used to obtain a certain amount of amplifier output, the overall gain in the fiber reduces. Therefore, the backward propagating Stokes signal experiences lower amplifier gain, abetting a higher SBS threshold. On the other hand, the temperature gradient due to the high gain is reduced, which counter-acts a threshold power increase. Nevertheless, the signal intensity at the seed end can become eventually as high as for the co-pumped case, also reducing the power threshold. The third amplifier parameter that gets influenced by the seed power level is the amount of generated ASE. This broadband noise is emitted in both fiber amplifier directions and the backward propagating photons with frequencies within the Brillouin gain bandwidth might seed the SBS process. An experimental and theoretical investigation had not been carried out before and was part of the work for this thesis. The results are presented in Chapter 3.

2.3 Large mode area double-clad fibers

One issue that had to be overcome in order to extract at least a few Watts out of a fiber laser or amplifier, was the limited output power of fiber-coupled high-brightness pump diodes. The invention of the double-clad fiber structure allowed for the utilization of multi-mode pump sources that deliver nowadays several kW of pump power at 976 nm [88]. Double-clad fibers guide high-brightness light in the core, while the multi-mode pump light is guided in the first cladding, consisting of silica [89]. Thus guiding is achieved by coating the fiber with a proper polymer. Its refractive index determines the index difference to the silica-cladding, i.e. the NA of the pump core. Typically, the polymer's refractive index is ≤ 1.38 , providing a cladding NA value of ≥ 0.46 [90]. The pump cladding diameter is

usually between $125\ \mu\text{m}$ and $400\ \mu\text{m}$ [40]. It is important to implement symmetry-breaking features into the cladding, because otherwise the pump light could propagate on a helical path around the core and get consequently not absorbed [45]. Two common geometries to break this symmetry are D-shaped [91] or hexagonal claddings [92], depicted in Fig. 2.9 (a) and Fig. 2.9 (b), respectively. In PM-fibers, the implementation of stress rods is usually sufficient to prevent the formation of helical pump rays.

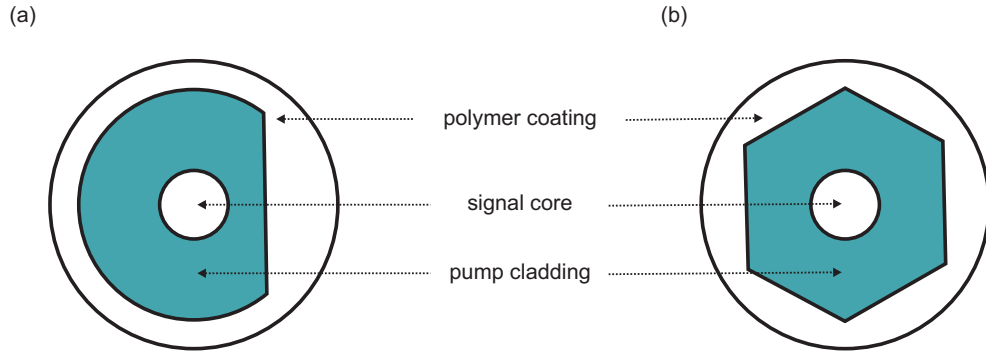


Figure 2.9: (a): D-shaped [91] and (b): hexagonal-shaped [92] pump claddings are commonly incorporated into a double-clad fiber in order to avoid the prevailed formation of helical pump rays that do not get absorbed as they never cross the signal core [45].

The guidance of the pump light in the silica-cladding sets another requirement upon the polymer coating. As it is in direct contact with the evanescent field of the pump light, it can partially absorb it, yielding the deposition of a significant amount of heat. Even advanced polymer compositions, with refractive index values around 1.37, are restricted to long-term operation at temperatures below 90°C [90, 93–95]. This issue was solved by the invention of the so-called air-clad structure. The pump-core in a fiber deploying an air-clad is surrounded by a ring of air, which contains only very thin bridges of silica glass [96]. Bridge thickness and number determine the effective refractive index of the air-clad structure, enabling pump core NAs of up to 0.88 [97]. In order to achieve this, the silica bridges must be essentially narrower than the wavelength of light [98]. Otherwise, the modes with the largest NAs could leak along the silica bridges into the jacket [97]. For mechanical stability, the air-cladding is surrounded by another silica-cladding, even further increasing the distance of the pump core to the polymer coating [50, 96, 97]. As there are no further requirements on the optical properties of the coating anymore, materials that are resistant beyond 90°C can now be applied. Thermo-cured polyimides or silicones work well at temperatures above 200°C , but their manufacturing is complicated and costly [93]. Therefore, a lot of research has been put into the development of UV-cured acrylate-based mid-temperature coating materials [99]. Commercially available mid-temperature coatings are fully qualified for operation up to 165°C and rated even up to 180°C [100]. Polymer coating operating temperatures of 200°C to 300°C are reported in the literature, but even these temperatures can be easily reached by extracting a few 100 W out of an Yb-doped fiber amplifier or oscillator [76, 101].

The second feature of the large mode area (LMA) double-clad fiber is the increased mode field diameter of the fundamental mode, compared to conventional single-mode step-index fibers. It reduces the intensity across the fiber core, leading to higher power thresholds for the onset of nonlinear effects [102]. For conventional step-index fibers this is however accompanied by an increase in the V -parameter and the guidance of higher order modes. The HOMs can be suppressed to a certain degree by e.g. optimized fundamental mode excitation [103] or by coiling of the fiber [16]. The latter is enabled by the mode specific bend losses [104, 105]. As the mode field diameter (MFD) of the HOMs is typically larger than for the fundamental mode, they are less confined and “pushed out” of the core at smaller bending diameters and to a higher extent than the fundamental mode. However, for core diameters of about $30\ \mu\text{m}$, the fiber must be coiled very tightly to obtain reasonable beam quality [17, 106], which in turn reduces the effective MFD of the LP_{01} [102]. Furthermore, for active LMAs the HOM content typically increases with the amplified power level, manifested in a lower beam quality [102, 107]. A more detailed description on this issue will be given in Chapter 4. Besides developing techniques to suppress the HOMs in few-mode fibers for high-power operation, several attempts have been undertaken to develop truly single-mode LMA fibers. The most promising fiber design concepts are photonic crystal fibers (PCF) and chirally coupled core (CCC) fibers. Their working principles are presented in the following two Subsections.

2.3.1 Photonic crystal fibers

Photonic crystal fibers are micro-structured fibers with a periodic capillary lattice in the fused silica of the cladding [34]. Most commonly, a silica-air lattice is used, but the capillaries may contain in general any gas, liquid or glass composition, as long as their refractive index differs from the one of the background material. The resulting periodic index variation forms a two-dimensional photonic crystal in the cross-sectional plane of the fiber, as illustrated in Fig. 2.10. Removing the central capillary yields a “defect” that can act as fiber core [34]. Such a structure enables interesting guiding effects for waves with a nonzero wave-vector component k_z along the fiber’s principal axis, i.e. perpendicular to the periodic plane [108]. Depending on the geometric design of the air-hole lattice, light-wave guiding can be an implication of the photonic bandgap (PBG) [109] effect or TIR [110]. The key parameters determining the waveguide properties are the hole diameter d , the hole spacing (“pitch”) Λ and most significantly, their ratio $\frac{d}{\Lambda}$ [111–113].

PBG guiding can be viewed in a classical physical picture as Bragg-scattering, which occurs if the wavelength of the incident light is smaller or comparable to the lattice constant of a periodic refractive index variation [109]. Depending on their relative phases, the scattered waves experience either constructive or destructive interference. As a consequence, certain combinations of wavelength and wave-vector directions vanish in the structure due to destructive interference, i.e. they cannot propagate [34]. For a fiber containing such a lattice in the cladding, there are two consequences. First of all, light-waves trying to enter from the cladding area outside of the structure are reflected from its surface. Moreover, if

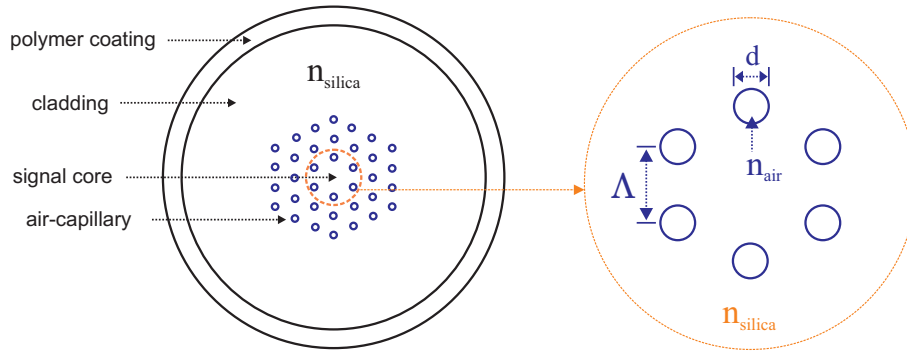


Figure 2.10: Schematic cross-section of a photonic crystal fiber with a hexagonal arrangement of air-capillaries in the silica cladding. The missing air-hole at the fiber center can act as signal core (for proper β and \vec{k} values). To chart the capillary diameter d and the hole-to-hole offset (center-to-center) Λ , the inner air-hole ring (orange circle) is enlarged. Relative sizes and dimensions do not resemble a real fiber, but are for illustration purposes only. While the capillaries contain a material of different refractive index, e.g. air (n_{air}), signal core and cladding have the same refractive index, given by the utilized glass material, most often silica (n_{silica}).

light with proper β and \vec{k} values is launched perpendicular to the periodic plane, it will remain confined within the defect and propagate along the fiber's principal axis. As β and thus k are mode-specific (Section 2.1.3), single-mode (SM) fibers with larger MFDs than achievable with the standard step-index concept can be potentially designed. However, the guiding properties of such a micro-structured fiber are very sensitive to the geometric fiber parameters. Even though PBG guiding can be realized in hollow-core PCFs [109], this approach is useless for the realization of actively doped LMA fibers. Hence, solid-core structures that exhibit bandgaps need to be designed. Theoretically, PBG guiding can occur if the core's refractive index is higher than the average index of the silica-air lattice, for a properly chosen geometry, but in praxis TIR guiding effects dominate in this case [34]. Thus, solid-core PBG fibers are usually made from a low-index glass, surrounded either by consecutive high- and low-index ring layers or by an arrangement of high-index rods. PBG fibers consisting of the ring layer structure are usually referred to as 1D-PBG- or Bragg-fibers [114, 115]. HOM suppression in such a fiber is based on different attenuation coefficients for the different transverse modes [113]. The manufacturing process of such a fiber is however very challenging due to the small index differences of the cladding layers and slight inaccuracies can lead to high propagation loss of the fundamental mode [116]. Moreover, for MFDs as large as $26\ \mu\text{m}$, single-mode operation relies strongly on additional HOM management, such as fiber coiling and tailoring of the doped area [117].

The PBG fibers, containing a high-index rod arrangement, are also referred to as two-dimensional PBG fibers and they seem to be a promising alternative. Their HOM suppression is primarily based on different bending losses for the transverse modes [118]. However, they are still subject to current research and not yet an established techno-

logy [113, 119–121].

LMA PCFs based on TIR, on the other hand, have enabled enhanced single-mode amplifier and oscillator performances within the last few years [50, 122]. In the resonance picture, TIR in a PCF is difficult to distinguish from PBG guiding. There exist, of course, combinations of β and \vec{k} in the cladding lattice that interfere either constructively or destructively when scattered at a silica-air boundary. Viewing the guiding mechanism to be somewhat similar to TIR in step-index fibers helps to distinguish it from PBG guiding and covers most of the observed effects. First of all, TIR occurs only, if the core index is slightly higher than the average index of silica-air lattice [34]. Furthermore, the hole diameters are typically much smaller than for PBG guiding, yielding values of the relative hole size of $\frac{d}{\lambda} \leq 0.424$. This is in fact the single-mode condition for PCFs with a core formed by one missing air-capillary and containing 10 or less air-hole rings [123]. For larger hole sizes, the gaps between the holes become narrower and the core more isolated from the cladding [110]. Accordingly, the effective refractive index as experienced by the core modes decreases, yielding a higher NA and making the fiber more likely to be multi-mode. Increasing the number of air-hole rings has a similar effect.

If $\lambda \geq \Lambda$ and d , the light field gets only slightly affected by the air-holes. Hence, the effective cladding index experienced by the field can be approximated by the average index of the silica-air lattice n_{avg} [124]. When λ approaches the hole diameter d , the guided mode is only evanescent in the air-holes. This is manifested in sharp minima in the far-field pattern of a light-wave transmitted through the PCF [124]. Consequently, the effective index experienced by the light field is larger than n_{avg} .

In order to properly design single-mode PCFs with large mode areas, it is essential to calculate the guided mode set. Like in any other waveguide, the latter can be obtained by solving Maxwells equations under appropriate boundary conditions. Due to the complex structure in the transverse fiber plane, it is however much more complex and thus time-consuming as e.g. in a step-index fiber. Hence, a lot of effort has been put into reducing the calculation time by utilizing appropriate simplifications. Nevertheless, accurate modeling of a PCF with a full-vector analysis is at least necessary to check the validity of the proposed approximations [125, 126]. An overview about some proposed models and numerical techniques is given in Ref. [34].

Still, to get a rough idea about the number of guided modes in a PCF, a normalized frequency similar to Eq. 2.12 for a step-index fiber is useful. Saitoh et al. applied an equivalent step-index index model to the PCF structure, and derived empirical relations to calculate the normalized frequency. The denotation equivalent step-index model refers to the fact that the modal properties, resulting from a complex, varying refractive index structure can be represented by some other fiber with a step-index profile [33]. The empirical relations were found by trial and error fitting of functions $V(\frac{\lambda}{\Lambda}, \frac{d}{\Lambda})$, to values of V , numerically calculated from [127]

$$V = \frac{2\pi}{\lambda} a_{\text{eff}} \sqrt{n_{\text{co}}^2 - n_{\text{FSM}}^2} = \sqrt{U^2 + W^2}. \quad (2.33)$$

In Eq. 2.33, a_{eff} denotes the effective core radius and n_{FSM} the refractive index of the fundamental space filling mode (FSM). The FSM is defined as the lowest order mode that could be guided in the cladding lattice, if the central defect was absent [110]. Accordingly, n_{FSM} represents the refractive index of the cladding and Eq. 2.33 is analogous to the definition of the V -number for step-index fibers. The cut-off condition for single-mode performance of a PCF in this case is also analogous to the step-index fiber, i.e. $V \leq 2.405$ [112]. As the empirical relations derived in Ref. [127] to calculate n_{FSM} depend on $\frac{\lambda}{\Lambda}$ and $\frac{d}{\Lambda}$, this model reflects that the latter parameter is the crucial design criterion for the single-modeness of a PCF for a fixed wavelength. Moreover, it can explain the observed broad single-mode bandwidth of the first drawn PCF, ranging from about 460 nm to 1550 nm [108]. The cladding index defined as n_{FSM} increases towards shorter wavelengths [127], thus balancing for the increasing factor $\frac{1}{\lambda}$, and the value of V remains almost constant over a wide wavelength range. This justifies the definition of the effective cladding index and the V -parameter. Standard step-index fibers designed for single-mode guidance from 1 μm to 1.5 μm on the other hand have typically a cut-off wavelength λ_c (Section 2.1.3) of about 980 nm [40, 128]. From Eq. 2.12 it can be anticipated that the V -parameter increases with decreasing wavelength, as the cladding index remains constant.

The definition of the FSM also alleviates to identify the range of propagation constants that can be guided in the core of a TIR PCF. Being the largest value of β that can exist in the cladding, the propagation constant of the FSM, $\beta_{\text{FSM}} = kn_{\text{FSM}}$ (k is the free-space wavenumber) sets the lower limit for the guided modes set values of β . Analogous to step-index fibers, the upper limit is given by the refractive index of the core material [110], yielding

$$kn_{\text{co}} \geq \beta \geq \beta_{\text{FSM}}. \quad (2.34)$$

Cores formed by more than one missing air-hole enable larger doping areas and thus larger fundamental mode MFDs [129]. Three missing air-holes enable already 30% larger MFDs compared to the one-hole-case, with unchanged propagation losses, while exhibiting no additional losses [111]. The empirical relations from Ref. [127] however, can no longer be applied and n_{FSM} must be evaluated numerically in order to calculate the V -number [130]. Analogous to step-index fibers, the NA must be decreased to keep the V -number below 2.405, the single-mode regime. Hence, n_{FSM} has to approach n_{co} , i.e. the refractive index of silica, and consequently smaller values of d and $\frac{d}{\Lambda}$ are necessary [123]. By removing 7 air-holes, MFDs $\geq 35 \mu\text{m}$ and NAs of 0.03 have been demonstrated [131], but in order to achieve this, $\frac{d}{\Lambda}$ must be kept below 0.046 [123].

An explanation why increasing the number of air-hole rings requires even lower values of $\frac{d}{\Lambda}$ for a PCF to be strictly single-mode can be anticipated from the following considerations. While the propagation constant of the fundamental core mode must fulfill Eq. 2.34,

$$\beta_{\text{HOM}} \leq \beta_{\text{FSM}} \quad \equiv \quad n_{\text{HOM}} \leq n_{\text{FSM}} \leq n_{\text{FM}} \leq n_{\text{co}} \quad (2.35)$$

would be the ideal case for a truly single-mode fiber [132]. Nevertheless, Saitoh et al. calculated that for a fixed value of $\frac{d}{\lambda}$, the effective refractive index of the HOMs approaches the value of n_{FSM} with increasing number of air-hole rings [123]. Guidance of the particular HOM is eventually enabled, which must be counter-acted by lowering $\frac{d}{\lambda}$.

Eq. 2.35 also indicates the difficulty in fabricating single-mode, very large MFD PCFs. The refractive indexes are not independent of each other, as there exists no “real” index-step due to different materials. To meet the condition in Eq. 2.35, the index of the core material must be controlled by an order of magnitude of at least 10^{-4} , but this is very difficult in practice [129].

The manufacturing process of a PCF is similar to a step-index fiber, but again the difficulty arises from the complex cladding structure. As the preform must already contain all of the relative dimensions [33], it is this fabrication stage that is the most challenging. Several techniques have been tried out, including extrusion, sol-gel casting, injection molding and drilling of the capillaries [34]. Most commonly, silica PCFs are obtained by repeated stacking and drawing of circular capillaries and rods [98, 131, 133, 134]. In the first step, capillaries of about 1 m length are drawn from pure-silica starting tubes with an outer diameter of about 20 mm. The capillary diameter after this stage is about 1 mm and should not vary by more than 1% over the entire length [34]. Another critical parameter is the ratio of the inner and outer diameter of the starting tubes, which is typically between 0.3 and 0.9, and largely determines the key parameter $\frac{d}{\lambda}$ [34]. Next, the capillaries are stacked together and the hole assembly is placed into a jacketing tube, later forming the outer, pure silica part of the cladding. For small core diameters, one capillary is replaced by a rod [108]. Depending on whether a passive or active fiber is supposed to be manufactured, the central rod consists either of pure silica or is doped with rare-earth ions. For LMA PCFs, several capillary rings are removed, typically yielding a hexagonal core shape [131, 135]. Even though the emitted beams have noncircular shapes, most of the power is usually contained in a round central part, resembling almost a Gaussian intensity distribution [133].

During the final drawing process, only limited adjustment of the fiber parameters can be achieved by controlling the pressure and furnace temperature [34]. The overall fiber performance on the other hand depends strongly on effects during the drawing process, such as viscous flow, surface tension and pressure. Hence, several fabrication iterations are necessary, if a new fiber design is to be drawn. Moreover, for active fibers it is very important to keep the index increase of the core caused by the active ion doping as low as possible in order to preclude step-index guiding [136]. To compensate for this index increase, additional dopants such as e.g. fluorine can be used [131, 133].

One disadvantage of a low NA value that is required for LMA single-mode operation is the high sensitivity towards bending effects [122, 137]. For long wavelengths, a PCF behaves like a standard step-index fiber. There exists a long wavelength edge beyond which the light field experiences massive bending loss, which depends on the core index and radius, as well as on the V -parameter. Contrary to step-index fibers, PCFs inhibit also a short wavelength bend loss edge [110]. Other, less critical attenuation mechanisms

in a PCF include absorption and scattering just as in a step-index fiber (Section 2.1.2). PCF specific propagation attenuation is due to the glass-air interfaces in the cladding. The two main parameters that influence this loss source are the fraction of light in the glass and the roughness of the interface [34].

The high bending losses are the reason why PCFs with MFDs larger than $35\ \mu\text{m}$ and NAs below 0.03 are produced as rods, with outer cladding diameters of about 1 mm to preclude any bending [135]. Consequently, current research still targets to develop a technology that enables to maintain the coiling benefit of fibers compared to bulk materials. A promising approach are chirally coupled core fibers, as will be described in the next Subsection.

2.3.2 Chirally coupled core fibers

Another fiber design concept, proposed to enable single-modeness of large mode area fibers is the chirally coupled core (CCC) design. CCC fibers are a weakly-coupled waveguide system, consisting of a step-index fiber structure, whose signal core is additionally chirally surrounded by one or more satellite cores. A schematic of this geometry is depicted in Fig. 2.11. It is manufactured by the so-called stack-and-draw technique, where the core preforms are stacked straight and parallel into the cladding preform [138]. These preforms are typically produced just as step-index fibers (Section 2.1.1) and already resemble the correct relative diameters. To obtain the helical path of the side core(s), the preform assembly is spun during the drawing process. Thereby, the helix offset R_{helix} (Fig. 2.11 (a)) and the helix pitch Λ_{helix} (Fig. 2.11 (b)) are permanently controlled to achieve ideal performance throughout the entire fiber length. Real-time monitoring of these parameters and immediate adjustment of the furnace temperature, the drawing speed as well as the spinning rate is necessary. Thus, the drawing process is much more challenging than for a pure step-index fiber, where only the fiber diameter needs to be controlled.

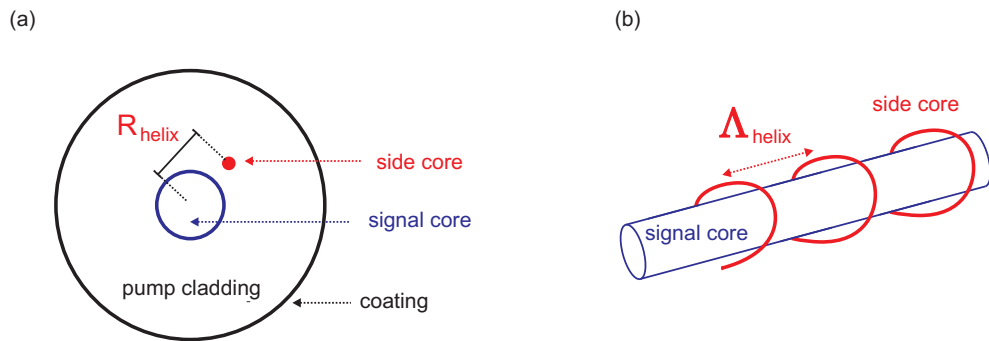


Figure 2.11: Sketch of (a): cross-section and (b): spatial view of a chirally coupled core fiber with one helical satellite core [139]. R_{helix} denotes the signal-core to side-core offset, and Λ_{helix} the helix pitch.

To understand the working principle of CCC fibers it is necessary to consider some features of conventionally coupled waveguides, such as e.g. a step-index fiber with two

straight and parallel cores. Eigenmodes of these two cores can only interact with each other, if their phase velocities i.e. their propagation constants are the same [64]. As soon as the two waveguides differ in core size or refractive index, phase matching of one modal pair can only be achieved at one wavelength. This resonance occurs, where the dispersion curves of the two waveguides cross [140]. The idea of CCC fibers is that the phase difference of one modal pair at one particular wavelength can be compensated by an additional relative phase shift, if one of the waveguides is not straight but rotating around the other waveguide. The relative rotation leads to the accumulation of different amounts of angular momentum [141, 142] of the modes in the two waveguides that can balance the difference in β due to the linear momentum [143]. As a consequence, such a waveguide structure has several resonance wavelengths for each modal pair, which are referred to as quasi phase matched (QPM), to account for the balancing of the linear momentum difference by the angular momentum [138]. By properly choosing the right helix parameters, phase-matching of the HOMs from the signal core to the modes of the side core is obtained and additionally, high loss for the selected side core modes can be achieved [139]. That way, the HOMs are “pulled” out of the signal core, which then only guides the fundamental mode, i.e. is effectively single-mode.

As the CCC structure has a helical-translation symmetry, only modes of the individual waveguides that are simultaneously invariant to translation along and rotation around the z-axis can interact with each other [138]. As a consequence, their modal field-vector distributions and vector-amplitude distributions have to make a full rotation within each optical cycle. Fig. 2.12 (a) shows such a modal field-vector distribution along the fiber axis z, i.e. the evolution of a circular polarized electric-field. It makes one full rotation around the fiber axis, while propagating a distance along the fiber axis that is equal to the modes wavelength. The angular momentum associated with the circular polarization of the light is commonly referred to as optical-spin [141].

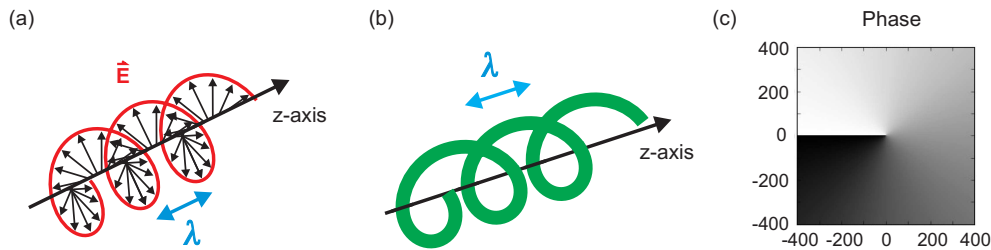


Figure 2.12: (a): In a Cartesian coordinate system, with the fiber’s propagation axis as z-axis, the electric field-vector \vec{E} of the side core mode corresponds to a circular polarized field that carries spin-momentum [138]. (b): Example of a helical wave, propagating along the z-axis, where it has a phase singularity (optical vortex) [144]. (c): Its associated azimuthal phase performs one full 2π rotation in the transverse plane around the z-axis, yielding a topological charge of $|m|=1$ of the beam, corresponding to an intrinsic orbital-angular momentum given by $m\hbar$ [145].

Since the side-core in a CCC-fiber is helically twined around the signal-core and thus

the fiber's principal axis, the side-core's eigenmodes propagate on a helical path around the z-axis. In the laboratory reference frame, these modes can be described as helical modes. Their electric field amplitude is zero at the z-axis, ensuing an "optical vortex" (Fig. 2.12 (b)) [144, 146]. In the x-y-plane, the helical modes' wavefront consists of $|m|$ interwoven surfaces, yielding an azimuthal phase that rotates $|m|$ times 2π around the optical vortex [145, 147]. Consequently, these modes do not possess well defined phase- or wavefronts. The integer m is called orbital helicity of the beam or topological charge of the vortex [145]. Its sign gives the handedness of the surface-twist [148]. Thus, the topological charge of the example illustrated in Fig. 2.12 (b) and (c) is 1. Each photon associated with a helical mode carries a quantized z-component of angular momentum, given by $m\hbar$ and called orbital angular momentum [142].

The challenge of describing modes in a CCC structure arises from the z-dependence of the position and orientation of the side core in a Cartesian reference frame. Therefore, Ma et al. used a curvilinear helical reference frame with x- and y-axes rotating around the principal fiber axis (z-direction) with the side-core helix-pitch Λ_{helix} to calculate the modes and resonances [138]. In this reference frame, the fiber has a longitudinally invariant refractive index profile and two parallel and straight cores. Hence, the transverse permittivity tensor distribution is z-invariant and a standard finite-element-method based modal solver for anisotropic waveguides can be applied to solve Maxwell's equations to obtain the propagation constants and the transverse electric-field distributions [138].

This calculation reveals a feature of modes in CCC fibers that alleviates the understanding of the CCC working mechanism. The modes within one LP_{lm} group that are degenerate in a conventional step-index fiber carry different spin- and orbital-angular momentum, in terms of magnitudes and polarities, if interaction between the two cores is considered [138]. Thus they are not degenerate anymore and can interact with each other. Degeneracy in one individual core, on the other hand, still holds. By controlling the spin- and orbital-angular momentum of the HOMs from the signal core through adjustment of the helix parameters, in a way that the QPM condition

$$\beta_{l_1 m_1} - \beta_{l_2 m_2} \cdot \sqrt{1 + K^2 R_{\text{helix}}^2} - \Delta m \cdot K = 0, \quad (2.36)$$

with $K = 2\pi/\Lambda_{\text{helix}}$, the helix offset R_{helix} and the propagation constants of the modes from the central core $\beta_{l_1 m_1}$ and the side core $\beta_{l_2 m_2}$, is fulfilled [138], an effectively single-mode core can be achieved. The integer Δm depends on the mode numbers l_1 and l_2 as well as an integer, Δs . Physically, $\Delta s = 0$ corresponds to coupling between modes of the same polarization, caused by the perturbation of the central core simply through the presence of the side core. The difference in thermal expansion between the two cores and the cladding during the drawing process causes local linear birefringence, which in turn yields coupling between orthogonally polarized modes. This is covered by $\Delta s = -2$ and $+2$. The values $+1$ and -1 of Δs represent the mixing of the longitudinal and transverse modal field components, which is caused by local "shear" birefringence due to the viscosity of the glass flow during the spinning of the heat-softened fiber preform [138]. Conventional

fibers on the other hand have independent rotational and linear-translation invariance. Their modes are not invariant to helical-translation, thus possessing either optical spin- or orbital-angular momentum.

2.4 Conclusion

This Chapter has given an overview about the physical fundamentals related to design fiber amplifier systems for the 3rd generation of GWDs. Basic properties of optical fibers were presented and it was explained how the nonlinear effect of SBS limits the power scaling of single-frequency lasers in strictly single-mode step-index fibers. Moreover, the advanced design concepts of photonic crystal fibers and chirally coupled core fibers were introduced. These fiber concepts are very promising candidates to enable single-mode single-frequency signal amplification to power levels beyond the limits of conventional step-index fibers.

In the following Chapters of this thesis, the carried out experiments will be presented and discussed. The next Chapter starts with the analyses of a general physical aspect of single-frequency signal amplification in fiber amplifiers. This is the impact of ASE on the Brillouin scattering process.

3 The impact of ASE on Brillouin scattering of a single-frequency signal

Single-frequency (SF) laser oscillators that have suitable properties for application in GW detectors are limited to only a few watts of output power. Amplification of such a signal to a few hundred watts corresponds to gain factors around 20 dB. In fiber amplifiers, this can lead to a high sensitivity towards parasitic lasing processes and a significant amount of output power in amplified spontaneous emission (ASE). ASE photons within the Brillouin gain bandwidth (BGBW) and co-propagating to the Stokes signal could potentially seed the Brillouin scattering process and lower the SBS threshold power. In case of SF amplifiers, an effect of ASE on the Brillouin scattering process is at least expected by Pannell et al. [149] and Hildebrandt et al. [78], as they included a term accounting for ASE in their calculations of Brillouin scattering in optical fiber amplifiers. Thus, it was interesting for the work of this thesis to investigate the impact of ASE on the Brillouin scattering of a SF signal. This analysis is presented in this Chapter, starting with a numerical calculation of the SBS threshold of a SF fiber amplifier (Section 3.1). The case, when a term accounting for backward ASE was included in the differential equation for the Brillouin power, was compared to the case, when no such term was implemented. Using a passive fiber and artificially added ASE, co-propagating to the Stokes signal, the impact of ASE in the BGBW on the Brillouin scattering process of a SF signal is demonstrated in general (Section 3.2).

To decrease the gain factor in high power fiber amplifiers, it is common to use intermediate amplifier stages with output powers of several 10 watts. Unfortunately, besides preamplifying the SF signal, these amplifier stages also generate ASE photons, even if the overall ASE power can be kept comparably low. In particular, also ASE photons within the BGBW will be injected into the high power amplification stage, unless a very narrow bandpass filter is used in front of it. Rayleigh-backscattered ASE within the BGBW could then potentially seed the SBS process in the main amplifier.

Cooperative stimulated Brillouin and Rayleigh backscattering has at least been observed in long single-mode fibers with high Rayleigh losses [150]. Dynamic distributed feedback due to double Rayleigh scattering of the Stokes field led to SBS lasing, yielding a very narrow spectrum of the Stokes field. The possibility that Rayleigh-backscattered ASE from a fiber preamplification stage might be sufficient to seed the SBS process in an optical amplifier is experimentally tested in Section 3.3.

3.1 Numerical SBS-threshold calculations of a single-frequency amplifier

To investigate the significance of a term accounting for ASE in the calculation of the SBS threshold of SF fiber amplifiers, calculations using the numerical model presented in Ref. [78] were carried out. There, the evolution of the signal power (P_s), the pump power (P_p), the forward and backward ASE power ($P_{\text{ASE}}^{\text{f,b}}$), and the Brillouin scattered signal power (P_{BS}) were calculated along an amplifier fiber. The corresponding set of differential equations was solved by applying a Runge-Kutta algorithm and a shooting method. A discrete number of spectral lines within the Brillouin gain frequency range ($\Delta\nu_{\text{B}}$) described the Brillouin scattered radiation. Two consecutive spectral lines were separated by the bandwidth $\Delta\nu_{\text{SBS}}$. A distributed, nonfluctuating source model with spontaneously generated Brillouin noise power at different positions along the amplifier fiber provided the noise initiation of the SBS-process. The noise photon power at the frequency ν_i of the i -th Brillouin line was given by

$$P_{n_i} = \frac{4h\nu_i\Delta\nu_{\text{SBS}}}{(1 + (2(\nu_{\text{B}} - \nu_i)/\Delta\nu_{\text{B}})^2)(\exp(h\nu_{\text{B}}/kT) - 1)}. \quad (3.1)$$

Here, h is Planck's constant, ν_{B} the Brillouin shift frequency, k Boltzmann's constant, and T is the temperature in the fiber. In the differential equation for the power in the i -th SBS line,

$$\frac{dP_{\text{BS}_i}}{dz} = -\Gamma_{\text{s}}P_{\text{BS}_i}(N_2\sigma_{\text{BS}_i}^{\text{e}} - N_1\sigma_{\text{BS}_i}^{\text{a}}) + \alpha P_{\text{BS}_i} - P_{\text{s}}g_{\text{B}_i} \left(P_{\text{BS}_i} + P_{n_i} + P_{\text{ASE,BS}}^{\text{b}} \frac{\Delta\nu_{\text{SBS}}}{\Delta\nu_{\text{ASE}}} \right) / A_{\text{eff}}, \quad (3.2)$$

Γ_{s} accounts for the overlap of the guided LP₀₁ mode and the doped step-index core region, N_2 and N_1 are the ion densities in the upper and lower energy levels, respectively, $\sigma_{\text{BS}_i}^{\text{e}}$ and $\sigma_{\text{BS}_i}^{\text{a}}$ are the emission and absorption cross-sections of the ytterbium doped fiber. Furthermore, α is introduced to account for background losses through fiber imperfections and Rayleigh scattering, and A_{eff} is the effective modefield area of the fiber. The last term in Eq. 3.2 accounts for the backward propagating ASE power at the Brillouin wavelength ($P_{\text{ASE,BS}}^{\text{b}}$), seeding the SBS process. Similarly to the Brillouin scattered radiation, the broadband ASE was described. A discrete number of spectral lines at wavelength λ_{ASE_j} , separated by a bandwidth $\Delta\nu_{\text{ASE}}$ was initiated by a noise photon power $P_0 = \frac{2hc}{\lambda_{\text{ASE}_j}\Delta\nu_{\text{ASE}}}$, with Planck's constant h and c being the speed of light in vacuum. To account for the two possible polarization states, the factor of 2 was introduced.

In Ref. [78] it had already been shown that this numerical model is suitable to adequately simulate a SF fiber amplifier, once the right fiber and amplifier parameters are implemented. The calculations presented here do not resemble a particular fiber amplifier system, but they demonstrate the effect that there is a significant difference in the SBS power evolution

Table 3.1: Simulation parameters for the numerical model. g_B is the Brillouin gain peak value and c_f the coefficient for the temperature induced Brillouin frequency shift [78].

parameter	value	parameter	value
Γ_s	0.85	r_{core}	9.9 μm
α_s	0.001 m^{-1}	$r_{cladding}$	200 μm
$\Delta\nu_B$	58 MHz	core NA	0.055
g_B	$2.4 \cdot 10^{-11}$ m/W	SBS lines	50
c_f	2.25 MHz/K	$\Delta\nu_{SBS}$	6 MHz
doping concentration	$7 \cdot 10^{25}$ ions/ m^3	ASE lines	25
fiber length	8 m	ASE start/stop λ	1030 nm/1100 nm

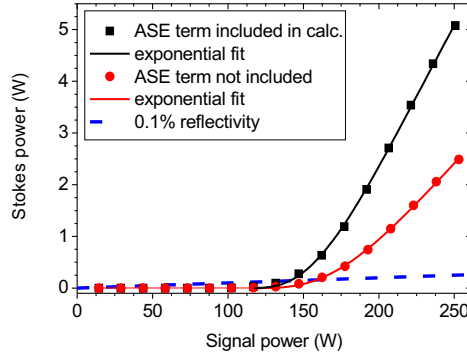


Figure 3.1: Calculated Stokes power with respect to the amplified signal power when the term accounting for backward ASE was included in the numerical simulation (black squares) and excluded (red circles). The dashed blue line corresponds to a reflectivity of 0.1 %.

whether a term accounting for backward ASE at the Brillouin wavelength is included in the calculation or not, in general. The used parameters are mostly taken from Ref. [78] and can be found in Table 3.1. Representative results are shown in Fig. 3.1, in which the backscattered Stokes power is plotted with respect to the launched signal power. The seed power in this case was 1 W and the pump light was counter-propagating to the signal. Common definitions of the SBS threshold are the amount of signal power where the backscattered power departs from linear behavior or reaches a certain reflectivity, but this is quite ambiguous in the literature. In order to compare the SBS thresholds in these calculations and the following experiments, the SBS threshold was chosen to be the amount of signal power corresponding to a reflectivity, i.e. an amount of backscattered power of 0.1 %. For the simulated fiber amplifier, this threshold was about 140 W when the Stokes power calculation accounted for ASE. The threshold power increased by 13 % to 158 W, when the last term in Eq. 3.2 was not included in the calculation. It can be clearly seen

in Fig. 3.1 that at higher signal power levels, the difference in the backscattered Stokes power at a certain signal power increased even more. Due to the neglect of the ASE term, the power of the Brillouin scattered light decreased from 5.1 W to 2.4 W at a signal power of 250 W. This corresponds to a decrease by 47 %.

The calculated decrease in the threshold power in case of accounting for ASE in the SBS calculation can be explained by seeding the SBS process by ASE within the BGBW and co-propagating to the Stokes signal. These ASE photons are, in this case, generated in the active fiber, as no additional ASE was injected into the modeled amplifier.

3.2 ASE counter-propagating to a SF signal in a passive fiber

As numerically calculated in Section 3.1, ASE within the BGBW and co-propagating to the Stokes signal apparently has an influence on the SBS threshold power level of a fiber amplifier. To gain an insight into the proposed effect, the SBS process of a SF signal in a passive fiber was investigated. To account for the ASE generated in the amplifier fiber, ASE was artificially added counter-propagating to the SF signal, and hence co-propagating to the Stokes signal. An analytic evaluation of this process was carried out beforehand.

Considering the signal power to be much larger than the Brillouin scattered power, pump depletion could be neglected. Hence, the Stokes power was calculated according to Eq. 2.31. The potentially injected ASE power within the BGBW was used as the initial power at the Stokes wavelength at the fiber end ($I_s(L)$). To account for the Lorentzian-shaped BGBW, the amount of total injected ASE power ($P_{\text{ASE_total}}$) was equally distributed among 200 discrete frequencies within a rectangular shaped ASE spectrum. Its width corresponded to the FWHM of the Brillouin gain spectrum and the lines were equally spaced. For each of these lines, Eq. 2.31 was evaluated, where g_B was substituted by the frequency dependent Brillouin gain value, calculated from $g(\nu)$ (Eq. 2.24). These calculations were carried out for launched signal powers from 0 mW to 100 mW, in steps of 1 mW, and different values of the peak Brillouin gain g_B . To be able to compare the analytical with the experimental results, the fiber parameters were taken from the fiber used in the experiment (Section 3.2). All parameters used in this analytical evaluation are listed in Table 3.2.

Table 3.2: Parameters applied in the analytical calculation.

parameter	value	parameter	value
MFD	4 μm [128]	A_{eff}	12.6 μm^2 (Eq. 2.16)
α_{dB}	2.5 dB/km [128]	L	335 m
λ_p	1064 nm	$\Delta\nu_B$	50 MHz [151]
ν_B	16 GHz (Eq. 2.23)	g_B	1-2 $\cdot 10^{-11}$ m/W+[67]

The calculated total amount of backscattered Stokes power (i.e. the seed power was not subtracted) with respect to the launched signal power for two different values of g_B is

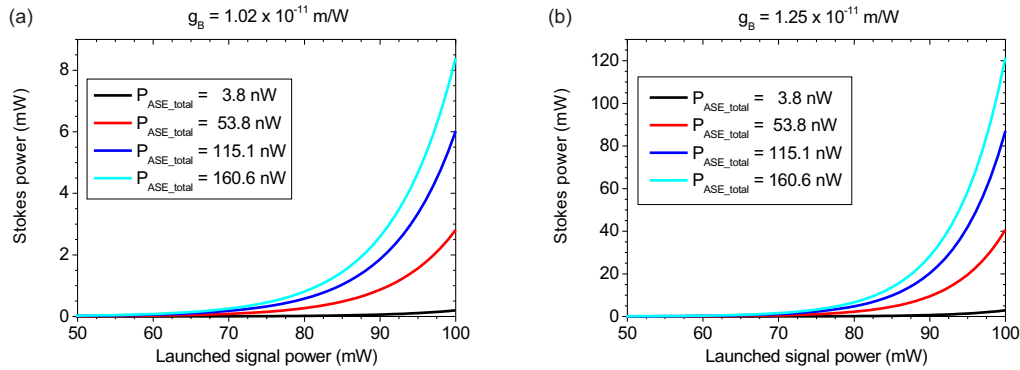


Figure 3.2: Analytically calculated Stokes power with respect to the launched signal power for different amounts of total ASE power within the BGBW ($P_{\text{ASE_total}}$) and different values of the peak Brillouin gain g_B . (a): $g_B=1.02 \cdot 10^{-11} \text{ m/W}$, (b): $g_B=1.25 \cdot 10^{-11} \text{ m/W}$.

shown in Fig. 3.2. With increasing ASE power, the Stokes power at one particular launched signal power level increased, just as expected. Nevertheless, the calculated values for the Stokes power were very sensitive to the choice of the peak Brillouin gain. As will be seen in Section 3.2.2, with g_B set to a small but reasonable value of about $g_B=1.02 \cdot 10^{-11} \text{ m/W}$ (Fig. 3.2 (a)) [74], they resembled the experimental data quite well. For $g_B=1.25 \cdot 10^{-11} \text{ m/W}$ (Fig. 3.2 (a)), the backscattered power was already too large for the undepleted pump limit approximation to be valid, yielding Stokes power values eventually exceeding the launched signal power.

3.2.1 Experimental setup

The setup used for the experiments is depicted in Fig. 3.3. As signal source, a commercial nonplanar ring oscillator (NPRO), delivering up to 400 mW at 1064 nm with a signal linewidth of approximately 1 kHz, was used. The NPRO was protected from backreflections by a Faraday isolator (nominal isolation $\geq 35 \text{ dB}$), which was followed by a variable attenuator, consisting of a half-waveplate and a polarizing beam splitter (PBS). To monitor the signal-to-fiber-coupling and to detect a sample of the backscattered light, a 90/10-tap-coupler (all tap-couplers were built in-house; the typical value for the return loss is $\geq 35 \text{ dB}$) was used. The fiber generating the Brillouin scattered Stokes signal was an approximately 335 m long piece of HI-1060-Flex from Corning, a commercially available passive fiber with a nominal core diameter of $3.4 \mu\text{m}$ [128]. A 70/30-tap-coupler was spliced to the other end of the fiber to couple in and monitor the ASE as well as to extract a sample of the transmitted signal.

The artificially added ASE was supposed to resemble ASE generated in a fiber amplifier. Therefore, the ASE source consisted of components typical for a SF fiber amplifier. As active fiber, 10 m of the PLMA-YDF-10/125 by Nufern were used, which were cladding-pumped through an in-house built pump combiner by a commercial 25 W fiber-coupled

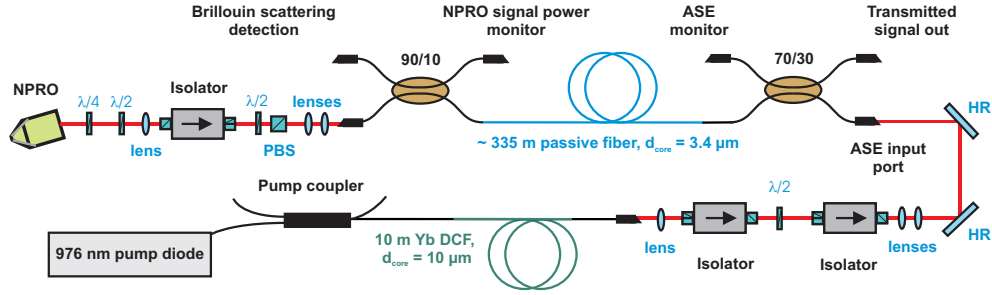


Figure 3.3: The setup used in the experiments with a passive fiber. The ASE was counter-propagating to the SF signal. HR: highly-reflective mirror, $\lambda/2$: half-wave plate, $\lambda/4$: quarter-wave plate.

diode at 976 nm. To protect the ASE source from the NPRO signal transmitted through the HI-1060-Flex, two Faraday isolators with a nominal isolation of ≥ 35 dB each were implemented. Behind the isolators, the maximum ASE power was 139 mW, limited by the onset of parasitic lasing processes. About 60 % of the ASE power could be coupled into the 70/30-tap-coupler, of which the 70 %-output-port was spliced to the HI-1060-Flex. At all fiber ends, angle-polished fiber connectors were used to protect the fibers from backreflections. Furthermore, all lenses used had AR-coatings at the relevant wavelengths.

3.2.2 Measurement method and results

To determine the SBS threshold of the used fiber without additional injected ASE, the signal power was increased via the variable attenuator, while the backscattered power and optical spectra were detected at the backwards directed 10 %-output-port of the first tap-coupler. Additionally, the transmitted power was measured at the 30 %-output-port of the second tap-coupler. This procedure was repeated for four different levels of ASE power in the BGBW.

As only ASE photons within the BGBW can potentially seed the SBS process, the ASE source was set up such that the ASE maximum was roughly at the Brillouin wavelength. Hence, the spectral shape can be considered as flat in the relevant spectral interval. To increase the overall ASE power in the fiber, the pump power was increased. From the measurement of the power and optical spectra at the 30 %-ASE-monitor-port of the tap-coupler, the ASE power in the BGBW was calculated. Assuming a BGBW of 50 MHz [151], the ASE power levels in the BGBW used in the experiments ($P_{\text{ASE,BGBW}}$) were between 3.8 nW and 160.6 nW. The corresponding optical spectra are shown in Fig. 3.4 (a).

In Fig. 3.4 (b), the backscattered power is plotted versus the signal power for different injected ASE power levels. Note that the power offset created by the transmitted ASE was subtracted in the graph for better comparison. Without artificial ASE, the backscattered power started to rise very slowly compared to the cases when additional ASE was injected into the fiber. In fact, only at a signal power of 81 mW, the evolution of the backscattered

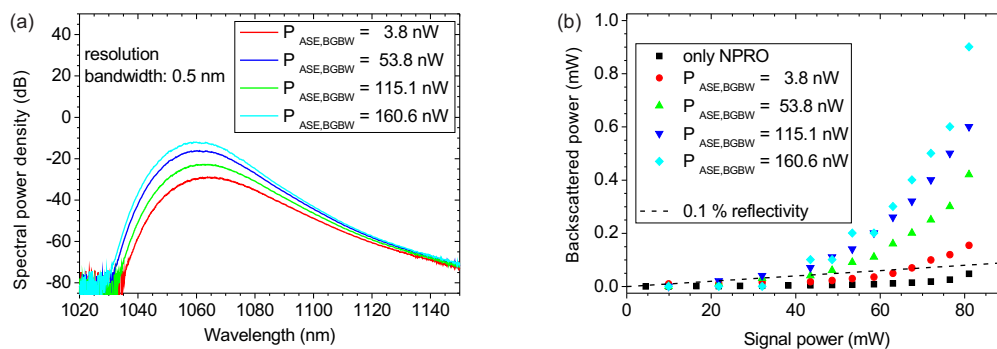


Figure 3.4: (a): The optical spectra of the ASE injected into the fiber, measured at the 30 %-port of the second tap-coupler, for four different power levels used in the experiments. (b): Backscattered power with respect to the signal power for different levels of ASE within the BGBW. ASE counter-propagating to the SF signal. The dashed line indicates where the backscattered power reaches 0.1 % of the signal power.

power departed from linear behavior. A reflectivity of 0.1 %, the SBS-threshold, as defined in Section 3.1, was not reached even at the maximum signal power. It can be clearly seen in Fig. 3.4 (b) that the more ASE was added, the smaller was the signal power when the backscattered power started to rise exponentially. With power values within the BGBW of 3.8 nW and 53.8 nW, the SBS-threshold power values were 67 mW and 44 mW, respectively. With ASE power values within the BGBW of 115.1 nW and 160.6 nW, the SBS-threshold was reached at signal powers smaller than 40 mW. At a signal power of 81 mW, the backscattered power was 19 times as high when 160.6 nW of ASE were added, compared to the case when no additional ASE was used.

To obtain more information about the power evolution of the Brillouin scattered signal, the optical spectra of the backscattered light were measured with an optical spectrum analyzer (OSA) with a resolution bandwidth (RBW) of 0.01 nm. In these spectra, the signal at the seed wavelength generated by Rayleigh scattering and spurious backreflections could clearly be separated from the Brillouin scattered signal. In Fig. 3.5 (a) the optical spectra of the backscattered light for the case of no additional ASE in the backward direction are shown. At low power the Brillouin triplet, consisting of the elastic Rayleigh scattering line, and the two inelastic Stokes and anti-Stokes lines at the shifted wavelength of ~ 60 pm corresponding to a frequency shift of about 15.9 GHz, is evident. With increasing signal power, the Stokes component of the spectrum increases due to the onset of stimulated Brillouin scattering.

Figure 3.5 (b) shows the evolution of the backscattered optical spectra when 3.8 nW of ASE within the BGBW were added counter-propagating to the SF signal. Due to the transmitted ASE, which can be seen as the -47 dB offset in Fig. 3.5 (b), the Stokes and anti-Stokes lines cannot be seen at low signal powers. At higher signal powers, only the Stokes line is evident besides the Rayleigh line, indicating the onset of the stimulated

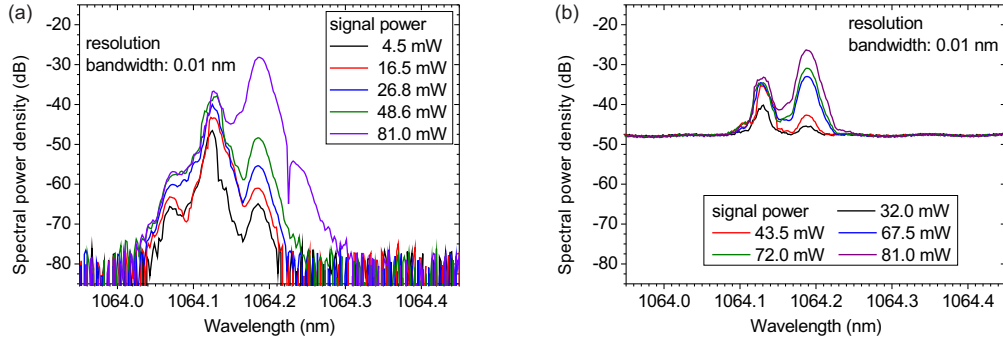


Figure 3.5: (a): Evolution of the backscattered optical spectra for the case of no additional ASE and (b): when 3.8 nW of ASE power within the BGBW were added counter-propagating to the signal with increasing signal power.

Brillouin scattering process. Comparing the power in the Stokes peak line to the ones in Fig. 3.5 (a) indicates that the small amount of added ASE already seeds the stimulated Brillouin scattering process. In the case of no additional ASE, injecting a signal power of about 49 mW resulted in a spectral power density of -48 dB of the Stokes peak line. When only 3.8 nW of ASE power in the BGBW were added counter-propagating to the signal, the Stokes peak line's spectral power density was already about -42.6 dB for only 43.5 mW of signal power. Injecting 81 mW of signal power yielded Stokes peak line spectral power densities of about -28 dB and -26 dB for no ASE and $P_{\text{ASE,BGBW}} = 3.8 \text{ nW}$, respectively. For higher ASE power levels, the backscattered optical spectra looked alike, but the offset due to ASE was even higher.

Figure 3.6 shows the Stokes peak line power with respect to the signal power for the ASE levels corresponding to Fig. 3.4 (a). Again, it can be clearly seen that the more ASE power in the BGBW was injected into the fiber, the stronger was the exponential increase of the Brillouin scattered signal. Accordingly, the power in the Brillouin peak line at a fixed value of signal power increases with increasing ASE power. At a signal power of 81 mW the power in the Brillouin peak line was 19 times as high when 160.6 nW of ASE in the BGBW were injected, compared to the case when no artificial ASE was added.

The exponential rise of the backscattered power is a characteristic typically considered as the threshold of SBS [78]. Therefore, it can be concluded from the data above that with increasing ASE power within the BGBW and co-propagating with the Brillouin scattered signal, the SBS threshold decreases. This effect could contribute to the fact that increasing the seed power for a fiber amplifier increases its SBS threshold [149], as not only the overall amplification gain factor is reduced, but also the amount of generated backwards ASE. In master-oscillator fiber-amplifier systems, gain factors can be as high as several 10 dB, which can yield a significant amount of power in generated ASE in the backward direction. According to the results presented here, this can possibly seed the SBS process.

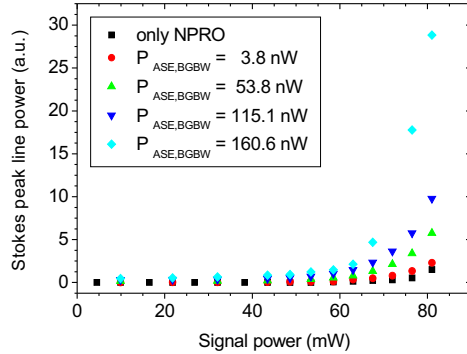


Figure 3.6: Stokes peak line power with respect to the signal power for different powers of ASE in the BGBW. ASE counter-propagating to the signal.

To increase the SBS-threshold by decreasing the gain factors, the utilization of an intermediate amplifier stage to preamplify a low power seed signal is a common approach. However, the ASE generated in the preamplifier is then usually also coupled into the high power main amplifier. The Rayleigh-backscattered part of the ASE within the BGBW could then potentially increase the strength of the Brillouin scattering process. Experimental results investigating this possibility are presented in the following Section (3.3).

3.3 SBS threshold measurements on a fiber amplifier with added ASE

The amount of power in the backward direction of an optical amplifier due to Rayleigh scattering and spurious reflections depends on various fiber parameters such as the used material composition and the homogeneity of the glass matrix, as well as the signal wavelength. A typical value for the Rayleigh scattering damping coefficient of a standard silica fiber for a signal wavelength of $1\ \mu\text{m}$ is $1\ \text{dB/km}$ [36]. This corresponds to a backscattered signal power of $26\ \text{dB}$ below the injected signal power level. However, in an active fiber due to the inhomogeneity of the fiber core induced by the implementation of the active ions, the overall backscattered power can be significantly higher and is difficult to estimate. Furthermore, the effect of optical amplification has to be considered, as the backward propagating light experiences the same gain as the forward propagating signal. For the work of this thesis it was thus interesting to investigate the eventuality that the Rayleigh backscattered ASE within the BGBW from a fiber preamplification stage could decrease the SBS threshold of an optical amplifier. These experiments were carried out with artificially added ASE in forward direction of a low-power Ytterbium-doped fiber amplifier and the results are presented in this Section.

3.3.1 Experimental setup

The setup is depicted in Fig. 3.7. A 90/10-tap-coupler was used to combine the signals from the NPRO and the ASE source, which was the same as described in Section 3.2. Again, the ASE signal-to-fiber coupling was about 60%. The port containing about 10% of the NPRO power and 90% of the ASE power was spliced to a second 90/10-tap-coupler, of which the backwards directed 10%-port was used to monitor the backscattered signal. The seed monitor port contained 10% of the power, while 90% of the combined signal seeded the following fiber amplifier.

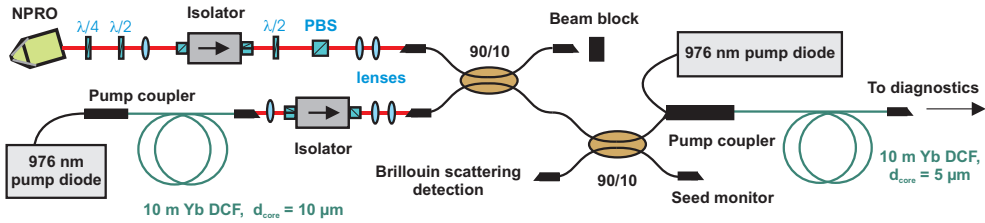


Figure 3.7: Setup of fiber amplifier, seeded with an NPRO and artificially added ASE co-propagating to the SF signal. $\lambda/2$: half-wave plate, $\lambda/4$: quarter-wave plate.

Signal- and pump-beam were coupled into the active double-clad fiber, with nominal signal- and pump-core diameters of $5\ \mu\text{m}$ and $125\ \mu\text{m}$, via a pump combiner. A fiber-coupled multi-mode diode provided a maximum pump power of 9 W at 976 nm.

3.3.2 Measurement method and results

The characterization of the amplifier was performed as follows. While the SF signal from the NPRO remained at the same power level of 50 mW throughout the measurements, different amounts of ASE were artificially added. Therefore, the ratio of the SF signal and the ASE at the signal wavelength was measured with an optical spectrum analyzer (resolution set to 0.5 nm) at the 10%-seed-monitor-port. Fig. 3.8 shows the optical spectra of the amplifier seed for no and three different power levels of ASE. Limited by the onset of parasitic lasing processes in the ASE source, the lowest signal-to-noise ratio (SNR), i.e. the largest amount of added ASE resulted in a spectral power density of 16.6 dB below the NPRO peak line. The corresponding power values of ASE within the BGBW are given in Table 3.3. Again, they were calculated from the optical spectra and the additional measurement of the power at the 10%-seed-monitor-port. Assuming a BGBW of 50 MHz, the total ASE power at the relevant wavelengths varied between 14.5 nW and 365 nW.

For each level of ASE power injected, the forward as well as the backward power and optical spectra were measured. In order to evaluate the evolution of the backscattered power and of the power of the Stokes-maximum, the power within the amplified narrowlinewidth signal was calculated from the measurement of the overall output power and the optical spectra. Figure 3.9 (a) shows the evolution of the backscattered power with respect to the signal power for four different levels of artificially added ASE. The amplified signal

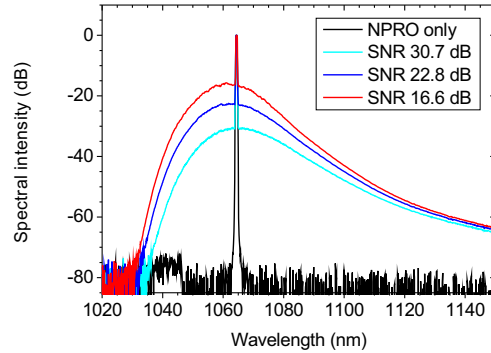


Figure 3.8: The optical spectra of the amplifier seed for four different power levels of artificially added ASE. The SF signal power was kept constant throughout the measurements. Resolution bandwidth: 0.5 nm.

power was limited in each case by parasitic lasing processes. Note that the threshold of parasitic lasing increased with increasing ASE power. No significant difference in the exponential rise of the backscattered power could be observed.

Table 3.3: The ratio of the SF signal and the artificially added ASE in forward direction and corresponding power within the BGBW. The resolution bandwidth of the optical spectrum analyzer was set to 0.5 nm.

SNR	Power within BGBW
30.7 dB	14.5 nW
22.8 dB	91.4 nW
16.6 dB	365 nW

Furthermore, the evolution of the Stokes-maximum was compared for the same power levels of injected ASE. This is shown on a logarithmic scale in Fig. 3.9 (b) with respect to the signal power. Again, no significant difference in the rise of the Brillouin scattered power could be observed.

The limitations of the experimental setup were, as mentioned above, the available ASE power and parasitic lasing of the fiber amplifier. However, the following conclusions can be drawn from the results. Comparing the evolution of the backscattered power and the power in the Stokes peak line for the three cases of different amounts of added ASE power yields no hint that the SBS-threshold was reached at different amplified signal power levels. For the sake of completeness it should be mentioned that when no additional ASE was injected, the amplifier was already limited at an output power of about 1.5 W. At this power level, the amount of Brillouin scattered power was still significantly lower than at an output power of 2.5 W, which could be extracted when more ASE was injected. However,

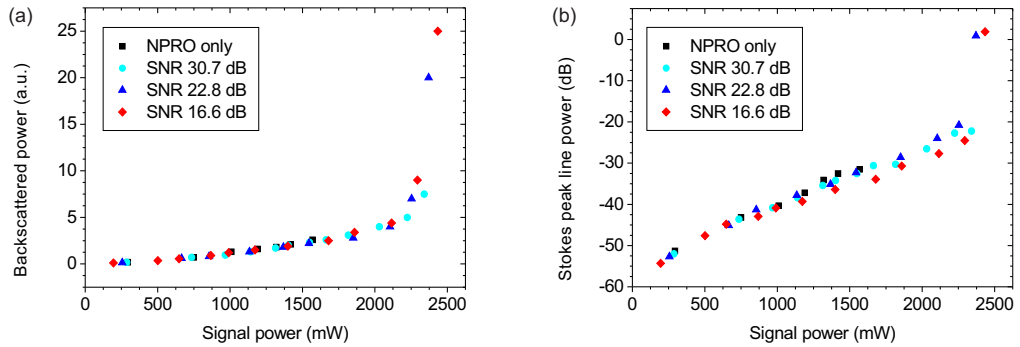


Figure 3.9: (a): Backscattered power and (b): SBS peak line power with respect to the signal power for different ratios of SF signal and artificially added forward ASE in the BGBW.

the evolution of the overall backscattered power and the power in the Stokes peak line was – according to Fig. 3.9 (b) – identical for all levels of added ASE. Therefore, a higher SBS-threshold for the case when no additional ASE was injected is not expected either.

Secondly, setting up a different, more powerful ASE source will eventually yield power levels within the BGBW high enough to decrease the SBS-threshold. However, the utilization of a seed source with a signal-to-noise ratio of less than 15 dB (OSA RBW: 0.5 nm) for a high power fiber amplifier is a very unlikely, if not even pathological configuration, and the general effect has been demonstrated in Section 3.2.

3.4 Conclusion

This Chapter focused on the impact of ASE on the Brillouin scattering of a SF signal. Numerical calculations using a rate-equation model that had been previously proven to be able to adequately simulate SF fiber amplifiers were carried out. In Section 3.1 it was demonstrated that the inclusion of a term accounting for ASE in the differential equation for the Brillouin power yields a decreased SBS threshold power level compared to the calculation without this term. Consequently, to adequately model a SF fiber amplifier, a term accounting for ASE needs to be included in the differential equation for the Stokes power.

The observed effect was explained by the seeding of the SBS process by ASE photons at wavelengths within the BGBW, generated in the amplifier fiber and co-propagating to the Stokes signal. Analytically calculated and experimental results supporting this assumption were presented in Section 3.2. There it was shown in a passive fiber that ASE within the BGBW can increase the strength of the Brillouin scattering process and therefore decrease the SBS-threshold, when it propagates in the same direction as the Brillouin scattered light. This statement was supported by a decreased signal power level necessary to reach the 0.1% reflectivity, defined as the SBS threshold power level, when more and more

ASE was added. Moreover, the total amount of backscattered power at a given signal power level and the height of the Stokes peak line in the backward detected optical spectra increased at higher added ASE power levels. In the experimental configuration used, their values were up to about 19 times as high, compared to the case, when no ASE was added.

Considering a fiber MOPA system with gain factors of several 10 dB, the ASE generated in the backward direction in the power amplifier fiber can be quite high and therefore possibly seed the SBS process. This in turn could contribute to the fact that increasing the seed power for a fiber amplifier increases its SBS threshold. Previously, this has been attributed only to the reduction of the gain factor [149]. Hence, concluding from the above described effect, a few Watt signal from a SF source should be preamplified to a few tens of Watts, before seeding a power amplification fiber stage, where a few hundred Watts are supposed to be extracted.

As this in turn leads to the injection of ASE photons from the preamplification stage into the high power amplifier fiber, the eventuality that Rayleigh-backscattered ASE from such a fiber-based preamplification stage could seed the SBS process of a fiber amplifier was investigated. These experiments were performed with a SF signal and artificially added ASE in the forward direction, seeding a typical low-power fiber amplifier. The results were presented in Section 3.3. No effect was observed decreasing the ratio of the SF power signal to the ASE at signal wavelength in the optical spectrum to 16.6 dB (OSA RBW: 0.5 nm). As the effect depends on the amount of the Rayleigh scattered light and spurious reflections in the backward direction, and therefore on fiber composition and length, the obtained results are not representative for any arbitrary fiber amplifier. Nevertheless, a fiber amplification stage employing a comparable standard fiber should not show a performance degradation in terms of a lower SBS-threshold, if the seed contains ASE from a preamplifier; at least as long as the ASE suppression is higher than 15 dB (OSA RBW: 0.5 nm).

The results presented in this Chapter have demonstrated that the ASE photons within the BGBW and co-propagating to the Stokes signal that are generated in a fiber amplifier are more likely to decrease the SBS threshold than Rayleigh backscattered ASE photons injected from a fiber preamplifier. From this point of view it is advisable to use higher seed power levels to increase the SBS threshold of a high power fiber amplifier. In fact, increasing the seed power yields even another advantage, as it decreases the sensitivity towards parasitic lasing processes. Unfortunately, it also decreases the temperature gradient within the amplifier fiber, which counteracts a high SBS threshold [81]. Therefore, for a finally constructed laser source for GWD application, the exact configuration in terms of preamplification power levels and the resulting SBS threshold will have to be evaluated in detail.

4 Beam quality characterization of single-frequency signals

As explained in the introduction to this thesis, interferometric gravitational wave detectors have a strong requirement regarding the beam quality of potentially applied laser sources, namely a high fundamental Gaussian mode content. Therefore, a method to measure the overlap of a SF laser beam with the fundamental Gaussian mode had been developed [152]. A brief description of its setup and working principle is given in Section 4.1. Applying this measurement technique, modal decompositions of signals transmitted through passive versions of the LMA fiber types presented in Chapter 2.3 were carried out (Section 4.2). These fibers have, up to now, the largest core diameters available of their fiber design type. Their performance is of interest, when all-fiber system integration or the utilization of delivery fibers is considered. Furthermore, in Section 4.3 different reasons for beam quality degradation of amplified signals in active fibers are explained. In particular, the phenomenon of transverse modal instabilities is discussed and the utilization of three new methods to characterize this effect is investigated.

4.1 Beam quality measurement methods

Most commonly, the laser beam quality is characterized by the so called M^2 value [153]. This value is obtained by focusing the beam and measuring its caustic. A perfect fundamental Gaussian beam yields the smallest focal beam waist and lowest possible M^2 value of one. However, M^2 values < 1.1 still allow for the fraction of higher order mode content to be as high as 30 % [22].

To investigate the modal composition of a fiber output beam, the so called S^2 method can be applied [154]. It is based on spectrally and spatially resolving the mode interference pattern of a broadband signal transmitted through the fiber under test. This measurement technique can not be employed to a beam in amplifier or oscillator operation, and does not work for SF signals. The same problems apply to an interferometric method in the time domain [155]. Other characterization techniques are based on measuring intensity profiles only [156], or additionally employing either computer generated holograms [157] or wavefront measurements [158]. As the modal power content is iteratively calculated, these methods unfortunately depend on the accurate knowledge of the fiber modes. Furthermore, the overlap of the beam with the fundamental Gaussian mode can not be directly measured and its calculation also relies on the knowledge of the fiber modes. Moreover, as explained in the introduction to this thesis, for GWD applications, the TEM_{00} mode is explicitly required, but none of the above mentioned techniques is suitable to analyze the TEM_{00} mode overlap of a beam.

The beam quality of a SF signal in terms of its modal decomposition can be investigated by employing a nonconfocal scanning ring cavity. In particular, the overlap with the fundamental Gaussian mode can be directly measured, if the cavity eigenmodes are by design the free-space TEM_{nm} modes [152]. The cavity used in all the experiments presented in the following Sections and Chapters is schematically shown in Fig 4.1. It had a free-spectral range (FSR) of 715 MHz and the finesse was about 200 at 1064 nm. One of the three mirrors was attached to a piezoelectric transducer. By injecting a ramp signal to it, the cavity length and hence the resonant eigenmode can be selected and is transmitted, while all other modes are reflected. Injecting a SF signal leads to the transmission of only one distinct transverse mode, as their resonant lengths differ due to their respective Gouy phases [159]. Hence, a modal decomposition of a SF signal with respect to the TEM_{nm} modes can be obtained. A more detailed description can be found in Ref. [152].

Mode-matching to the fundamental mode of the cavity was achieved with two lenses of different focal lengths. Careful alignment with two 45° -highly-reflective (HR) mirrors was necessary. The power level required in front of the cavity was about 120 mW. In the following Sections and Chapters, this measurement setup will be referred to as diagnostic breadboard, short DBB.

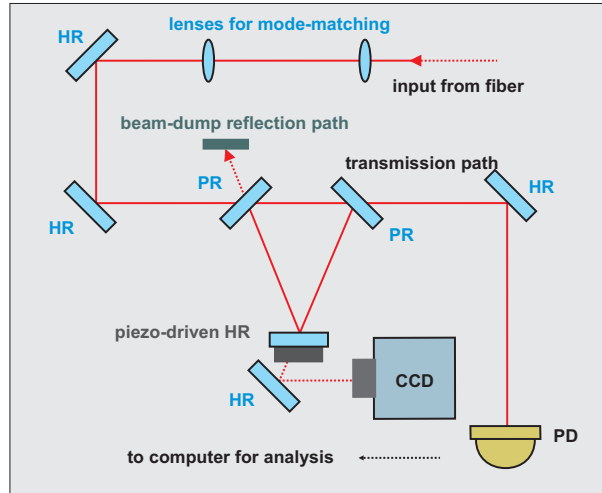


Figure 4.1: Experimental setup of the three mirror nonconfocal ring cavity (diagnostic breadboard, short DBB) as well as the optics in the signal-input and the cavity-transmission path. HR: Highly-reflective mirror, PR: partial reflector.

4.2 Fundamental Gaussian mode content of passive double-clad LMA fibers

The measurement setup for the passive LMA fiber characterization is depicted in Fig. 4.2. The SF signal with a nominal linewidth of about 1 kHz at a wavelength of 1064 nm was

provided by an NPRO. It was transmitted through a 10 μm core diameter fiber of a PM single-mode preamplification stage, whose fundamental fiber mode has a TEM_{00} mode overlap of 97% [160]. Behind this fiber, the PER was measured to be ≥ 20 dB. The signal was mode-matched to the fiber under test, and again collimated after propagating through the fiber. In case of the non-PM fibers, a quarter waveplate was employed to linearize the output polarization. The half-waveplate and the polarizing beam splitter (PBS) were used to measure the polarization extinction ratio (PER) and to reject the residual orthogonal polarization component as the DBB (Section 4.1) requires the signal to be linearly polarized. Throughout the experiment, mode-matching was achieved with the same pair of lenses for one fiber and the signal-to-fiber coupling was optimized. A high-index matching gel was utilized to remove any light from the pump-cladding of the step-index and CCC fibers as well as the outer cladding of the PCF. To separate the core signal from the light accidentally launched into the inner cladding of the PCF, an aperture was used.

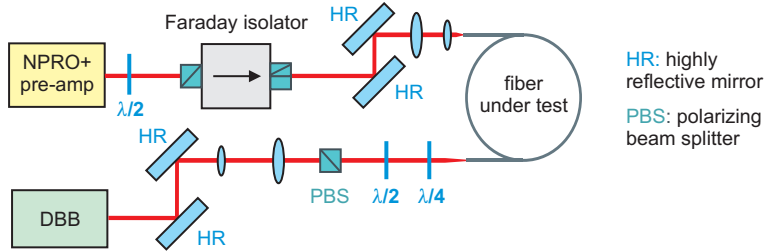


Figure 4.2: Experimental setup for measuring the fractional TEM_{00} mode content of a SF signal transmitted through different passive LMA fibers with the DBB described in Section 4.1.

4.2.1 Standard step-index fibers

The few mode step-index large mode area fibers under test had nominal core diameters of 30 μm and core NAs of 0.06. Resulting MFD and V-number (Eq. 2.12) were about 23.5 μm and 5.315, respectively. 1.8 m long samples of both PM and non-PM versions (LMA-GDF-30/250 and PLMA-GDF-30/250 by Nufern) were tested. The coiling diameter was set to 10 cm, 15 cm and 20 cm for each of the fibers, and the beam quality was very sensitive to the signal-to-fiber coupling in each case. By monitoring the output beam profile it was possible to excite distinct HOMs just through alignment. Optimizing the alignment with respect to fundamental mode excitement, the highest TEM_{00} mode content was obtained for both fiber versions for a coiling diameter of 15 cm. It was 95.6% for the non-PM version and 96.3% for the PM-fiber. For coiling diameters of 10 cm and 20 cm the obtained modal overlap values were between 94% and 95%.

Fig. 4.3 (a) shows the obtained mode scan for the PM-fiber, coiled to a diameter of 15 cm. The normalized cavity transmission is plotted with respect to the FSR on a logarithmic scale. In theory, for a perfect TEM_{00} mode overlap, only peaks at 0.0 and 1.0 FSR would

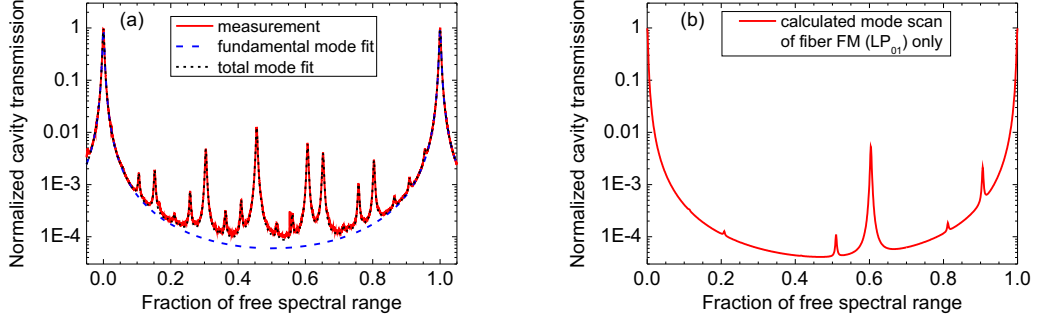


Figure 4.3: (a): Mode scan result for 1.8 m of the PLMA-30/250 (coiling diameter: 15 cm) on a logarithmic scale. The corresponding HOM content, calculated from the total mode fit, was only 4.4%. (b): Calculated TEM_{nm} modal decomposition for a beam, containing only the LP_{01} mode of the (P)LMA-GDF-30/250 fiber, optimized regarding a maximum TEM_{00} mode content.

be present (blue dotted line: fundamental mode fit). In reality, due to slight misalignment and mode mismatching, a few more peaks, corresponding to different distinct HOMs appear (red solid line: measurement). In particular, the peak at 0.3 FSR corresponds to mode mismatching, while the peaks at 0.15 FSR and 0.65 FSR indicate relative misalignment in the vertical and horizontal direction. These attributions are straightforwardly identified by comparing the sensitivity of the peak height to slight changes either of the lens positions or HR-mirror adjustment. The HOM peaks seem to be quite high in the graph due to the logarithmic scale, but their power levels were very low in this case. In fact, the total mode fit, which has a very good overlap with the measurement, contained only 4.4% of the power in HOMs.

The theoretical upper limit of the measurable TEM_{00} mode content is given by its overlap with the fiber's fundamental mode (FM). In order to obtain this value, first the electric fields of these modes need to be calculated. For the TEM_{nm} modes, the field distributions are given in several textbooks, e.g. in Section 3.1.5 of Ref. [37]. Solving Eqs. 2.9 and 2.10 with proper parameters yields the fundamental mode of the particular fiber design. Finally, the overlap integral of the modes is evaluated in the beam waist, while the beam width of the fiber's FM is optimized with respect to the maximum TEM_{00} mode content [161]. The calculated TEM_{nm} modal decomposition for a beam containing only the LP_{01} mode of the (P)LMA-GDF-30/250 is depicted in Fig. 4.3 (b). There is one predominant HOM peak at about 0.6 FSR and smaller ones at 0.5 FSR as well as 0.9 FSR, even though the corresponding TEM_{00} mode content is 99.2%. These HOM peaks also contribute to the deviation from an ideal TEM_{00} mode overlap of the measured signal (Fig. 4.3 (a)).

Fig 4.4 (a) shows the calculated mode-scan for a beam containing 90% of the power in the LP_{01} mode and 10% in the LP_{11} mode. The peaks at 0.45 FSR, 0.75 FSR and 0.8 FSR

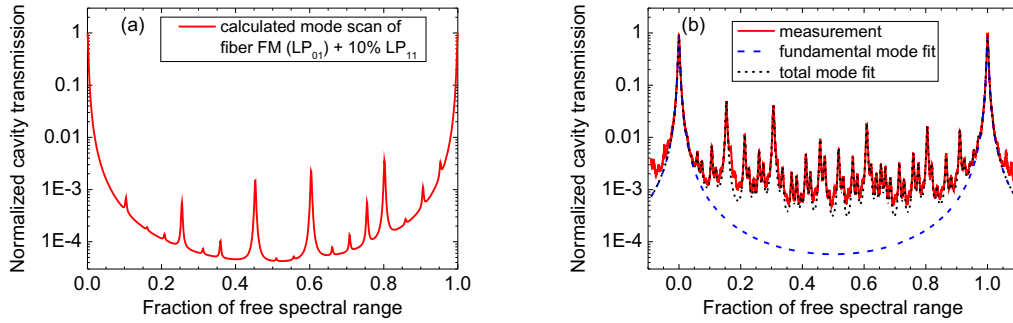


Figure 4.4: (a): Mode-scan, calculated for a beam containing 90 % of the power in the LP₀₁ mode and 10 % in the LP₁₁ mode of the (P)LMA-GDF-30/250 fiber with maximized TEM₀₀ mode content. (b): Exemplary measured mode scan with 20 % of the power distributed in several HOMs.

also appear in the measured scan in Fig. 4.3 (a), and indicate the presence of the LP₁₁ in the beam, transmitted through the PLMA-GDF-30/250 fiber. It also demonstrates that in order to obtain a good overlap with the TEM₀₀ mode (here: >95 %), a fiber does not need to be intrinsically single-mode. For applications such as GWDs, however, the latter is highly desirable, as slight changes in the relative phases between two modes can lead to effects such as beam pointing.

An exemplary mode scan in case of 20 % HOM content is shown for comparison in Fig. 4.4 (b). The total mode fit shows a good overlap with the measured scan, but much more HOM peaks are present and the offset to the fundamental mode fit is quite high. For all mode scan results presented in this thesis, it was checked that the total mode fit, from which the applied iterative algorithm calculated the HOM content, had a good overlap with the measured scan. In case of an offset, the fundamental mode content was calculated manually by integrating the areas under the fundamental fit and the measured curve and subtracting the former from the latter.

4.2.2 Photonic crystal fiber

The analyzed PCF (DC-200/40-PZ-Si by NKT Photonics) had a nominal core diameter, core NA and MFD of 40 μm, 0.03 and 30 ± 2 μm. Applying Eq. 2.33, this yields a V-value between 2.481 and 2.835. Hence, the fiber was intrinsically multi-mode, although the manufacturer advertises it as strictly single-mode. Two boron stress rods ensured linear polarization output, if the input polarization was launched in the right fiber axis. The pump cladding had a diameter of 200 μm and a nominal NA of 0.55. It was surrounded by an air-clad and an outer silica cladding with a diameter of 450 μm. For mechanical stability, the fiber was coated with a high temperature acrylate. A microscope image of the fiber's cross-section is shown in Fig. 4.5 (a).

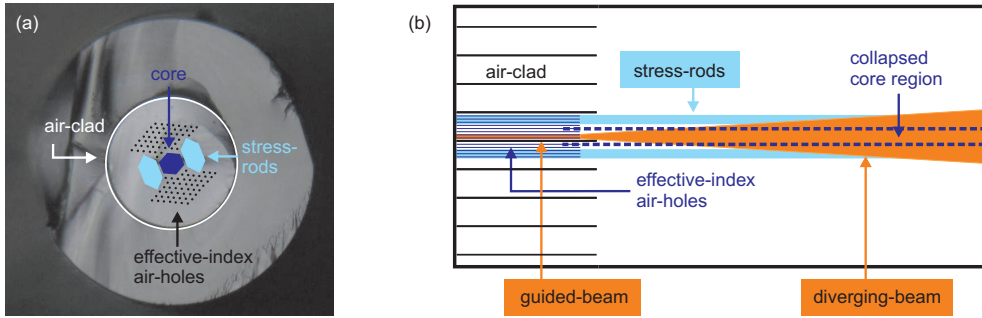


Figure 4.5: (a): Microscope image of the PCF’s cross-section. The air-hole structures enable low core and high pump cladding NAs, but make the fiber end preparation and splicing a challenging task. Note that the cracks are due to manual cleaving. The presented results were obtained with sealed and polished end facets. It can be clearly seen that the stress-rods are very close to the core region. (b): Schematic side-view of the PCF. The horizontal black and blue lines represent the air-holes of the air-clad and for the effective index-guidance, indicating that the smaller holes around the core collapse further than the air-clad holes. If the collapsed region is too long, the diverging beam enters the region of the boron-doped stress rods.

As the air-hole structures are very sensitive to capillary effects, the fiber ends need to be sealed. Collapsing the air-holes however can potentially affect the beam quality. This is illustrated in Fig. 4.5 (b). The beam diverges in the part of the fiber, where the air-holes that otherwise enable effective-index guiding are collapsed. If the beam diameter gets larger than the core, it would enter the region of the boron-doped stress rods. These in turn possess a slightly higher refractive index than the silica-cladding and cannot guide any light. Consequently, the diverging beam gets “squeezed” by the stress-rods and its shape becomes slightly elliptical. To prevent this beam deformation, the collapsed region must be kept as short as possible. The minimum collapse length however is determined by the collapsed air-holes of the air-clad structure, which might not collapse as far as the effective-cladding air-holes due to their larger diameter.

To get a theoretical estimate about the TEM_{nm} modal decomposition of a beam transmitted through this PCF, its fundamental mode was calculated by solving Eq. 2.9 with the effective PCF indices described in Section 2.3.1. The calculated mode scan with respect to a maximized TEM_{00} mode content is presented in Fig. 4.6. There is one predominant HOM at about 0.6 FSR, just as for the (P)LMA-GDF-30/250, but it is smaller than in the case of the latter fiber (Fig. 4.3 (b)). The same holds for the HOMs located at 0.51 FSR and 0.81 FSR, while the power in the HOM peak at 0.9 FSR is roughly the same. Only the HOM located at 0.2 FSR contains slightly more power, compared to the calculated fundamental mode decomposition of the (P)LMA-GDF-30/250. Nevertheless, the overall TEM_{00} mode overlap of the PCF’s fundamental mode is just 0.5 % higher than for the step-index fibers, i.e. 99.7 %.

Measurements were carried out for different bending diameters and different collapsing lengths. For a collapsed length of 100 μm the TEM_{00} mode contents were measured to be

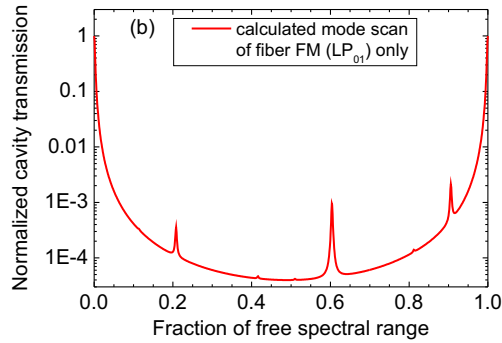


Figure 4.6: Calculated modal decomposition of the PCF DC-200-40-PZ-Si fundamental mode with respect to a maximum TEM_{00} mode overlap.

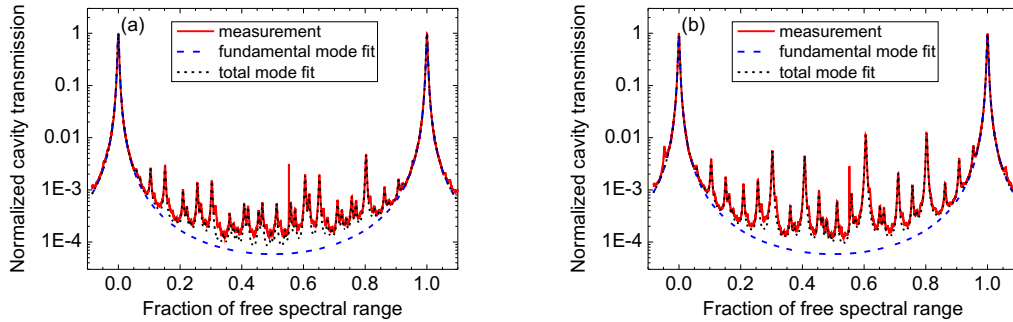


Figure 4.7: Mode scan for 2.54 m of the PCF, with a coiling diameter of 32.4 cm and an air-clad collapse length of (a): 100 μm with a corresponding TEM_{00} mode content of 97% and (b): 700 μm with a corresponding TEM_{00} mode content of 94.2%. For the latter, it was not possible to obtain a higher overlap, as the beam got distorted when propagating through the long collapsed region.

96.5% and 97% for bending diameters of 69 cm and 32.4 cm, respectively. The fiber length was 2.54 m and the signal transmission was not sensitive to the coiling diameter within this bending range. Increasing the collapsed length to 700 μm led to a slightly elliptical beam profile, decreasing the overlap with the TEM_{00} mode to 94.2% at a bending diameter of 32.4 cm. This is most likely due to the fact that the diverging beam in the collapsed region gets distorted by the boron-doped stress rods. The obtained mode scans for a bending diameter of 32.4 cm are presented for 100 μm collapsing length (Fig 4.7 (a)) and 700 μm (Fig 4.7 (b)) and show a good overlap with the total mode fit. Misalignment of the signal-to-fiber coupling led to an increase of power transmitted through the cladding, but the beam quality of the signal transmitted through the core did not decrease. The measured PER was always around 14 dB, deviating only slightly from the nominal value of 15 dB [162]. This is most likely caused by residual inner cladding light.

4.2.3 Chirally coupled core fiber

The parameters of the CCC fiber under test, which was kindly provided by Prof. Galvanauskas from the University of Michigan, can be found in Table 4.1. A microscope image of the fiber's cross-section is shown in Fig. 4.8. Eight satellite cores surround the central core, in which only the fundamental fiber mode is guided. All HOMs are pulled out of the core, due to a high overlap with the satellite core modes through proper choice of the satellite core parameters and helix period (Section 2.3.2).

Table 4.1: Parameters of the passive large core CCC fiber.

core diameter, NA	55 μm , 0.07
MFD, cladding diameter	42 μm , 500 μm
calc. V-number	11.368
number of satellite cores	8
satellite core diameter, NA	10 μm , 0.09
helix period	5.3 mm
edge-to-edge distance of central core and side cores	7 μm

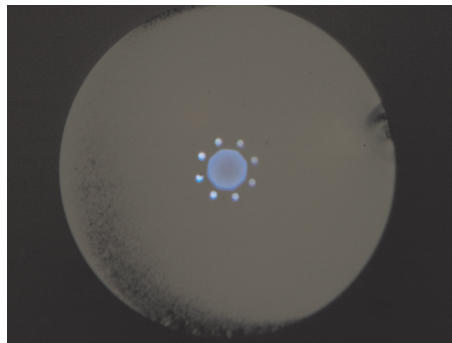


Figure 4.8: Cross-sectional microscope image of the CCC fiber under test. The large central signal core (diameter of 55 μm) is surrounded by 8 satellite cores.

The calculated mode scan of the CCC-fiber's LP_{01} mode is depicted in Fig. 4.9 (a). It corresponds to a TEM_{00} mode overlap of 98.5%. The FSR-localization and relative power content of the HOMs is very similar to the modal-decomposition calculation of the (P)LMA-GDF-30/250 fiber. This can be most likely traced back to step-index structure of the CCC-fiber without the satellite cores, which were not included in the FM calculation. Due to the logarithmic scale, the HOM peaks in Fig. 4.9 (a) appear to be significantly higher than for the step-index fibers (Fig. 4.3 (b)), but the corresponding TEM_{00} mode overlap is still 98.5%.

1.8 m of this fiber were tested with three coiling diameters within the recommended

range. Changing the coiling diameter from 50 cm to 40 cm decreased the transmitted signal power by about 20 %, which is not a significant number, considering that the signal-to-fiber coupling can typically vary by $\pm 10\%$. However, coiling the fiber with a diameter of 30 cm further reduced the transmitted signal power by 70 % compared to 40 cm diameter coiling diameter and the transmission got sensitive to bending, twisting and external pressure. Apparently, the losses for the fundamental mode increased significantly at this coiling diameter, even if assuming a slight misalignment of the signal coupling. Otherwise there was no difference in the fiber performance. The measured PER was always higher than 20 dB and the mode scans yielded an overlap with the TEM_{00} mode from 96.5 % to 97.1 %. A representative mode scan is shown in Fig. 4.9 (b). It was measured with a coiling diameter of 30 cm and corresponds to a TEM_{00} mode content of 97.1 %. Additionally to the HOMs that can attributed the fiber's FM, some other HOM peaks appear, although their relative power content is very low. Again, the peaks located at 0.15 FSR and 0.65 FSR are due to slight misalignment in the vertical and horizontal cavity direction, while the presence of the HOM peak at 0.3 FSR indicates relative MFD mismatching. The HOMs located at 0.45 FSR, 0.55 FSR and 0.75 FSR could be caused by the presence of higher order fiber modes in the beam.

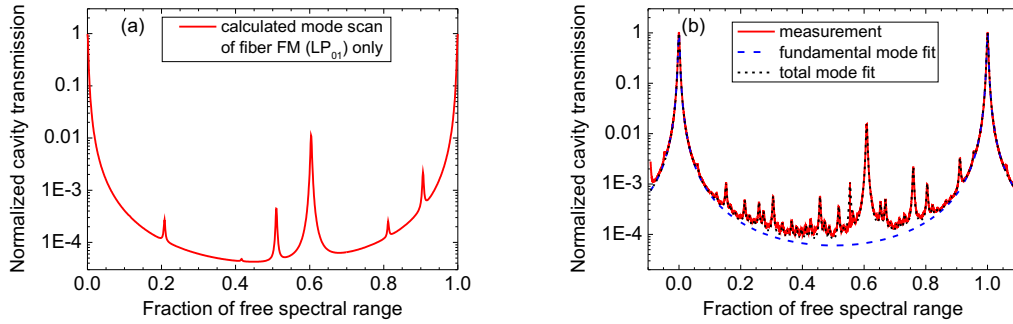


Figure 4.9: (a): Result of the TEM_{nm} modal decomposition calculation for the CCC-fiber's fundamental mode, with maximized TEM_{00} mode overlap. (b): Representative mode scan on a logarithmic scale of a beam transmitted through 1.8 m of the CCC fiber, coiled with a diameter of 30 cm. The corresponding overlap with the TEM_{00} mode was measured to be 97.1 %.

The modal decomposition of the beam transmitted through the CCC-fiber under test was not sensitive to the signal-to-fiber coupling. Slight misalignment of it led only to less power coupled to the fundamental mode, decreasing the fiber transmission. HOMs could not be further excited. Therefore, it can be concluded from these results that this all-solid fiber can be considered truly single-mode with an impressively large mode field diameter.

4.2.4 Conclusion

In conclusion, the TEM_{00} mode overlap of beams transmitted through passive CCC, step-index, and photonic crystal fibers with core diameters of $55\ \mu\text{m}$, $30\ \mu\text{m}$ and $40\ \mu\text{m}$, respectively, was investigated. For all fibers, the electric field distribution of the fundamental mode was calculated and the theoretical overlap with the TEM_{00} mode evaluated. The calculated modal decompositions of the fiber fundamental modes with respect to a maximized TEM_{00} mode overlap demonstrated the influence of the fiber geometry. The PCF, possessing the lowest NA and V-value, yielded the best theoretical TEM_{00} mode overlap, i.e. 99.7 %. For the fibers with higher NAs and V-values, the (P)LMA-GDF-30/250 as well as the CCC fiber, more HOM peaks appeared in the calculated mode-scans, even though the overall TEM_{00} mode content was still 99.2 % and 98.5 %, respectively. The impact of the fiber NA and V-number on the modal shape and thus on the overlap with the TEM_{00} mode is illustrated in Fig. 4.10. If the NA of a fiber and consequently the index step is higher than for fiber parameters, yielding the best overlap with the Gaussian fundamental mode (green curve), the evanescent field of the mode is more confined in the core (red curve). Lower NA and index-step values yield an evanescent mode field that penetrates deeper into the cladding (blue curve). In both cases, the overlap with the fundamental Gaussian mode is reduced.

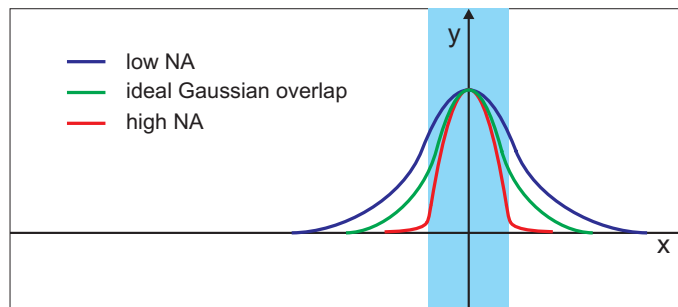


Figure 4.10: Sketch of the transverse intensity distribution for an ideal fundamental Gaussian mode (green curve), as well as modes that either penetrate deeper into the cladding due to a lower NA (blue curve) or are more confined in the core due to a sharper index step (red curve). The blue-shaded area indicates the core region.

TEM_{00} mode contents larger than 96.3 % could be obtained. While both the CCC fiber as well as the PCF behaved like truly SM-fibers, for the step-index fiber HOMs could get easily excited through external perturbations. The beam quality of the PCF under test was only sensitive to the fiber end preparation, but the MFD was just about $30\ \mu\text{m}$. The largest MFD under test was provided by the CCC fiber. It enabled a single-mode $42\ \mu\text{m}$ MFD, qualifying it as possible passive beam delivery fiber, e.g. for GWD applications.

Nevertheless, in terms of power scaling a SF signal with active fibers, a few things need to be considered, as the CCC fiber was single-clad and passive. Implementing a double-clad structure always enables the guiding of HOMs. Doping the fiber changes

the core's refractive index, so that the fabrication process in terms of controlling the different modes' effective refractive indices and hence their propagation constants could be further aggravated. Therefore, the TEM_{00} mode overlap of such a fiber with gain and heat load can not be anticipated from the results presented in this Section and must be experimentally studied in detail.

4.3 Beam quality degradation and transverse modal instabilities of amplified signals

As analyzed in Section 4.2, single-mode operation of passive large core few-mode fibers can be achieved with external or intrinsic HOM suppression. At least in principle, the same holds true for active fibers. However, in amplifier operation, the implications of gain as well as thermal issues need to be considered. Saturation effects usually lead to an improved beam quality with increasing pump power [163, 164]. At power levels where thermal effects are still small, transverse spatial hole burning (TSHB) can affect the beam quality [163]. It can either enhance or suppress the growth of a HOM, depending on the HOM's coherence and polarization relative to the fundamental mode [164, 165].

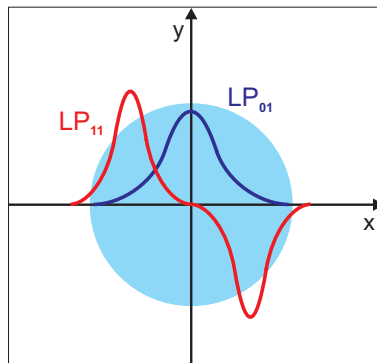


Figure 4.11: Electric field distributions of the LP_{01} and the LP_{11} mode in the transverse (xy-) fiber plane. The LP_{11} mode can deplete the inversion (represented by light-blue circle in the background) in core regions that are not saturated by the intensity of the LP_{01} mode.

If the excited HOM is polarized orthogonally to the fundamental fiber mode, no modal interference will take place. The typically Gaussian-like fundamental fiber mode (Section 2.1.3) yields a less depleted upper state population towards the core edges, giving rise to TSHB. As illustrated in Fig. 4.11 for the LP_{11} mode, the HOMs typically possess a higher intensity in this outer core region and can be amplified by the excess gain. Due to the small amount of initial power in these modes (usually, they are rather accidentally excited, caused by slight misalignment and mode mismatching with respect to the FM), they experience a higher gain and are preferentially amplified compared to the saturated fundamental mode. In case of parallel polarized modes, interference can occur, and the transverse intensity profile gets asymmetric in the plane of the lobes of the LP_{11}

mode. Saturation is higher, where the intensity maximizes, i.e. the two modes interfere constructively. As a consequence, the gain is higher on the core side, where the mode fields interfere destructively. After propagation through the fiber, the resulting amplified field is slightly less asymmetric, which corresponds to a lower HOM power fraction compared to the initial field. This is equivalent to a suppression of the HOM [165]. External TSHB suppression can be achieved by tandem cladding-pumping of the amplifier fiber [166] or by confining the doped region in the center of the core [165, 167].

Furthermore, the Gaussian-like fundamental fiber mode can induce a parabolic index profile in the radial direction across the core, either through the resonant change of the refractive index [168] or via the thermo-optic effect [169]. As a consequence, the MFD of the fundamental fiber mode decreases with increasing pump power [170]. In PCFs, where the fundamental mode usually has hexagonal features due to the arrangement of the air-hole structure at low power levels, the shrinking of the MFD can lead to an increased beam quality, as the hexagonal features become weaker with increasing pump power [170]. Unfortunately, this counteracts the technologically achieved fundamental MFD enlargement and therefore represents another power scaling limitation. Additionally, if the MFD gets smaller than the doped region of the core, TSHB can become an issue, especially in the backward pumped case [171]. Further advancement in fiber design is therefore necessary to precompensate for this effect. For bend fibers such an asymmetric index profile precompensation has been theoretically investigated [172]. The feasibility of its production process is still to be seen.

Even though the previously described temperature induced parabolic index profile occurs in the transverse fiber plane, some implications arise in the longitudinal fiber direction. Due to the longitudinal temperature gradient, the radial index perturbations change along the fiber's z-axis and accordingly the guiding properties change. Consequently, different modes are guided at different longitudinal positions, yielding a varying number of guided modes along the fiber [171]. Potentially, a truly single-mode fiber can eventually become multi-mode at very high pump powers.

Today, the probably most fundamental power scaling limitation of Yb-doped fiber amplifiers (CW as well as pulsed) is commonly referred to as mode instabilities (MI) or transverse modal instabilities (TMI). The current status of significant experimental observations, proposed physical theories and numerical modeling results is summarized in Subsection 4.3.1. Experimental setups, procedures and results of the investigations carried out within the framework of this thesis are described in Subsection 4.3.2. Concurrences and deviations to the experimental and numerical results from other groups are discussed in Subsection 4.3.3. Finally, Subsection 4.3.4 consists of an overall conclusion and some key remarks on this issue.

4.3.1 Transverse modal instabilities (TMI)

TMI manifest themselves in a sudden onset of beam quality degradation, from nearly single-mode to chaotic multi-mode behavior, at a sharp threshold power level. Representative

near field images of the optical intensity profile, in this case emitted from a PCF amplifier just beyond the TMI threshold, are depicted in Fig. 4.12 (a) to (d). Reported threshold powers vary from a few hundred watts to a few kilowatts [170, 173], depending strongly on the particular fiber geometry and amplifier configuration. Nevertheless, TMI have been observed in different fiber types (PCFs [174] and step-index fibers [175]), and in co- as well as counter-pumped amplifier configurations [25, 176]. Parameters such as fiber length [25, 176], core diameter [170], and seed power [173] apparently influence the threshold power. CW- [173] and pulsed [175] systems are affected likewise, and the threshold power rather depends on the average power than on the peak power.

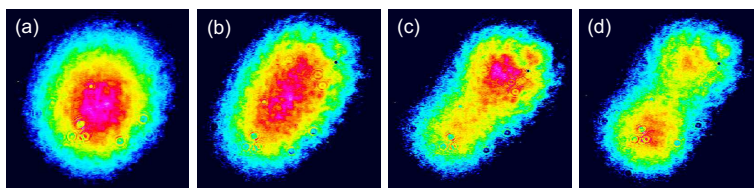


Figure 4.12: Representative snapshots of the fluctuating beam profile at the threshold power. It permanently changed from an LP_{01} -like mode (a) through intermediate states (b,c) to an LP_{11} -like mode (d) and back in a chaotic manner.

By reducing the amplifier power below the threshold level, the formerly excellent beam quality can be restored. However, a certain fiber degradation was found by several research groups, leading to a lowered TMI-threshold, every time the amplifier was turned up to the corresponding power level [177–179]. Such a “memory”-effect was also identified by Haarlammert et al [180]. Utilizing certain pre-, main-, and post-pulse configurations, they demonstrated the existence of a build up and decay time of the TMI on a millisecond time scale. Moreover, they could influence these build-up and decay times of TMI, even if the pre- or post-pulse was injected with an average power below the threshold power.

To get an insight into the dynamics of the MI process experimentally, Stutzki et al. developed a mode analysis technique, employing a high-speed camera and a modal decomposition algorithm [26]. These measurements revealed that complete energy transfer between the modes could occur during TMI, while the overall amplifier output remained stable. The timescale of the process was confirmed to be in the range of a few milliseconds. Hence, it is not sufficiently accurate to characterize the TMI dynamics with low-speed cameras or the naked eye. Consequently, Otto et al. measured time-traces with a photodiode behind an aperture, which was utilized to cut out a certain part of the beam, i.e. to convert the beam profile fluctuations into intensity fluctuations [181]. Furthermore, Fourier-spectra were calculated from the recorded time traces. As TMI threshold, the power level, where the first derivative of the standard deviation of the time traces reaches $0.1\text{‰}/\text{W}$, was defined [181]. This threshold power was found to be slightly lower than what could be anticipated from low-speed measurements. Mostly, power fluctuations between the LP_{01} and the two orientations of the LP_{11} mode have been observed, but this

seems to be rather fiber dependent [176, 182].

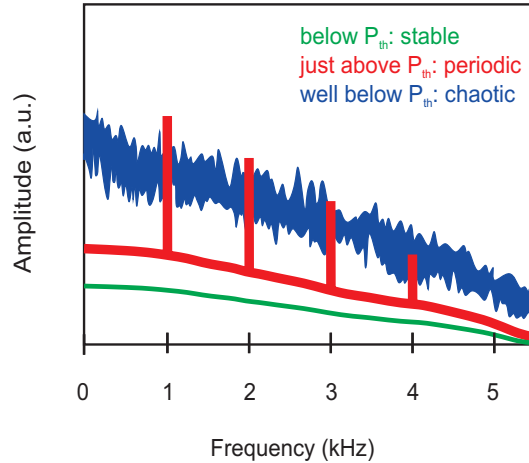


Figure 4.13: Fourier-transformed temporal intensity fluctuations, sampled at a small fraction of the transverse beam profile, below, at and well above the TMI threshold power level (P_{th}). Three different oscillation regimes can be clearly distinguished as stable, periodic and chaotic. The figure is drawn according to the results presented in Ref. [181].

Three different oscillation regimes were identified. They can be distinguished best by comparing the Fourier-spectra of the time-resolved intensity fluctuations, sampled from a fraction of the transverse beam profile, as schematically depicted in Fig. 4.13. Amplifier operation below the threshold was naturally referred to as the stable regime. Beyond this power level, the standard deviation of the time-signal started to increase exponentially and periodic peaks appeared in the frequency-spectra, whose central frequency slightly shifted with time. Aperture size and position on the other hand did not affect this center frequency. While the aperture position (i.e. at or off the beam center) only affected the magnitude of individual peaks, the size of the aperture was more critical for the measurement. In particular, the magnitude of all the frequency peaks decreased for an increasing aperture size, which agrees with the observation of an overall stable output power. When the pump power was further increased, the distinct frequencies disappeared, leading to a broadband noise spectrum. The corresponding time-trace became chaotically unstable. Consequently, this was named the chaotic regime, while the former was defined as transition region. A dependence of the involved frequencies on the core diameter was found. In particular, the broadband noise in the Fourier-spectra featured higher and higher frequencies with increasing fiber core diameter. This corresponds to a modal power transfer taking place on a smaller time-scale. These limits were compared to calculated values, related to the overall transverse thermal diffusion time. While calculated and measured frequencies matched in magnitude, they differed in their exact values.

The existence of the oscillation regimes was confirmed with similar time-trace measure-

ments by the groups of Ward et al. [183] and Jørgensen et al. [178]. Contrary to Ref. [181], the latter group observed a rather step-like increase of the time-signals' standard deviation than an exponential one. Moreover, changes in the frequency spectra of the transition region were measured, if the amplifier power was turned repeatedly to the threshold level. Interestingly, the harmonic peaks did not always appear, yielding broadband noise right at the power threshold.

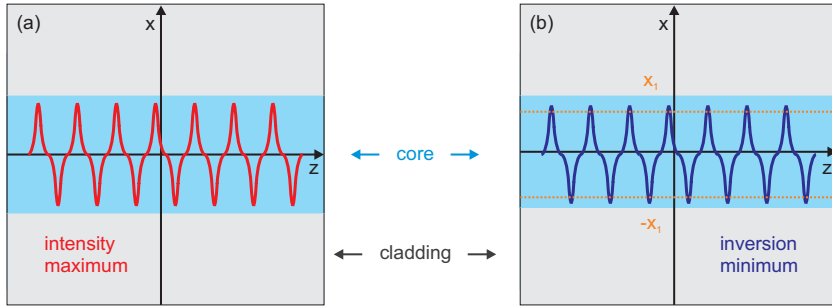


Figure 4.14: (a): The intensity maximum of the interference pattern between the LP_{01} mode and the LP_{11} mode oscillates in the transverse direction while propagating along the fiber (z : propagation axis). (b): This entails an oscillating local minimum of the population inversion in the transverse fiber plane.

Threshold power improvement was obtained for asymmetric conductive cooling [183], as well as improved fiber designs. These were based on gain-tailoring [184] and modal-filters as well as HOM delocalization [185]. As external mitigation technique, the utilization of an acousto-optic deflector to dynamically excite the fundamental mode at two different symmetric radial positions, was demonstrated [179].

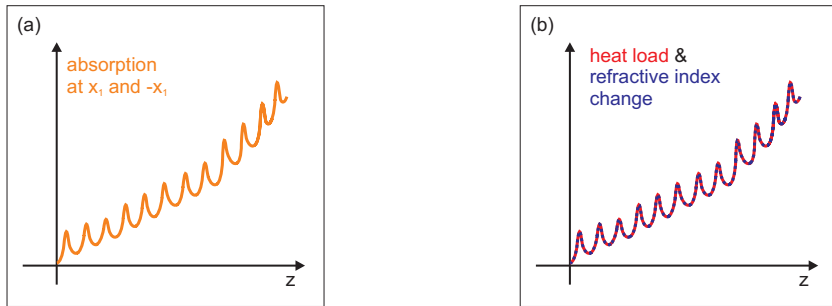


Figure 4.15: (a): Evolution of the absorption along the fiber, schematically illustrated for a counter-pumped amplifier. The radial asymmetry of the population inversion results in small oscillations on top of the overall increasing absorption towards the pump end, especially at the core edges (x_1 and $-x_1$). (b): Corresponding evolution of the deposited heat load and induced refractive index change along the fiber.

To explain the observed features of TMI, multiple theoretical models have been developed by different research groups [27, 183, 186, 187]. Combining the transversally resolved rate equations in the steady-state case with a 3D beam propagation method (BPM) it was first demonstrated by Jauregui et al. that TSHB alone cannot explain the observed effect [186]. Their modeling results showed what the scientific community has agreed upon to be an essential basic of the physical origin of TMI. Interference of the LP_{01} and LP_{11} mode (Fig. 4.11) yields a radially antisymmetric irradiance pattern along the principal fiber axis z (Fig. 4.14 (a)). This in turn causes the minimum of the population inversion in an active fiber to radially oscillate along the fiber's z -axis (Fig. 4.14 (b)). An alternating, periodic structure of local maxima and minima on top of the overall absorption evolution along the fiber's z -axis is created, whose oscillation depth is especially deep/strong at the core edges. This is schematically illustrated for a counter-pumped amplifier in Fig. 4.15 (a).

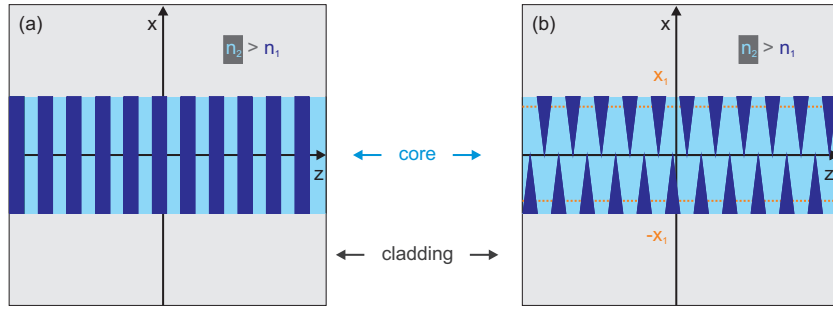


Figure 4.16: (a): Schematic sketch of a radially symmetric refractive index grating, as is the case for e.g. fiber Bragg or long-period gratings. (b): Radially antisymmetric index grating, thermally induced in the presence of interference between a symmetric and an anti-symmetric mode (e.g. the LP_{01} and the LP_{11}). n_1 and n_2 denote the alternating refractive index minima (dark blue) and maxima (light blue).

As a result, there are small oscillations of the heat load superimposed on its overall evolution along the fiber. The alternating heat-load in turn induces a refractive index grating through the thermo-optic effect [169] and the evolution of the refractive index changes follows the evolution of the heat load (Fig. 4.15 (b)). This longitudinal index grating is unlike long-period or fiber Bragg gratings (Fig. 4.16 (a)) antisymmetric in the transverse direction (Fig. 4.16 (b)) [27, 188]. In fact, the anti-symmetric part of the index-grating was found to be the principal contributor to TMI induced modal power transfer [189].

Smith et al. pointed out that even though this index grating has the right period, energy transfer between the modes creating it is not possible without a phase shift with respect to the interference pattern [27]. They suggest that a frequency-offset between the interfering modes exists, which would automatically produce the necessary phase shift. Regarding the origin of this phase shift, two “philosophies” have been developed. One of them assumes a frequency-shift between the interfering modes a priori, but the origin of this potential

initial frequency shift is still under discussion and subject to current research. Jauregui et al., on the other hand, follow the second “philosophy” (e.g. Ref. [28]). Even though they admit that such a frequency-offset induced moving grating might enhance the TMI process, they have focused their research on identifying other potential physical processes. Modal power transfer is assumed to be triggered by a quasi-static grating in the presence of a transient process, i.e. external perturbations or the increase of the pump power. This static grating is induced by interference of two modes with the same frequency, and a frequency-shift would be a consequence of the Doppler-effect in this case [190].

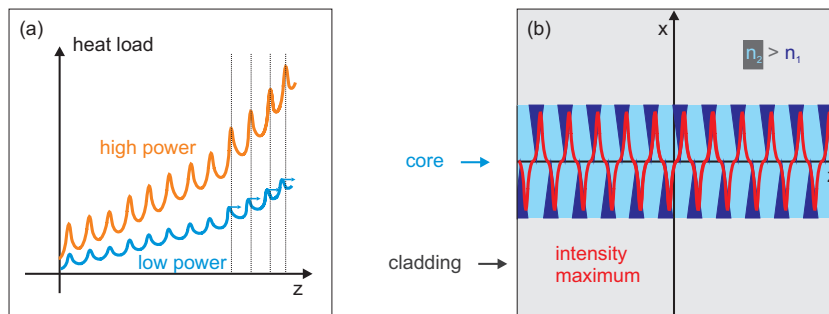


Figure 4.17: (a): The maxima of the deposited heat load move with increasing amplifier power towards the pump end of a counter-pumped fiber amplifier. (b): The irradiance pattern can not adapt itself fast enough to the resulting nonadiabatic waveguide changes and its maxima get delayed to the maxima of the refractive index changes (light blue). The figures are drawn according to Ref. [28].

The potential physical processes enabling modal power transfer from the FM to the HOM as proposed by Jauregui et al. in Ref. [28] is illustrated in Fig. 4.17 and was related to nonadiabatic waveguide changes. The denomination “nonadiabatic” indicates that the irradiance pattern interacts with a refractive index grating, whose shape and maxima localization is only partly induced by the interfering modes. This grating shape and maxima localization gets modified at high amplifier power levels by a resulting strong longitudinal temperature gradient. As a consequence, the heat load changes stronger within short distances compared to low power levels (Fig. 4.17 (a)). The local maxima of the heat load move towards the next minima, while the local minima are “pulled” towards the previous maxima. Hence, the oscillations on top of the overall heat load evolution along the fiber change from a quasi-sinusoidal to a rather “sawtooth”-like shape [28]. This brings the interference pattern and the index grating out of phase. Especially towards the pump end of the fiber (at least for counter-pumped amplifiers as shown in the example of Fig. 4.17), the maxima and minima of the interference pattern are delayed with respect to the ones of the refractive index changes (Fig. 4.17 (b)), and the index grating moves downward the fiber. This process is strongest, when the HOM content is 50%. When the energy in the HOM increases further, the waveguide changes become more adiabatic, and the transfer rate gets reduced.

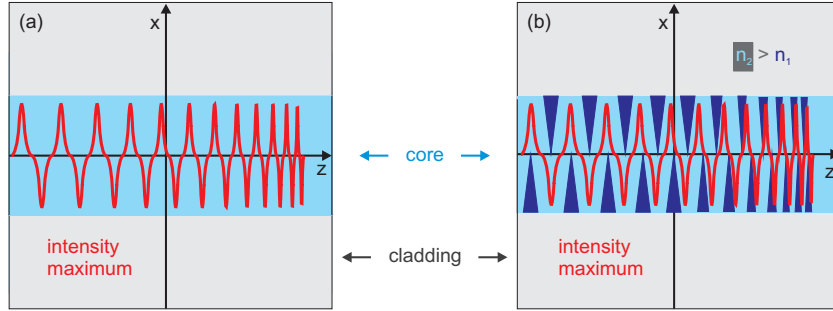


Figure 4.18: (a): As the individual propagation constants of the interfering modes experience a slightly different magnitude of the thermally-induced waveguide changes, the modal beating-period changes along the fiber axis z and the interference pattern gets compressed towards the fiber end. (b): The refractive index grating, corresponding to the resulting new heat load takes some time to be induced and is thus delayed with respect to the irradiance pattern. The figures representatively illustrate the case for a counter-pumped amplifier and are drawn according to Ref. [28].

A reversal of the gratings' movement direction, leading to energy transfer from the HOM to the fundamental mode, was related to the different impact of the thermally-induced waveguide changes on the individual modal propagation constants. Even though the two modes interfere, their propagation is determined by their individual propagation constants. The impact of the thermally-induced waveguide changes on these propagation constants differs in strength for the two modes. Therefore, the modal beating period changes, while the irradiance pattern propagates along the fiber. The modified interference pattern generates a new heat load, inducing a refractive index grating that is slightly phase-shifted with respect to the already induced one. While the interference pattern can change almost instantaneously, the thermal index induction requires some time. Hence, the interference pattern gets faster compressed than the thermally-induced index grating, which in turn moves upward the fiber. Fig. 4.18 illustrates this effect. Consequently, the created phase shift has the opposite sign compared to the process, enabling energy transfer from the FM to the HOM. The effect depends on the transverse local temperature gradient and its influence on the irradiance pattern weakens when the local period of the interference pattern approaches the period determined by the local waveguide changes. When the HOM content is reduced to 50%, the nonadiabatic waveguide changes become the dominant process again. In this manner, the oscillating modal content was explained.

In their numerical calculations, the intensity grating and the temperature profile were calculated along the fiber over 1 ms. At this point, the simulation was stopped due to the long computational time. Dramatic power conversion was not observed, but that usually takes place after a few milliseconds. Nevertheless, downward movement of both gratings, but at different speeds was revealed. This led to a relative phase shift, induced by the fact that the temperature grating started to move first, and was attributed to the nonadiabatic

waveguide changes described before. Studying the instantaneous position of both gratings' maxima further confirmed the downward movement. Furthermore, their model revealed the existence of the proposed process leading to energy transfer in the reversed direction. Plotting the period of modal beating along the fiber with time showed that the "natural" modal beating period (which the interference pattern would have, should it not have been affected by propagation) changes along the fiber with z . In fact, it gets smaller due to the transverse index gradient, resulting in a compressed interference pattern, moving upward the fiber. Thus, the feasibility of the proposed processes to enable a movement of the grating and this in turn yielding energy transfer, was demonstrated. Their work can at least be considered as analysis of possible processes at the start up of MI at a fixed power level.

Computational extensive calculations, supporting the idea of a static grating, together with a transient process to be the essential source for TMI, were carried out by B. Ward and the group of S. Naderi [183, 190, 191]. The model captured most of the observed amplifier characteristics without assuming a frequency offset in advance, just by considering transient heating. It is based on dynamic feedback between the optical intensity field and the temperature distribution. The modal amplitudes were calculated from coupled differential equations and then used to update the temperature distribution, resulting from the quantum defect heating induced heat load [183]. Consequently, the temperature-profile followed the population inversion and accounts for TSHB. This new heat load was then used to update the refractive index in the coupled mode equations.

Calculations of the time-resolved modal power distribution for the LP_{01} and the LP_{11} mode for different amplifier power levels revealed three oscillation regions [183, 190], similar to the ones observed in Ref. [181]. In the stable regime, the power oscillates almost fully between the two modes for a few milliseconds, before settling to a constant distribution with most of the power in the LP_{01} . The same initial transient effect is observed at the TMI threshold power level, but afterwards, the power keeps oscillating periodically between the two modes, denoting the transition regime. Corresponding frequencies were calculated to be in the kHz range. At even higher output powers, the modal power distribution started to oscillate chaotically and the corresponding frequency spectrum comprised of broadband noise, again in the kHz range. Additionally, a linear dependence of the TMI threshold power with seed power was found. However, the major weakness of this model is that it cannot unambiguously explain the harmonic oscillations, observed in some of the experiments. Calculations with the latest update of this model did not yield any periodic behavior, but chaotic modal content fluctuations just at the TMI threshold [191]. This indicates that a static grating in the presence of a transient is not the solely source for the experimentally observed TMI process.

Contrary to the groups of Jauregui et al. as well as Ward et al., Smith and Smith followed their idea of a frequency shift between the two interfering modes in advance to account for the necessary phase shift between the irradiance pattern and the grating [192]. A frequency shift, injected in advance, causes the grating to move along the fiber with a velocity proportional to the offset frequency, even if transient heating effects (i.e. time-

dependence of the heat equation) are neglected [193]. This mode-coupling mechanism yields a dispersion-like gain profile with zero-offset frequency. Hence, Smith and Smith categorized the process as a form of stimulated forward thermal Rayleigh scattering (STRS) [192]. Thermal equilibrium is a crucial condition for STRS to start [194]. For a thermally-induced index-grating, the dispersion curve peaks at a frequency of only a few kHz, which corresponds to the observed time-scale of TMI. Yet, the origin of the necessary frequency shift is a major question and currently still under discussion.

Sources for the frequency-shifted light were discussed to be quantum noise seeding, spontaneous thermal Rayleigh scattering, as well as pump- and seed-amplitude (or -phase) modulation. The latter two effects were calculated to easily reduce the TMI threshold power by 20 %, compared to quantum noise seeding [165]. A counter-modulation scheme, to e.g. compensate a pump-modulation with proper chosen signal modulation parameters, could re-enhance the power threshold, but not fully restore it, compared to solely quantum-noise seeding [195]. At least one of these modulations is believed to be present in most laboratory amplifiers, as the pump- and seed-sources can be quite noisy. Furthermore, linear absorption processes such as photodarkening were also found to lead to a significant threshold power reduction [195]. TMI mitigation, on the other hand, was obtained by increasing the mode specific loss for the HOMs [195]. The threshold-like onset of TMI was traced back to the high necessary mode coupling gain [192].

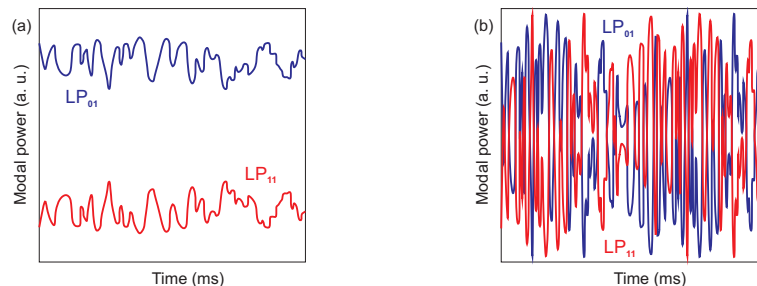


Figure 4.19: Modal power oscillations for RIN seeding, as calculated by Hansen et al. and presented in Ref. [29], (a): at a power level just above the TMI threshold and (b): well beyond it.

As the models by Ward et al. as well as Smith and Smith involved heavy computations and long run-times, Hansen et al. developed a semi-analytical approach to model qualitative features of TMI [187]. It is based on deriving and evaluating a coefficient for the coupling strength between the modes and basically supports the theoretical attempt by Smith and Smith. Nevertheless, Hansen et al. numerically extended their analytic approach to evaluate the temporal and spectral features of TMI in detail, yielding very interesting results. In particular, the absence and appearance of the harmonic modal power transfer can be explained with the analysis from Ref. [29]. At the TMI threshold, instantaneous modal power transfer was observed, even though the HOM was not artificially seeded [29].

Only quantum noise or additional relative intensity noise (RIN) was added as phase noise to the fundamental mode. Frequency resolved amplifier output was not calculated in this case, thus it is difficult to compare the result to the experimentally observed regimes. Nevertheless, as schematically shown in Fig. 4.19 (a), only part of the power was transferred back and forth in a rather chaotic manner. Nevertheless, the time-scale (milliseconds) resembled the reported experimental results. Calculation of the HOM spectrum revealed a Stokes-shift, corresponding to the peak frequency of the mode coupling gain profile. Increasing the laser gain to simulate an increased pump power yielded roughly the same behavior. In this case, however, the chaotic modal amplitude oscillations were comparably faster and implied full power transfer between the interfering modes (Fig. 4.19 (b)).

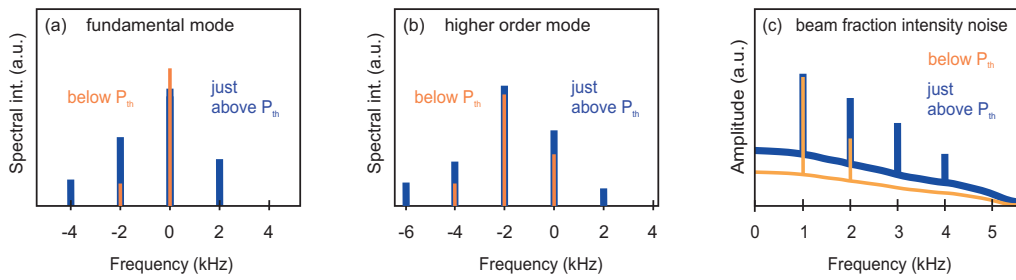


Figure 4.20: Spectrum of the (a): fundamental mode and (b): higher order mode, below and just above the TMI threshold for an amplitude modulated seed signal. (c): Interference of modes with these spectra yields distinct peaks in the frequency resolved amplifier output intensity, sampled at one point in the transverse beam profile. The figures are drawn according to the results presented in Ref. [29].

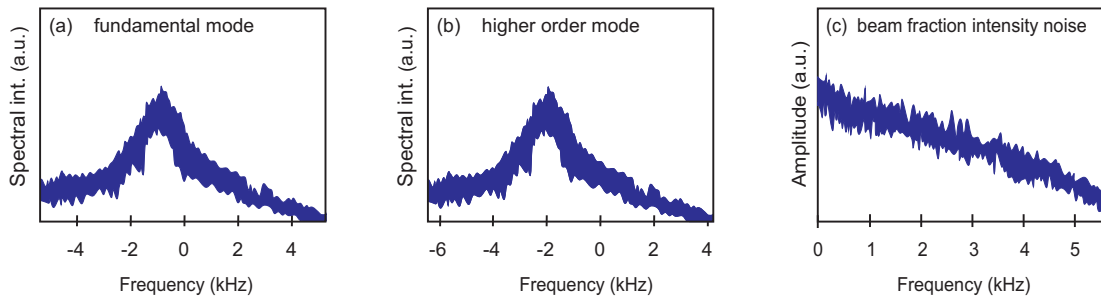


Figure 4.21: Spectrum of the (a): fundamental mode and (b): higher order mode, well above the TMI threshold for an amplitude modulated seed signal. (c): Interference of modes with these spectra yields broadband frequency resolved intensity noise at a small fraction in the transverse beam profile. The figures are drawn according to the results presented in Ref. [29].

Different results for the modal spectra and the frequency resolved amplifier output intensity were observed for an amplitude modulated seed signal. More and more side bands appeared due to four-wave mixing (FWM) with increasing laser gain in both spectra, while

the LP_{11} mode was again red-shifted with respect to the LP_{01} (Fig. 4.20 (a)). Interference of the two modes yielded harmonic peaks in the amplifier output intensity, if a small fraction of the transverse beam profile was sampled (Fig. 4.20 (b)). These Fourier-spectra of the fractional beam intensity resembled the measurements from References [181] and [183] qualitatively well. The additional Stokes bands were found to act as seed for nonlinear power transfer between the modes and the cascading process was said to continue until eventually the threshold power for RIN or quantum noise induced TMI is reached. In fact, the numerical evaluation in Ref. [29] revealed broad noisy modal spectra well above the threshold power, masking out the discrete frequency peaks (Fig. 4.21 (a) and (b)) [29]. Consequently, the resulting fractional transverse beam intensity spectrum consisted of broadband noise (Fig. 4.21 (c)), just as experimentally observed for the chaotic oscillation regime.

The semi-analytic approach from Ref. [171] was taken on by the group of Hu et al. [196]. In fact, they referred to Ref. [171] for the derivation of the steady-state solutions to the coupled mode equations. Their own publication focused on the derivation of analytic coupled-equations for spatially and temporarily varying modal amplitudes. The most interesting result of this work, which distinguishes it from other publications, arises from a variation of the modal offset frequency. Setting the latter to the peak frequency $\Delta\omega_{\text{peak}}$ of the STRS gain spectrum yielded harmonic oscillations, even at the highest pump power level presented (1500 W in this case). At the same power level, a frequency separation of $-\Delta\omega_{\text{peak}}$ led to rather chaotic behavior and periodic peaks were only present up to 1000 W of pump power. Detuning the frequency offset from $\pm \Delta\omega_{\text{peak}}$ yielded harmonics only up to about 500 W of pumping. Moreover, the separation of the frequency peaks was decreased. Interestingly, Hu et al. did not inject any sidebands when observing the harmonics, contrary to the works of Smith and Smith [197] as well as Hansen et al. [187].

Another theoretical work, based on steady-periodic heating and yielding zero mode coupling gain for a non-zero frequency offset between the interfering modes was published by L. Dong [194]. In this case, the method to solve the heat equation differs from all the other models. L. Dong sums over all spatial temperature modes to obtain the traveling temperature wave, driven by the moving interference pattern. Heat diffusion, which dominates in the radial direction, damps the traveling temperature wave [194]. Influences of several fiber parameters on the threshold powers were basically the same as in Ref. [187]. In fact, L. Dong explicitly compared his calculated threshold powers to the values stated in [187] and found agreement within 3% [194]. Thus, solving the heat equation with temperature modes is just as adequate as utilizing Green's functions. According to this model, increasing the threshold power, can only be achieved by reducing the overall gain or the ratio of the input powers $\frac{P_{11}}{P_{01}}$ and is independent of all other amplifier parameters [194]. This is, however, not surprising, as rate equations to model the laser process were not included.

4.3.2 TMI characterization methods

Even though a lot of experimental and numerical work has been put into investigating the characteristics and origin of TMI, the scientific community is just about to begin to understand the effect. Still, a major question is, whether a transient effect that induces a Doppler-shift between the interfering modes predominantly triggers TMI or if a frequency-offset between the interfering modes is required for TMI to start. Both theoretical attempts (“philosophies”) have proven to explain some of the observed experimental features, indicating that both processes might be present. Additionally, TMI seems to be very sensitive to several system parameters and the overall amplifier configuration, aggravating it to capture all of the effect’s attributes in one numerical model. Furthermore, only four different research groups have published experimental works so far, and at least three of them have developed their own models of TMI. Consequently, their experimental research often seems to focus on proving the relevance of their model and that it captures the most crucial features of TMI.

For the work of this thesis it was thus interesting to experimentally investigate different characterization methods for the TMI threshold and dynamics. As the threshold power seems to be independent of the signal bandwidth for a linewidth larger than 1 kHz [183], a low-noise seed laser could be utilized, and the modal decomposition of the fiber output beam by utilizing the DBB (Section 4.1) was possible. This measurement technique could reveal even a slight potential beam quality degradation below the visible threshold, which had not been investigated before. Additionally, the possibility of using the DBB to get an insight into the TMI dynamics was tested. A power transfer between fiber modes should be visible by comparing mode scans at different power levels, as a change in the modal output of the fiber with respect to the fiber modes also changes the modal decomposition with respect to the TEM_{mn} modes.

By the time the experiments presented here were started, the works containing experimental results regarding the three oscillation regimes were not yet published. It had only been demonstrated that full modal power transfer can take place on a millisecond timescale and that the participating frequencies decrease with increasing core diameter [198]. Moreover, these frequencies were obtained by measuring and Fourier-transforming the time traces of the modal power evolution. Thus, it was interesting to directly measure the frequency resolved intensity noise spectra and study their evolution below and above the visible beam degradation threshold. This allowed for an examination of potential amplifier output power fluctuations beyond the modal instability threshold in the kHz frequency range. Secondly, in the case of a stable overall output power, the utilization of an aperture should yield a measurable conversion of the effect to intensity noise.

The single-frequency amplifier setup for these experiments consisted of a 9 W seed signal (linewidth about 1 kHz at 1064 nm) and an Yb-doped PM PCF (DC-400-38-PZ-Yb by NKT photonics), pumped by a low-brightness diode module in a counter-propagation scheme. The PCF parameters can be found in Table 4.2. Calculation of the effective V-number of this PCF according to Eq. 2.33 yields $V_{\text{eff}} = 2.569$. Thus this fiber can guide

Table 4.2: Parameters of the Yb-doped PCF.

core \varnothing , NA	38 μm , 0.03
MFD, \varnothing doped region	29 μm , 30.5 μm
inner, outer clad. \varnothing	400 μm , 600 μm
nominal absorption	2.4 dB/m at 976 nm
coating	high-temperature acrylate
pitch Λ	10 μm
rel. hole size $\frac{d}{\Lambda}$	0.19

at least one HOM, even though effective single-mode operation is supposed to be easily obtained as the doped area was smaller than the core, and through additional external coiling [199]. To reduce the coupling of the pump power noise to the output power, only 1.45 m of this PCF were used [200]. It was wrapped half way around an aluminum spool with a diameter of 40 cm. The pump-end of the fiber was held in a water-cooled chuck.

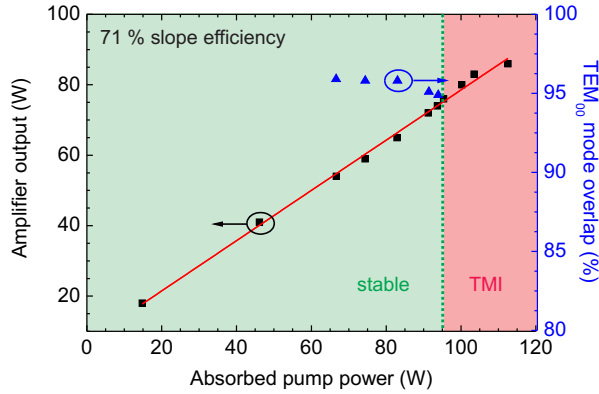


Figure 4.22: Signal output power and corresponding measured TEM_{00} mode content versus absorbed pump power for the amplifier set up to investigate TMI. The absorbed pump power was calculated assuming a pump coupling efficiency of 83 %.

In Fig. 4.22 the amplifier output power is plotted with respect to the absorbed pump power. Assuming a pump coupling efficiency of 83 %, the slope efficiency was 71 %. Amplifier operation regimes corresponding to stable modal content and TMI are denoted by the differently colored background. The visible threshold for the mode instabilities was sensitive to the seed alignment, but with optimized mode-matching it varied only by about 2 % between 95 W and 98 W of absorbed pump power, corresponding to 74 W and 76 W of signal output. At this threshold power, the beam profile started to fluctuate visibly, indicating an energy transfer between the fundamental LP_{01} and an LP_{11} mode [181]. The beam images shown in Fig. 4.12 (a) to (d), Section 4.3.1, were measured from this amplifier

at the threshold power (76 W of signal power in this case, as marked in Fig. 4.22), with a frame rate of 10 Hz.

The beam quality and its potential degradation due to modal power transfer below this visible threshold was analyzed with the DBB. As the scanning ring cavity requires the input beam to be linearly polarized, the PER of the amplifier output beam was measured before each mode scan. While the amplifier output power was increased from 18 W to 74 W, corresponding to an absorbed pump power of 15 W and 94 W respectively, the PER increased slightly from 18 dB to 20 dB. This can be explained by a higher relative amount of residual power in the cladding at lower pump power levels. For the measurement of the fractional TEM₀₀ mode content, the seed coupling was once optimized at a signal power of 54 W. At this power level, the average overlap of the beam with the TEM₀₀ mode was 95.9%. Increasing the signal power to 74 W led only to a slight decrease in the TEM₀₀ mode content to 94.9%. This could be due to mechanical pointing, potentially caused by a slight thermal misalignment of the seed coupling at higher pump power levels, as the seed coupling was not further optimized to exclude artificial alignment effects.

Further increase of the signal power to 76 W led to the onset of visible beam profile fluctuations. The PER was measured to be still about 20 dB, but the modal composition of the fiber output beam changed on a millisecond timescale, and the alignment into the scanning cavity could not be optimized. Altogether, the modal decomposition per FSR (free spectral range) scan varied strongly, yielding higher order mode (HOM) contents between 8.7% and 18.6%. At 80 W of signal power already 28.8% (averaged over 9 FSR scans with 1 Hz scanning rate and a variance of 12.2%) of the power was distributed into higher order cavity modes. The dominant HOMs in the obtained scan were e.g. TEM₀₁, TEM₁₀, TEM₁₁ and TEM₄₀, but no real information regarding the TMI process can be obtained by this observation. However, observing the cavity transmission signal (transmitted power versus frequency) on an oscilloscope revealed that their power distribution was chaotically changing within milliseconds. Hence, this measurement technique needs further customization to characterize the beam profile fluctuations beyond the instability threshold, but the sudden beam quality degradation is clearly visible even in this configuration.

The setup utilized to measure the frequency resolved intensity noise spectra is depicted in Fig. 4.23. The first CCD camera was used to record beam profile videos without the aperture. With the second CCD camera the beam profile at the aperture, which was used to convert beam profile fluctuations into intensity fluctuations on the photodiode, was imaged.

The measurement procedure consisted of two steps. First, the intensity noise spectra were recorded without the aperture. No significant increase of the amplifier noise, measured up to 100 kHz, (Fig. 4.24 (a)) was observed after the beam profile started to show some pointing or, at even higher pump power levels, to visibly fluctuate. I.e., the overall output power was stable despite of the beam profile fluctuations. In the second step, the aperture was partially closed and the intensity noise spectra were again measured with increasing pump power. Throughout the measurement, the aperture width remained constant as the aperture size affects the visibility of the mode instabilities [181] and once adjusted, the

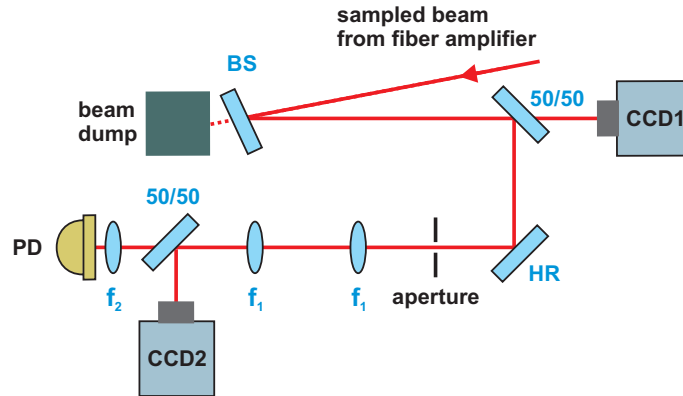


Figure 4.23: Experimental setup for the measurement of the frequency resolved intensity noise spectra. BS: beam sampler and HR: highly reflective mirror. PD: photo diode. $f_1 = 100$ mm, $f_2 = 15$ mm.

seed as well as the pump coupling were not realigned.

The relative intensity noise (RIN) spectra for different levels of absorbed pump power are shown in Fig. 4.24. Different fluctuation regimes could be identified, similar to the ones in References [181] and [183]. Up to a signal power of 74 W the beam profile showed some modal power fluctuations for a few seconds just after the pump power was increased, before settling to a stable high fractional fundamental mode content. Only at the power level, where modal power transfer was permanently visible in the optical intensity profile, (76 W in this case), a sudden rise in the low frequency range up to about 1.4 kHz was observed in the RIN.

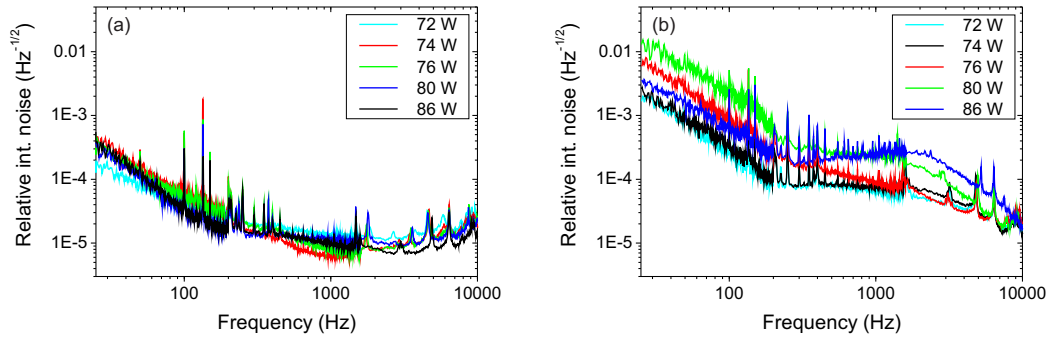


Figure 4.24: Relative intensity noise spectra at different levels of signal output power (a): without and (b): with an aperture in the sampled beam, to convert the modal power fluctuations into intensity fluctuations on the photodiode.

At higher signal power levels, the RIN also started to rise at higher frequencies (80 W) and eventually the low frequency fluctuations decreased again (83 W). At this power level,

the beam profile visible on the CCD cameras rather resembled an LP_{11} mode most of the time due to incoherent addition of the two modes. The upper limit of contributing frequencies increased to about 2.5 kHz, with a tail extending to about 8 kHz. Increasing the signal power to about 86 W did not lead to further significant changes in the shape of RIN spectra. Repeated measurements on the same amplifier reconfirmed their evolution. Even though the threshold power itself was sensitive to the amplifier alignment and could vary by a few percent, the shape of the RIN spectra in general were the same.

Using an amplifier configuration very similar to the previous experiments, the influence of seed- and pump-modulation on TMI was investigated. The same piece of PCF was utilized as amplifier fiber, but the ends had to be re-polished and the fiber length was now only 1 m. Also the setup for the diagnostics remained the same as presented in Fig. 4.23. The threshold power for the visible onset of TMI without external amplitude modulation was around 64 W of amplifier output, thus about 10 W lower than for the ~ 0.4 m longer fiber.

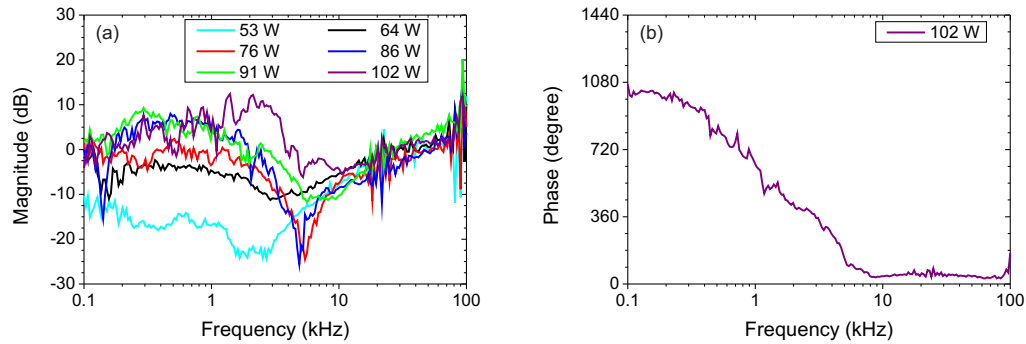


Figure 4.25: (a): Measured transfer functions for seed amplitude modulation of 0.6% at different amplifier output power levels. An increase in the modulation magnitude with increasing signal power can clearly be seen from about 0.1 kHz to 10 kHz. (b): Phase shift at different seed amplitude modulation frequencies for 102 W of amplifier output power. The fact that the phase does not change randomly with the modulation frequency indicates that the increased modulation magnitude in (a) is not due to an overall increase in amplifier noise, but rather indicates that the seed amplitude modulation gets amplified by the TMI process.

Modulation of the seed signal was carried out by sinusoidally modulating the pump-current for the preamplification stage. To get a first impression of a potential TMI threshold power dependence on the modulation frequency, the amplifier output was monitored with a CCD camera, while the modulation frequency was changed between 100 Hz and 10 kHz. Even though for frequencies between 1 kHz and 2 kHz the threshold seemed to decrease by a few Watts, this observation was not clear-cut and reproducible. Thus, a part of the beam profile was sampled with an aperture and detected with a photodiode. Transfer functions were recorded from 0.1 kHz to 100 kHz modulation frequency. The results for an amplitude modulation of 0.6% are depicted in Fig. 4.25 (a). An increase in the modulation magnitude with increasing signal power can clearly be anticipated. Distinct frequencies do, however,

not appear. Moreover, no definite dependence of the transfer function evolution with signal power can be identified and it seems rather chaotic. Nevertheless, the evolution of the phase with frequency indicates that the increased modulation magnitude in Fig. 4.25 (a) is caused by amplification of the seed-modulation by the TMI process. Noise due to the amplification process, artificial noise due to slight mechanical beam pointing at the aperture as well as overall TMI induced noise would rather yield a randomly changing phase. As an example, the phase measured at an output power of 102 W, is depicted in Fig. 4.25 (b). It basically looked alike at other power levels. Neither did a change in the modulation depth yield any significant changes in the measured amplifier performance.

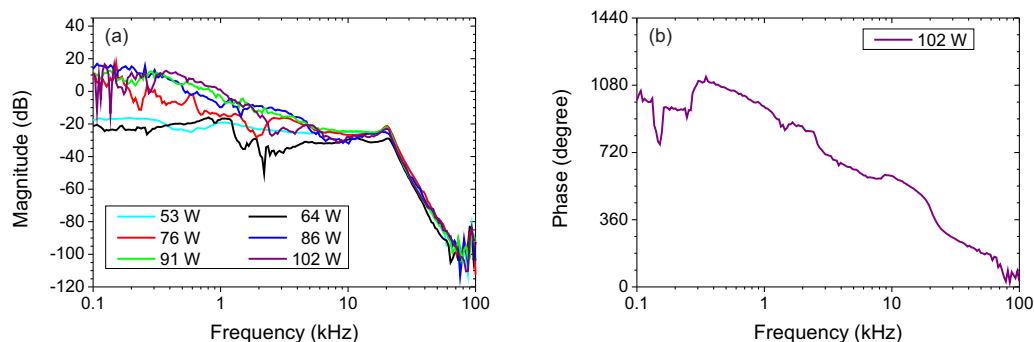


Figure 4.26: (a): Measured transfer functions for pump amplitude modulation of 0.2% at different amplifier output power levels. An increase in the modulation magnitude with increasing signal power can clearly be seen from about 0.1 kHz to 10 kHz. (b): Phase shift at different pump amplitude modulation frequencies for 102 W of amplifier output power. The fact that the phase does not change randomly with the modulation frequency indicates that the increased modulation magnitude in (a) is not due to an overall increase in amplifier noise, but rather indicates that the seed amplitude modulation gets amplified by the TMI process.

The same behavior of the amplifier was observed, when the pump-signal of the PCF was amplitude modulated. This time, the sinusoidal modulation was applied to the current of the high-power laserdiode. Exemplary transfer functions and the corresponding phase at an amplifier output power level of 101.7 W are presented in Fig. 4.26 (a) and (b), respectively. The pump modulation amplitude in this case was 0.2%.

4.3.3 Comparison to other experimental and numerical works

The first interesting observation in the experiments from Section 4.3.2 is the transient behavior, i.e. the initial visible beam profile fluctuations below the actual threshold power level for permanent TMI. This can not be explained by the proposed STRS mechanism, which can only start from thermal equilibrium [27, 187, 194, 196], but by the static grating theory [28, 190, 191, 201]. Without any external perturbations, there would be no phase-shift between the irradiance pattern and the index grating [188, 190]. Increasing the pump power can perturb the steady-state, as the optical phase changes much faster

than the temperature phase [183]. Once thermal equilibrium is reached, the process vanishes and the modal content becomes stable, just as verified by the DBB and RIN measurements. Contrary to the numerical results presented in the literature, where modal power evolution was only studied for a maximum of 100 ms [191] (due to the computational effort), the initial transient in the experiments for this thesis subsided only after a few 10 s. Nevertheless, this is most likely caused by the several potential sources for external perturbations, e.g. mechanical, cooling arrangement, and – as will be discussed later on in detail – intensity noise. If the computational time could be sped up and more external perturbation sources included, the result would probably rather be a longer transient time than the vanishing of it.

Still, the described observations strongly indicate the presence of a static grating below the TMI threshold. Moreover, there was no sign for STRS induced mode coupling, i.e. permanent modal power transfer once thermal equilibrium is reached. Consequently, it implies that the heat load at power levels below the visible onset of TMI was high enough to induce a static refractive index grating, but not sufficient for STRS induced mode-coupling to start. Of course, this can not be interpreted as a general characteristic of the TMI process, which has proven itself to be very sensitive to all system parameters. Nevertheless, such transient behavior was even suspected to exist by some researchers, primarily concerned with a steady-state analysis of a frequency-shift induced moving grating [187, 193, 194]. At least for the given setup, it seems to be the most likely situation.

Another feature observed in the TMI-experiments for this thesis is the extremely low threshold power for a fiber with a core diameter of about 38 μm . For 10 m of a similar PCF, the threshold power level was measured to be beyond 500 W [202]. Even though the threshold power is sensitive to almost all the system parameters, which makes comparison of different setups very difficult, and decreases for shorter fibers [25, 176], it is surprising, as for slightly shorter (1.2 m) rod-like fibers with core diameters larger than 50 μm , measured threshold powers were at least 100 W of signal output [170]. Apparently, the fiber utilized in the experiments from Section 4.3.2 was fully degraded. This conclusion is supported by a reproducible threshold power level. A pristine fiber, on the other hand, experiences strong threshold power reduction, every time the pump power is increased from zero [178, 201]. Additionally, the fiber might inhibit some defect, causing linear absorption, which can according to the simulations by Smith and Smith [195] also lower the threshold power. These assumptions are supported by the fact that the amplifier slope efficiency of 71 % (Fig. 4.22) was comparably low for a Yb-doped fiber amplifier. A similar PCF yielded much higher values (Section 5.1).

Slightly changing the seed-coupling to the amplifier from Section 4.3.2 confirmed that the fundamental mode excitation was optimized. The TMI threshold could not be further increased by changing the alignment. Eventually, it only led to even lower threshold powers, indicating a sensitivity to the ratio of initial powers in the LP_{01} and higher order mode. Such a dependence was also reported by Jauregui et al. [176], and captured by the steady-state models [187, 194], while Naderi et al. explicitly reported insensitivity of the

threshold powers, calculated with their transient model, to this parameter [190].

Contrary to reports in References [181] and [201], where the onset of TMI was characterized by an exponential increase in the first derivative of the standard deviation of the power evolution with time at a small fraction of the beam profile, the amplifier system from Section 4.3.2 exhibited a rather step-like TMI threshold. Especially, the DBB measurements confirmed excellent beam quality without any significant increase in HOM content below the power level, where beam profile fluctuations became visible on the CCD camera and the RIN started to increase (76 W of signal output). The reported TEM₀₀ mode content at an amplifier output of 74 W was calculated from 50 scans with a standard deviation of only 0.3%, indicating that the reported stable modal content was not due to measurement inaccuracy. Moreover, the group of Jørgensen et al. utilized the same threshold evaluation method as References [181] and [201] and also found a rather step-like onset of TMI. Thus, the characteristic of the onset (step-like or exponential) seems to depend on the exact system conditions. In general, the nonlinear threshold (instead of a gradually decreasing beam quality) is attributed to the necessary heat load to induce a refractive index grating of sufficient oscillation depth. The transient model needs the external perturbations to be strong enough to permanently disturb thermal equilibrium and the STRS model requires a sufficiently strong mode-coupling gain.

Beyond the threshold-power, TMI characterization with the DBB was not further possible due to the TEM_{*nm*} modal content fluctuations on a ms-timescale. These fluctuations could on one hand be caused by relative phase changes between modes of constant powers. Likewise, they could be due to modal power transfer, but this can not be distinguished with the DBB. Nevertheless, the timescale is consistent with all other publications related to experimental investigations of TMI. This ms-timescale is agreed upon to be a strong indicator for the thermal origin of the effect, but detailed explanations have not been found so far. Smith and Smith [203] as well as the group of Otto and Jauregui et al. [181] compared it to the overall thermal diffusion time in the transverse direction and found agreement, at least in the order of magnitude for the corresponding frequencies. The overall values differed slightly, which was basically attributed to the TMI sensitivity to the system parameters. Naturally, modal content fluctuations can only be captured by time-dependent models, but have been observed in numerical evaluations, independently of assuming a frequency-offset between the modes a priori or not.

The most interesting aspect of the modal content fluctuations is under which conditions periodic (harmonic) behavior or chaotic oscillations were observed. While some publications emphasize the appearance of a broad transition regime (in terms of power levels) with periodic oscillations in their experiments [181, 183, 201], straight onset of chaotic oscillations at the TMI threshold has also been observed (Section 4.3.2 and Ref. [178]). The group of Jauregui and Otto et al. related the distinct periodic frequencies to different sections of the grating, moving at different speeds and partly into opposite directions as well as some other (not further specified) external perturbation parameters [181]. However, numerical modeling without injection of noise or an amplitude modulation can apparently not capture this TMI feature.

In fact, the best explanations for the appearance of a periodic transient regime in some experiments and its absence in others (just like in the work for this thesis), can be found in a STRS based theoretical work by Hansen et al. [29]. They found a transition regime with harmonic behavior only for an amplitude modulated seed. Due to FWM, more and more frequency peaks appear in the modal spectra besides the carrier and initial sidebands. Consequently, an increasing number of harmonics appears in the intensity-spectrum at some fixed transverse location within the amplifier output beam. Eventually, the modal spectra become noisy at a certain power level and the discrete frequencies get masked out. As a result, the harmonics also disappear in the Fourier-spectrum of the modal power oscillations, which is then characterized by broadband noise. Ref. [29] found this to be the case, right at the TMI threshold, if no amplitude modulation was imposed on the seed signal and only RIN or quantum noise was injected to seed the STRS process. Oscillation depth and frequency increased with increasing amplifier power, resembling another feature of Fig. 4.24.

Interestingly, in Ref. [196] Hu et al. found that only modulating the signal with the peak-frequency of the STRS gain profile produces harmonic modal power oscillations. Detuning the modulation frequency by about 10 % already produced chaotic oscillatory behavior. A physical explanation was not given, but maybe this is due to some kind of beating-effect, causing a detuned amplitude modulation to act as intensity noise seed. Nevertheless, the appearance of higher and higher oscillation frequencies with increasing amplifier power, as shown in Fig. 4.24, is reproduced by their model. Given these numerical results, the absence of the transition region in the experiments from Section 4.3.2 can be interpreted as indicator either for the absence of a sufficiently strong or for a detuned amplitude modulation of the pump and seed.

An additional amplitude modulation can potentially further decrease the TMI threshold, which seemed to be the case in the setups utilized for the works of References [181, 201] and in some cases [178], as suggested in Ref. [197]. Nevertheless, there is an ultimate lower-power limit for TMI, given by the necessary amount of heat to induce a refractive index grating of sufficient oscillation depth. As discussed at the beginning of this Section, the threshold power level of the amplifier characterized during the TMI investigations for this thesis inhibited already a very low threshold due to noise-seeding and degradation. Apparently, the attempts to further seed the STRS process with an additional amplitude modulation failed, as at lower amplifier power levels the heat load was not sufficient to provide the necessary mode-coupling gain, i.e. an additional moving grating. These proposed differences between the TMI triggering might also explain, why different amplifier systems exhibit either an exponential or a step-like TMI onset.

The chaotic oscillatory behavior has been observed in numerical calculations based on both “philosophies”, STRS as well as the transient assumption. Also the appearance of more and more higher frequencies in the RIN with increasing amplifier output power (Fig. 4.24) was captured by either model. Thus it is very difficult to conclude what actually caused the onset of TMI in the amplifier of Section 4.3.2. Without sufficient RIN seeding, the static grating might have always reached thermal equilibrium with the interference

pattern. It is also possible that at a certain power level and corresponding grating strength, the slightest external perturbation (which is, of course, also some kind of noise, but does not require a frequency-shift between the modes a priori) impedes the thermal equilibrium. Most likely, both processes are present and the relative strength strongly depends on the system parameters [176, 201].

The last feature from the experimental TMI investigations within the framework of this thesis that deserves some attention is the predominant appearance of the LP_{11} -like mode on the low-speed CCD camera. Naturally, this could simply be interpreted as a measurement artifact, caused by the low frame rate of 10 Hz. However, in Ref. [183], the simulations for a convectively-cooled amplifier showed exactly this behavior at power levels well above the TMI threshold. Assuming that the observation is not an artifact (due to incoherent addition of the modal intensities), this would indicate a reduced rate of power transfer from the LP_{11} to the LP_{01} . The STRS as well as the transient-process picture would attribute this to a reduced rate of phase-shift reversal between grating and irradiance pattern. Following the phenomenological description from Ref. [28] for the transient-theory, nonadiabatic waveguide changes would have been the dominant process at this power level. Grating period compression, induced by the different amount of thermal change, experienced by the individual propagation constants of the two modes, would have contributed less to the modal power content. In the STRS picture, a predominant LP_{11} mode is obtained by neglecting any time dependence, which would yield exponential gain along the fiber for the LP_{11} mode only. Physically this would mean a reduced influence of noise-seeding, i.e. a higher heat load induces a stronger grating, which in turn needs lower starting power in the frequency-shifted LP_{11} mode. This can also be anticipated by the fact that quantum noise seeding was demonstrated to be sufficient, but yielded highly overestimated threshold power levels for all the models.

4.3.4 Conclusion

The experimental investigations on TMI, carried out during the work for this thesis contribute largely to an improved understanding of the process characteristics and their origin. Indicators for TMI triggered by a static grating in the presence of a transient as well as for a noise induced moving grating have been identified. Consequently, it is very likely that there are several contributors to TMI in laboratory amplifier setups, which can not be captured by just one numerical model so far, due to the immense computational complexity.

One of the key observations described in Section 4.3.2 is the transient behavior below the TMI threshold. Even though it is very likely that this has been observed by other researchers it has not been emphasized in publications. Nevertheless, it strongly indicates the presence of a static grating that yields modal power transfer until thermal equilibrium is reached, at power levels where no signs of STRS induced TMI can be found. The latter actually requires a thermal equilibrium state.

As the characteristic broadband noise well beyond the threshold power has been captured

by models based on both “philosophies”, it is difficult to attribute TMI at these power levels to just one origin. Considering the experimental setup, the presence of a sufficiently high RIN-level in the seed as well as the presence of mechanical and thermal external perturbations to permanently trigger transient TMI are both very likely. Sources for the RIN would be e.g. the pump diodes of the preamplification stage and slight temporal variations of its PER. The latter would be converted into RIN behind the Faraday-isolators, placed between the two amplifiers. Mechanical and thermal vibrations, either at the seed or pump end could also increase the RIN. Furthermore, the disturbances at the seed end affect the ratio of the initial modal powers, potentially permanently impeding an equilibrium state between grating and irradiance pattern. Also the potential appearance of a predominant LP_{11} mode can be explained by both theories. In the STRS model it would be caused by a reduced influence of noise-seeding (which is responsible for the time-dependent modal power oscillations in the STRS model), while in the transient picture, nonadiabatic waveguide changes would have a much stronger impact on the phase-shift between grating and irradiance pattern than thermal changes of the individual propagation constants. An increasing upper frequency limit with higher amplifier power, on the other hand, has only been presented for STRS based models.

The second key result of the presented experiments is the absence of the periodic transition region, characterized by harmonic modal power oscillations. In the literature this has been considered to be a general characteristic of TMI, but it should be rather recalled as characteristic of TMI in particular amplifier configurations. In fact, recently the experimental results presented in this thesis were cited to justify the need for transient modeling of TMI. It was stated that TMI is often characterized by broadband noise and less significance was attributed to the harmonic transition region [191]. While the appearance of the periodic oscillations in some static-grating models is ambiguous and under discussion, it can be explained by amplitude modulation of pump- and/or seed-signal in the STRS models. Such an amplitude modulation might also lead to a lowered threshold power, compared to noise seeding or transient triggering of TMI. Nevertheless, there must be an ultimate lower power threshold due to the necessary heat load for refractive index changes and a sufficiently strong mode coupling. The experimental work for this thesis has demonstrated that the TMI threshold of an amplifier system deploying a fully degraded fiber (that might even incorporate sources for additional linear absorption) can not be further lowered by additional amplitude modulation of seed- and/or pump-signal.

5 Fundamental mode content of single-frequency ytterbium-doped fiber amplifiers

The future generation of GWDs operating at 1064 nm wavelength demands around 1 kW of linearly-polarized single-frequency output from the laser source [6, 12]. Amplifying a signal with a linewidth of only about 1 kHz to the desired power levels with excellent beam quality is still a challenge. Defining this excellent beam quality by a high overlap with the free-space TEM_{00} mode represents a further restriction on the deployable fibers as well as the amplifier configuration. For beams transmitted through passive versions of fiber design concept candidates, the TEM_{00} mode overlap has been analyzed in the previous Chapter. Moreover, all potential issues arising from power scaling with their active counter-parts were described in general. In this Chapter, actual measurements regarding the TEM_{00} mode power extraction from these active LMA fibers are presented. The focus of the experiments was thereby set on the advanced fiber technologies, photonic crystal fibers and chirally coupled core fibers. They are the most promising candidates to reach the power levels for the next generation of 1064 nm based GWDs [20, 21, 74, 184]. The future application of standard step-index fibers in high power CW SF laser systems will most likely be all-fiber integration at power levels of 200 W to 300 W [18, 204], as their core diameters with reasonable modal performance are limited to 25 μm .

Section 5.1 starts with the analysis of the photonic crystal fiber design concept in terms of the largest core diameter available for a bendable fiber, which is 40 μm . For the CCC fiber design concept, fibers with 37 μm and 55 μm core diameter sizes were deployed. The results are discussed in Section 5.2. To the performance of all utilized fibers, the same questions were addressed. For low and for high power levels it was likewise interesting to see whether HOMs could be excited or if FM operation was easy to achieve. Most important was the measurement of the TEM_{00} mode overlap of the amplified output beam, and the investigation of the nature of the TEM_{00} modal power scaling limit. Potential limits were SBS, thermal issues, parasitic lasing processes and TMI.

Focusing on a high fractional TEM_{00} mode power extraction distinguishes the amplifier experiments carried out within the framework of this thesis from other works in the field of power scaling of CW SF signals at 1064 nm. Nevertheless, the investigations presented here do not only contribute to the development of laser systems for future GWDs. They can also be considered as general progress in understanding the modal performance and properties of advanced fiber design concepts.

5.1 PM LMA photonic crystal fiber amplifier

5.1.1 Fiber geometry

Even if coherent beam combination is considered, to reach the power level for potential GWD application, it is highly desirable to extract as much TEM_{00} mode power from a single-amplifier chain as possible. Naturally, the performance of the largest available core size for a bendable PCF was investigated in the following experiments. Nominal fiber core diameter and NA were $40\ \mu\text{m}$ and 0.03, respectively. To reduce the effect of TSHB (Section 4.3), the diameter of the doped region was only $30.5\ \mu\text{m}$, adjusted to the MFD of the fundamental fiber core mode. This was specified to be $29\ \mu\text{m}$ at $1060\ \text{nm}$. According to the manufacturer, NKT photonics, the fiber core operated transversely single-mode at this wavelength. Their standard product with these core parameters, the fiber DC-200-40-PZ-Yb, comes with a cladding diameter of $200\ \mu\text{m}$. This cladding size results in a nominal absorption of $10\ \text{dB/m}$ at $976\ \text{nm}$, hence to reach several $100\ \text{W}$ of output power, the heat load would have been considerably high. Furthermore, at the beginning of the work for this thesis, pump diode modules with sufficient optical output power were of rather low brightness and only available with delivery fibers of at least $400\ \mu\text{m}$ ($0.22\ \text{NA}$). Thus, a modified version of the fiber with a $400\ \mu\text{m}$ pump cladding diameter ($0.6\ \text{NA}$) was chosen. It was from the first spools drawn of this customized geometry, which resulted in some issues, as will be explained later in this Section.

With the $400\ \mu\text{m}$ pump cladding diameter, the nominal absorption at $976\ \text{nm}$ was $2.4\ \text{dB/m}$. The fiber had an air-clad and an outer silica glass cladding with a diameter of $700\ \mu\text{m}$. It was finally coated with a high temperature acrylate. Two boron stress-rods induced high birefringence to ensure linear polarization at the fiber output, if the signal was launched in the slow fiber axis.

5.1.2 Experimental setup

A fiber length of $6.8\ \text{m}$ was used in the experiments. It was partly coiled on a $40\ \text{cm}$ diameter metal spool, but not actively cooled. Only the pump end of the fiber was placed in a water-cooled copper v-groove. The fiber ends were angle-polished, after the air-holes had been collapsed to seal the end facets.

The amplifier setup is depicted in Fig. 5.1. A nonplanar ring oscillator (NPRO) delivered the low-noise $\sim 1\ \text{kHz}$ linewidth seed signal with an output power of $500\ \text{mW}$ at $1064\ \text{nm}$. This is quite low compared to the targeted PCF amplifier output power of several $100\ \text{W}$, and the resulting high gain of more than $20\ \text{dB}$ can lead to a high sensitivity of the amplifier to parasitic laser processes. Furthermore, as explained in Chapter 3, it potentially lowers the SBS threshold. On the other hand, seeding with very high power levels to reduce the gain and the ASE significantly also reduces the thermal gradient in the fiber, which is in turn essential for a high SBS threshold. Whether the first or the latter effect dominates in an amplifier strongly depends on the particular setup, including the fiber design. Thus, for every amplifier configuration, there is an optimum seed power level.

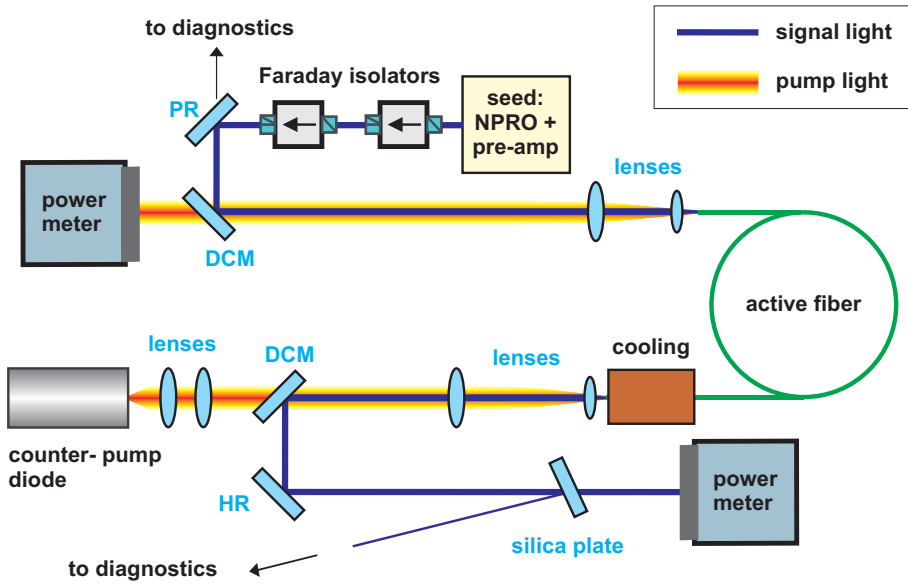


Figure 5.1: Experimental amplifier setup. PR: Partial reflector, DCM: dichroic mirror.

Table 5.1: Parameters used in the numerical calculation of the SBS threshold of the PCF amplifier for different seed power levels. The geometric fiber parameters are taken from the manufacturer's specifications and the Brillouin parameters from Ref. [205]. For the remaining parameters, the values utilized in Chapter 3 are deployed.

parameter	value	parameter	value
v_a	5960 m/s	r_{core}	20 μm
g_B	$5 \cdot 10^{-11}$ m/W	core NA	0.03
$\Delta\nu_B$	58 MHz	$r_{\text{inn. clad.}}$	200 μm
c_b	-0.2 MHz/K	$r_{\text{outer clad.}}$	350 μm
c_f	2 MHz/K	r_{polymer}	428 μm
α_s	0.001 m^{-1}	fiber length	6.8 m
Γ_s	0.85	doping concentration	$2.4 \cdot 10^{25}$ ions/ m^3

To get a rough estimate about the SBS threshold powers for different seed power levels, numerical simulations were carried out with the code presented in Chapter 3. The utilized parameters are summarized in Table 5.1 and are taken from References [78] and [205].

Fig. 5.2 shows the calculated backscattered power versus the amplifier output power. It can be seen that with the chosen simulation parameters, seeding with more than 7 W decreases the SBS threshold. Apparently for this amplifier configuration, the reduction in thermal gradient affects the SBS threshold more than the reduction of the amplifier gain

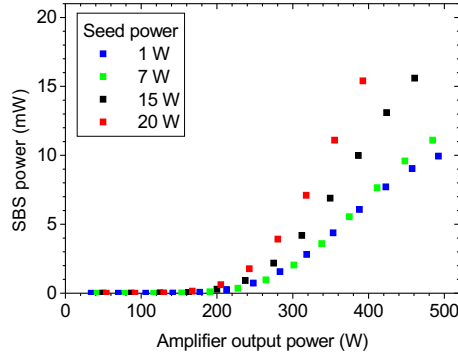


Figure 5.2: Numerically calculated Brillouin scattered power for the PCF amplifier. When the parameters from Table 5.1 were applied, the SBS threshold power was roughly the same for seed powers from 1 W to 7 W, but at that power level it started to decrease with increasing seed power.

does. Thus, for the preamplification of the NPRO-signal, a very simple setup was chosen, delivering about 8 W as seed power for the PCF. As active fiber, a step-index PM fiber with a 10 μm core (PLMA-YDF-10/125 by Nufern) was deployed, assuring single-mode seeding of the PCF amplifier. For improved long-term reliability, the preamplifier was set up as an all-fiber system. The 976 nm pump light from a 25 W fiber-coupled diode was launched into the active fiber via a fused-taper combiner (pump fiber core and cladding diameter: 105 μm and 125 μm respectively, core NA: 0.15). Throughout the experiments, the one-port fused-taper combiner was changed to a two-port combiner and a second pump diode was utilized. The upgraded preamplification stage delivered about 16 W as seed for the PCF amplifier. In both cases, a co-propagating pump scheme was chosen to protect the diodes.

Two 30 dB Faraday isolators protected this stage from backreflections of the main amplifier. A partial reflector (PR) was used to sample the backscattered light from the PCF, while the transmitted pump light was separated from the seed signal by a dichroic mirror (DCM). Mode matching of the seed signal to the fundamental mode of the PCF was achieved by a spherical lens with $f=100$ mm and an axial gradient lens with $f=10$ mm.

The main amplifier was pumped in a counter-propagating scheme, alleviating the alignment and abetting a higher SBS power threshold compared to a co-propagating pump (Section 2.2). The pump light from a temperature stabilized laser diode module, emitting at 976 nm, was delivered by a multi-mode fiber with a diameter of 600 μm and a NA of 0.22. It was collimated by a commercial water-cooled high-power collimator, and subsequently launched into the fiber through an $f=100$ mm spherical lens and an axial gradient lens with $f=15$ mm. A pump coupling efficiency of approximately 85 % could be achieved. After separation from the pump light by a dichroic mirror, the amplified signal passed through a silica plate, sampling part of the amplifier output beam for diagnostic purposes.

5.1.3 Amplifier characterization

In Fig. 5.3 (a), the amplifier output power is plotted versus the absorbed pump power (black squares). Assuming a pump coupling efficiency of 85 %, the differential optical-to-optical efficiency was calculated to be 80 %, and the polarization extinction ratio (PER) of the system at an output power of 11 W was 23 dB. At 246 W of output power, the PER was measured to be even 27 dB. Detecting the optical amplifier output spectrum at this power level yielded a signal-to-noise ratio (SNR), i.e. an ASE suppression, of more than 50 dB (resolution of the OSA set to 0.5 nm) (Fig. 5.3 (b)). Nevertheless, at an absorbed pump power of 363 W and a corresponding output power of 294 W, parasitic laser processes occurred, limiting the power scaling of the amplifier.

The parasitic laser processes became manifested in additional laser spikes in the forward optical spectrum. Possible sources of a parasitic resonator are backreflections from optical components, but this typically occurs at amplifier gain levels of about 20 dB. In this case, the amplifier gain was only about 16 dB. Reducing the number of optical elements in the amplifier output beam path to a minimum and trying out optics with different anti-reflective coatings, however, did not push the onset of the parasitic processes to higher power levels. To ensure that the fiber end preparation did not cause this lasing, they were repolished after the amplifier characterization with this particular fiber sample was finished. Moreover, to eliminate defects of this particular fiber sample as the origin, a second 6.8 m long sample of this PCF was prepared and implemented into the amplifier. Still, the output power scaling limit remained at about 300 W. Doubling the seed power to 16 W led only to a very slight increase of the extracted amplifier output to about 320 W before the parasitic processes set on. Placing the seed-end of the PCF as well as the preamplifier output end in water-cooled copper v-grooves to thermally stabilize the seed-beam path did not improve the amplifier performance, either.

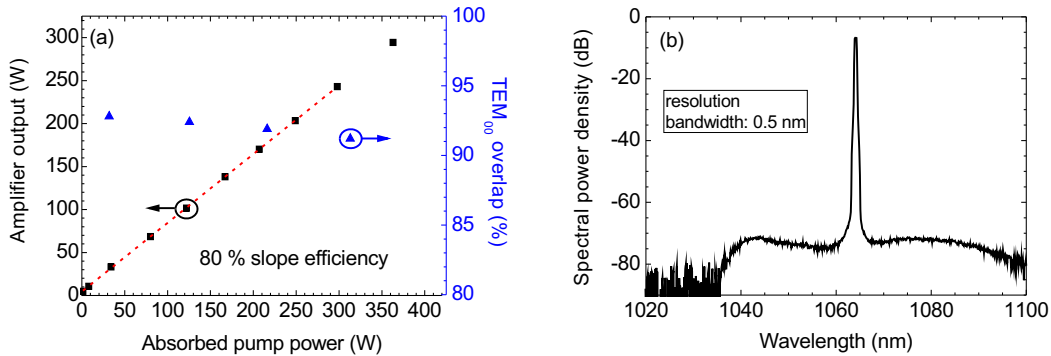


Figure 5.3: (a): Total signal output power at 1064 nm (squares) and fractional TEM₀₀ mode content of the beam, emitted from the fiber core (triangles), versus absorbed pump power at 976 nm. (b): Output spectrum at 246 W of output power. With a resolution bandwidth of the optical spectrum analyzer set to 0.5 nm, the SNR, indicating the ASE suppression, was measured to be >50 dB.

Another possible origin could have been lasing on a higher order mode, enabled either by TSHB or TMI (Section 4.3). In this case, the higher order mode would have experienced a significantly higher gain compared to the 16 dB of the fundamental mode. On the other hand, the most prominent manifestation of TMI, a wobbling beam profile, was not observed for this amplifier configuration. Another argument contradicting the TMI explanation is the sudden rise in the amplifier RIN at 294 W of output power (Fig. 5.4 (a)). As explained in Section 4.3.2, the overall output power remains constant at the onset of TMI and only the utilization of an aperture to transversely sample the beam converts the beam profile fluctuations into intensity noise. Nevertheless, further investigations on this issue were not carried out at this point, to prevent the fiber as well as all other components from being damaged.

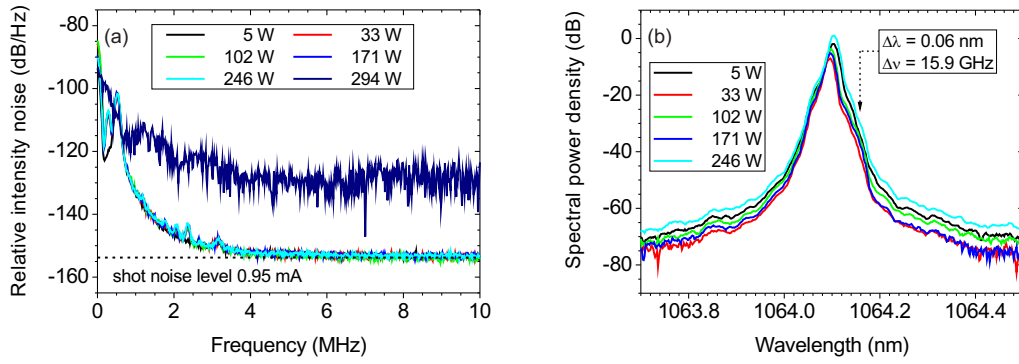


Figure 5.4: (a): Evolution of the relative intensity noise with increasing output power. The sudden rise of the noise level at 294 W of output power was most likely due to the onset of parasitic laser processes. (b): Optical spectra of the backward propagating signal with increasing amplifier power. An increase in the Stokes peak (wavelength marked by the dashed arrow) could not be observed even at the highest output power level, verifying SBS free operation.

The RIN was actually measured to monitor the possible onset of SBS. This was however not the case, as confirmed by the evolution of the optical spectra (Fig. 5.4 (b)), measured from the backward propagating light. This consisted mainly of Rayleigh scattered and back-reflected light with the same wavelength as the signal light, which can be clearly seen in Fig. 5.4 (b). The SBS induced Stokes peak would have appeared at a frequency shift of about -15.9 GHz, corresponding to a wavelength shift of about 0.06 nm with respect to the signal. This wavelength value was measured from SF amplifier operation of a 9 m piece of the same PCF, where the Stokes peak appeared at a power level of 50 W. In Fig. 5.4 (b), the Stokes wavelength is marked by the dashed arrow. For the amplifier seeded with 16 W, the backward optical spectra looked alike, indicating operation below the SBS threshold.

To evaluate the beam quality in terms of its modal decomposition and in particular the power in the TEM_{00} mode, the nonconfocal three mirror scanning ring cavity described in Section 4.1 was used. Due to the excellent PER, the losses at the polarization optics in

the beam path to the cavity were negligible. However, 9.5% of the power was contained in cladding modes. Compared to the seed power, the cladding loss was quite high, diminishing seed misalignment as possible source. It rather originated from scattering of the fundamental mode or even a HOM at fiber anisotropies. Fiber anisotropies can arise either during production of the fiber preform or during the drawing process. NKT photonics uses a so called stack and draw technique to manufacture photonic crystal fibers. The core is a composite of several rods, supposedly uniformly doped. Unfortunately, inhomogeneities occur often, when a new fiber design is fabricated for the first times (a similar issue will be discussed in Section 5.2.2). In fact, this explanation is much more likely than bending losses, as the same bending radius was used for another 6.8 m piece of the same PCF. The performance of this fiber piece in terms of slope efficiency, SNR and output power limit due to parasitic lasing processes was the same as for the piece described in the paragraphs above. The amount of residual cladding light, however, was only about 6%.

In order to investigate a potential decrease of the overlap between the beam emitted from the fiber core and the fundamental cavity mode, mode scans were carried out at different power levels. The corresponding measured TEM_{00} mode overlap values are inserted in Fig. 5.3 (a) (blue triangles). At an amplifier output power of 33 W, already 7.2% of the power were contained in higher order modes. This value increased only slightly to 7.6% at 102 W of total amplifier output power. Increasing the amplifier output to 171 W yielded a HOM overlap of 8.1% of the core signal.

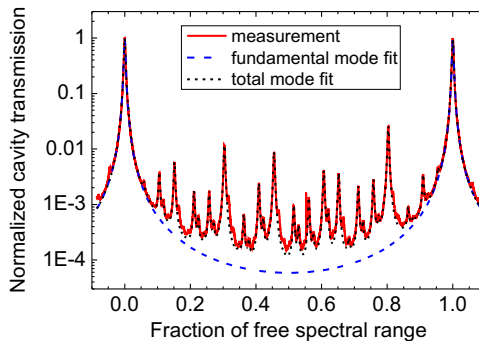


Figure 5.5: Mode scan signal on a logarithmic scale at an amplifier output power of 246 W. The resulting 8.8% HOM power fraction of the beam, emitted from the fiber core, was distributed among several higher order cavity modes.

The transmission signal of a complete sweep through one FSR of the mode scanning cavity at 246 W of output power is presented in Fig. 5.5. At this power level, 8.8% of the core signal could not be coupled to the fundamental cavity mode. Congruently, the TEM_{00} mode content of the beam emitted from the fiber core was 91.2%. This yielded, together with subtracting the residual cladding light, a fractional TEM_{00} mode power of 203 W in linear polarization state.

Interestingly, the measured HOM content of this fiber's core light was higher than for the 1.45 m long PCF sample from the experiments in Section 4.3. There, the HOM content at an output power level of 73.9 W was measured to be only 5.1%. That fiber had a slightly smaller core ($38\ \mu\text{m}$ instead of $40\ \mu\text{m}$), and was specified with the same MFD and NA. The critical difference of the fiber geometries, however, was most likely not the core size but the stress rod size and shape. Fig. 5.6 shows the cross-sections of the two fibers for comparison. The problem with the DC-400-40-PZ-Yb fiber was probably related to the fact that the smaller air holes surrounding the core collapse longer than the air clad holes during the heating process [202, 206]. Polishing the fiber end so that the air holes are just sealed might have resulted in an already too long collapse length of the inner air hole structure, leading to disturbance of the output beam by the boron-doped cladding region (Section 4.2.2). The stress-rods were larger and more oblong than for the DC-400-38-PZ-Yb.

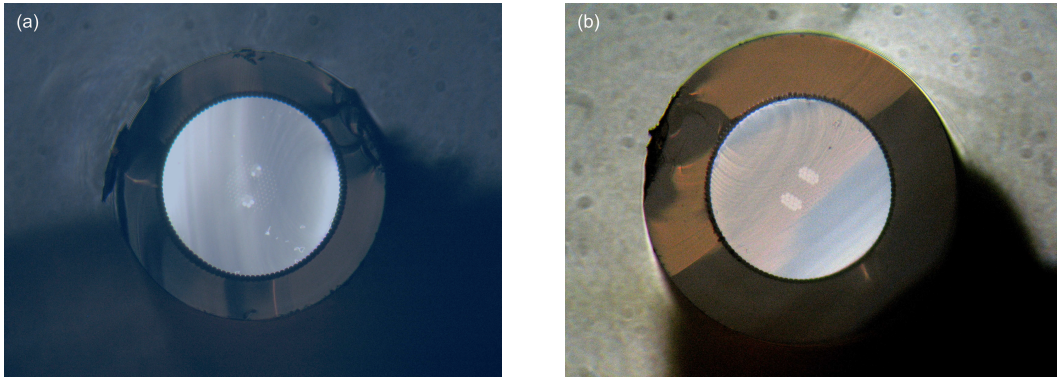


Figure 5.6: Cross-section of the (a): DC-400-38-PZ-Yb and (b): DC-400-40-PZ-Yb used for the experiments described in Chapters 4.3 and 5.1. The most obvious and probably crucial difference is the size and shape of the boron-doped stress rods, which are larger and more oblong for the latter fiber. This is most likely the origin for the beam quality's sensitivity to the fiber end preparation.

In fact it was found that the TEM_{00} mode overlap of the beam emitted from this particular fiber was extremely sensitive to the fiber end preparation. After the aforementioned repolishing of the fiber ends, the TEM_{00} mode overlap of the core light was only 87%. This value was measured at total amplifier output powers of 103 W, 202 W and 302 W, thus apparently independent of any absorption and gain effects. Due to this issue, endcapping of this fiber, which could have prevented the parasitic laser processes, was not an option. Unfortunately, NKT photonics had used spools with a too small bending diameter (20 cm) for the DC-400-38-PZ-Yb, so that the fiber was very prone to breaking, even untouched on the fiber spool. All available samples had fiber length ≤ 3 m, and power scaling was limited by TMI at power levels below 200 W.

For a potential GWD laser system, a fiber with a modal performance similar to the DC-400-38-PZ-Yb is highly favorable compared to the DC-400-40-PZ-Yb. In fact, even

more advanced PCF designs should be employed, as by the time the experiments presented in this Section were carried out, the SBS threshold for a very similar fiber geometry was identified by Robin et al. to be about 400 W [205]. The seed power in this case was about 15 W [202], but instead of trying out different external mitigation techniques to increase the SF output power, they developed a PCF with the same geometric dimensions, but an intrinsic SBS suppression through acoustic core segmentation [21]. No SBS was observed even at about 500 W of single-frequency output, but further output power scaling was limited by the onset of TMI [184]. In order to overcome this limitation, a third fiber design was tested. The core of that fiber consisted of doped as well as undoped segments, yielding preferential gain of the fundamental fiber core mode. Due to the resulting reduced absorption, a longer fiber length had to be utilized and in order to obtain 990 W of output power, a bandwidth broadened signal (about 300 MHz instead of a few kHz) had to be deployed [184]. Hence, to extract about 1 kW of kHz-linewidth output from one amplifier chain, still new fiber designs need to be developed. The current technology's state of the art makes coherent beam combination of two acoustically segmented 30 μm -MFD PCF amplifiers with about 500 W of single-frequency output much more likely to fulfill the requirements for a 3rd generation 1064 nm GWD laser system. These developments in PCF design and fabrication are one of the arguments leading to the conclusion that further attempts to eliminate the parasitic laser processes, limiting the output power of the amplifiers analyzed in this Section, would involve a lot of technological effort, but yielding only marginal scientific output.

Furthermore, the results presented in this Section already indicate that with proper design (in terms of stress rod geometry), fabrication (to reduce anisotropies in the core that can cause high fractional power scattering of the fundamental mode into the fiber cladding) and coiling diameter (rather around 40 cm than 20 cm), a bendable PCF with a 30 μm -MFD at 1064 nm should be able to deliver a TEM_{00} mode content larger than 90% at power levels at least up to 300 W. Considering the decrease in TEM_{00} mode overlap for increasing total amplifier output power, especially for the DC-400-40-PZ-Yb, no significant beam quality degradation should occur as long as the amplifier operates below the TMI power threshold (Section 4.3). Thus, 90% TEM_{00} modal power fraction should be achievable even at 500 W. Regarding the evolution of the beam quality with increasing amplifier output, NKT has obviously already improved the fiber design compared to what has been characterized in Ref. [23]. For that PCF, it had a nominal MFD of 22 μm at 1060 nm, the HOM content of the amplifier output beam increased from only 2% at 28 W to 7% at the maximum output power of 148 W.

Besides the developments in the PCF design concept, a completely different fiber design to achieve effective single-mode operation of active LMA fibers was pushed towards larger core diameters and resulting MFDs during the work for this thesis. From a scientific point of view the most interesting subject to study at this point was the performance of this alternative fiber design concept, namely chirally coupled core fibers (Section 2.3.2). These experiments are presented in the following Section.

5.2 Amplifiers with CCC fibers

As the nonconfocal ring cavity, used to decompose the beam emitted from the fibers into the free-space TEM_{nm} modes, was designed for 1064 nm, only CCC fibers operating at this wavelength could be deployed. Three different fiber geometries were available. Two of them differed only in the cladding geometry. All design parameters for their round-shaped core with a diameter of $37\ \mu\text{m}$ were the same. About these fibers it was actually known from pre-tests, carried out by the fiber designer group of Prof. Galvanauskas at the University of Michigan that they did guide one higher order mode. This was attributed to a non-optimized production process at the time the fibers were drawn. From a scientific point of view it was still interesting to see if this higher order mode could be suppressed by proper excitation of the fundamental mode and how much TEM_{00} mode overlap this yielded. The third active fiber under test had the same core design as the passive version characterized in Section 4.2.3, where the general capacity of the CCC fiber design concept to obtain an effectively single-mode signal core with a large MFD has already been demonstrated. In particular, this fiber had a $55\ \mu\text{m}$ core diameter, hence larger than what is available for bendable PCFs. For this core design, direct comparison of an active to a passive fiber version was possible. For active fibers, the fabrication process in terms of controlling the different modes' effective refractive indices and hence their propagation constants can be aggravated by the doping of the core, as it changes the core's refractive index. Furthermore, the implementation of a double- or triple-clad structure to guide the pump light always enables the guiding of HOMs, at least in the cladding. Thus it was interesting to study the impact of these structures on the overlap of the beam emitted from the fiber and the TEM_{00} mode.

5.2.1 $37\ \mu\text{m}$ core diameter fibers

The cross-sections of the two $37\ \mu\text{m}$ core fibers are shown in Fig. 5.7. One sample had only a double-clad (DC) structure and unfortunately, the cladding had a round shape (Fig. 5.7 (a)). It led to a very low absorption of only about 1 dB/m, because a large fraction of the pump light could propagate through the cladding as helical rays, which do not cross the core. The other fiber sample had an additional inner cladding, surrounded by an air-clad, as can be seen in Fig. 5.7 (b). This air-clad structure was sufficient to break the symmetry of the fiber geometry, disabling the formation of helical pump light rays. The parameters of the two $37\ \mu\text{m}$ -core fibers are summarized in Table 5.2.

For the amplifier setup, basically the same was used as for the PCF experiments (Fig. 5.1), but some changes were undertaken regarding the cooling arrangements. Water-cooled lens mounts were utilized, and the whole fiber was now actively cooled on a water-cooled aluminum plate. To optimize the contact to the fiber, the aluminum plate was covered with a thin thermal conduction pad and the fiber was coated with a thin film of thermal grease. This was especially important for the DC fiber version, as the material for the coating was primarily chosen to achieve the desired index-difference to the cladding. These

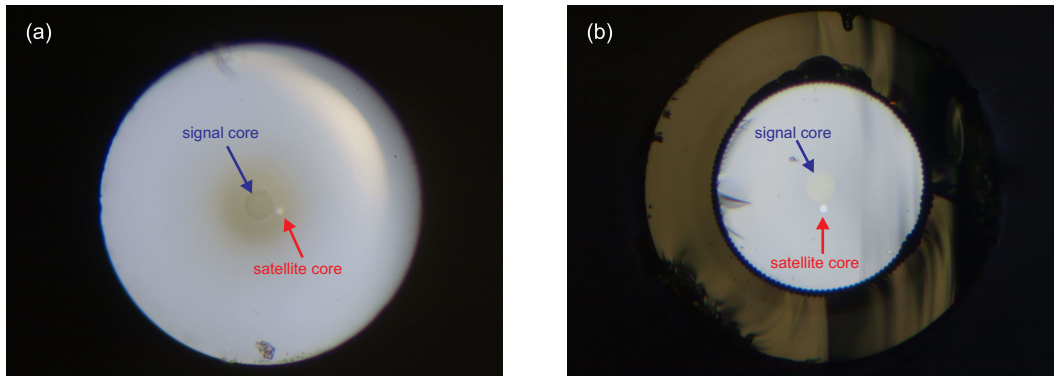


Figure 5.7: Cross-section of the (a): double-clad version and (b): the air-clad version of the $37\ \mu\text{m}$ core CCC fiber. The air-clad structure was sufficient to break the symmetry of the pump cladding geometry and prevent the formation of helical pump rays that do not cross the core. Accordingly, the absorption at $976\ \text{nm}$ was with about $9\ \text{dB/m}$ much higher than the $1\ \text{dB/m}$ for the DC fiber with the round pump cladding.

coating materials typically start to burn at lower temperatures than the high-temperature acrylate that can be utilized when pump-light guiding is obtained through an inner air-clad structure (Section 2.3). Additionally, the coating of a DC fiber is in direct contact with pump light, potentially absorbing the evanescent cladding modes. This further conduces to a critical coating temperature at moderate pump power levels, compared to an air-clad fiber.

First amplifier tests were carried out with a $5\ \text{m}$ long sample of the DC fiber, coiled to a diameter of $30\ \text{cm}$ and only seeded with $130\ \text{mW}$. The signal output power was increased from $3.4\ \text{W}$ to $19.8\ \text{W}$. Assuming a pump coupling efficiency of 78% , this corresponded to absorbed pump power levels of $9.8\ \text{W}$ and $33.8\ \text{W}$, respectively, and yielded a differential optical-to-optical efficiency of about 69% . The measured PER was for all power levels between $15\ \text{dB}$ and $16\ \text{dB}$, while the measured TEM_{00} mode overlap decreased slightly from 97% to 93% with increasing amplifier output power. These values for the TEM_{00} mode content were obtained by optimizing the seed-to-fiber coupling at every power level. Through misalignment of the seed signal, the presence of the HOM in the amplifier output beam was clearly observable and led to a significant decrease in the measured TEM_{00} mode content. However, these measurements indicate at least a very good overlap of the fundamental fiber mode with the TEM_{00} mode. Additionally, a decrease in the TEM_{00} mode content of 4% for an amplifier gain of $\sim 22\ \text{dB}$ is still comparable to what has been reported [23] or measured (Section 5.1) with fibers, where the beam quality was less sensitive to the seed alignment.

For the studies of the modal performance at higher power levels and higher temperatures due to absorption, a seed power of about $11.5\ \text{W}$, hence a power level one magnitude higher than before, was utilized. Everything else in the amplifier setup remained unchanged. In Fig. 5.8 (a), the amplifier output power is plotted versus the absorbed pump power,

Table 5.2: Parameters of the active CCC fibers with a round core of $37\ \mu\text{m}$ diameter. One sample had an additional air-clad, the other one only a DC-structure. The low absorption of the DC-fiber was due to the round shape of the cladding.

core diameter	$37\ \mu\text{m}$
MFD	$30\ \mu\text{m}$
core shape	round
core NA	0.068
number of satellite cores	1
satellite core diameter	$9.8\ \mu\text{m}$
satellite core NA	0.089
edge-to-edge distance of central core and side cores	$3.5\ \mu\text{m}$
helix period	6 mm
recom. bend. diameter	20 cm - 30 cm
absorption at 976 nm	$\sim 1\ \text{dB/m}$ & $9\ \text{dB/m}$
inner cladding diameter	none & $260\ \mu\text{m}$
inner cladding NA	none & 0.6
outer cladding diameter	$413\ \mu\text{m}$ & $440\ \mu\text{m}$
outer cladding NA	0.46

assuming a pump coupling efficiency of about 78%. This yielded an optical-to-optical amplifier slope efficiency of 75%. The experiments were stopped at about 157 W of output power due to the high amount of transmitted unabsorbed pump.

Fig. 5.8 (b) shows the measured values for the PER and TEM_{00} mode content of the amplified signal at different power levels. The seed alignment was optimized at every power level for the highest fractional TEM_{00} mode content. For the PER, the measured values were in the range between 14 dB and 19 dB. At 55 W of amplifier output power, corresponding to a gain of ~ 6 dB, a TEM_{00} mode content of 93% was obtained. Interestingly, the cavity transmission was lower as for the low-power seeding at a comparable gain level (97% at a gain of about 8 dB). This could be caused by a higher seed power fraction launched into either cladding modes or the higher order core mode, but at this power level it is indistinguishable what was actually the case. The latter is more likely, as just launching more power into cladding modes at low pump power levels should yield a higher fundamental mode content with increasing amplifier output. At 157 W of output power, corresponding to a gain of ~ 11 dB, a TEM_{00} mode overlap of only 88% was measured. The HOM suppression for this fiber is apparently rather sensitive to the pump power level and the corresponding absorption. Total gain and inversion on the other hand seem to be less critical parameters.

For the air-clad fiber version, a 2.2 m long sample was deployed, which was sufficient to get a reasonable absorption. One more change in the setup compared to the DC fiber

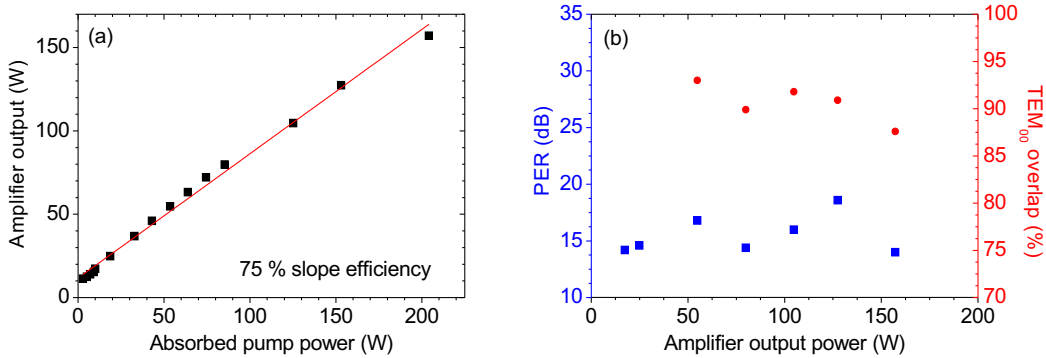


Figure 5.8: (a): Amplifier output power versus absorbed pump power for a 5 m long sample of the DC fiber, assuming a pump coupling efficiency of 78 %. (b): PER and TEM₀₀ mode content of the amplified signal for different amplifier power levels. The experiments were stopped at 157 W of extracted 1064 nm signal due to the high amount of transmitted unabsorbed pump light.

experiments was conducted. The focal length of the lens to pre-focus the pump beam was changed from 100 mm to 300 mm in order to achieve mode-matching into the smaller pump cladding with larger NA of the air-clad fiber. As for the DC fiber, the first TEM₀₀ mode content measurements were carried out with low-power seeding of about 130 mW. At a signal output power level of 4 W, the performance of this fiber was comparable to the DC version. The measured PER and TEM₀₀ mode overlap were 19 dB and 95 % respectively. Even though the core designs were the same, the modal performance of the air-clad version decreased with increasing amplifier output power, even though the seed coupling was realigned for maximum TEM₀₀ mode power extraction. At 34 W of signal output power and a corresponding gain of about 24 dB, the PER was measured to be only 13 dB and the best obtained fundamental mode scan result had decreased to only 88 %. While the HOM suppression of the DC version was not so much affected by the inversion, the air-clad fiber's modal performance was apparently prone to it.

In the TEM₀₀ mode power scaling experiments, the seed power level was set to 11.5 W in order to decrease potential issues arising from a high amount of ASE. The amplifier output power versus the absorbed pump power is plotted in Fig. 5.9 (a). Assuming a pump coupling efficiency of 73 %, a differential optical to optical efficiency of 75 % was obtained. Beyond 230 W of signal power, TMI set on, limiting the TEM₀₀ mode power extraction, and the experiments were stopped. In fact, this represents the first experimental evidence of TMI occurrence in a CCC fiber.

Fig. 5.9 (b) displays the measured values for the PER and the TEM₀₀ mode overlap at different amplifier output power levels. A slight increase in the TEM₀₀ mode power was observed, when the amplifier output power was increased from 19 W to 49 W. This was due to an increase in the TEM₀₀ mode content from 96 % to 97 %, accompanied by

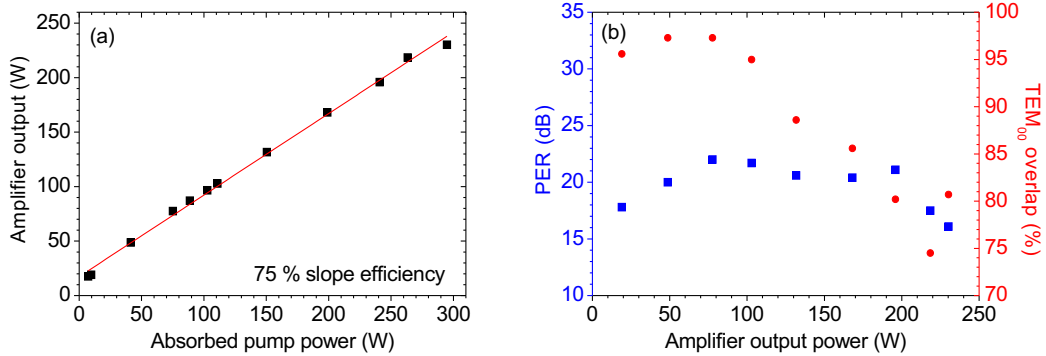


Figure 5.9: Amplifier output power versus absorbed pump power for a 2.2 m long sample of the air-clad fiber, assuming a pump coupling efficiency of 73%. (b): PER and TEM₀₀ mode content of the amplified signal for different amplifier power levels. Beyond 230 W of signal output, the amplifier power scaling was limited by transverse modal instabilities.

an increase in the PER from 18 dB to 20 dB, indicating preferential amplification of the fundamental mode compared to cladding and higher order core modes. At 78 W, the PER was measured to be even 22 dB, and it remained above 20 dB up to a signal power of 196 W. The TEM₀₀ mode overlap decreased already significantly beyond 103 W of amplifier output. Fig. 5.10 (a) shows the best mode scan result obtained at this power level, which yielded a TEM₀₀ mode content of still 95 %. At 132 W of signal output, only 89 % of the power could be coupled into the fundamental cavity mode, despite optimized seed alignment. This value decreased further with increasing signal power. The best mode scan result at 230 W is shown in Fig. 5.10 (b) and corresponded to only 81 % fundamental mode content. Together with the measured PER of 16 dB, it yielded a maximum extracted TEM₀₀ mode power from this amplifier configuration of 182 W. Fig. 5.10 (b) indicates that the power in the higher order core mode was rather distributed among several cavity modes than into a particular one.

Further TEM₀₀ mode power scaling was tried with a 2.6 m long sample of the same air-clad fiber spool, as a longer fiber length is one parameter to increase the power threshold for TMI. The modal performance of this fiber sample was nevertheless not as good as the one characterized above. At 48 W of signal power, the TEM₀₀ mode overlap was 94 %, hence 3 % lower than for the first air-clad fiber sample. Another indicator of an inferior HOM suppression was the PER of only 15 dB instead of more than 20 dB. Increasing the amplifier output power to 104 W improved the PER to 16 dB, but for the fundamental mode content only 91 % was the best obtained result. The highest signal power level, where mode scans could be carried out, was 211 W. While the measured PER remained at 16 dB, the TEM₀₀ mode overlap had decreased down to only 78 %. Further increase of the amplifier output led to the onset of TMI. Using an additional upper cold-plate for the main body of the fiber did not push the TMI threshold to a higher power levels. Thus no

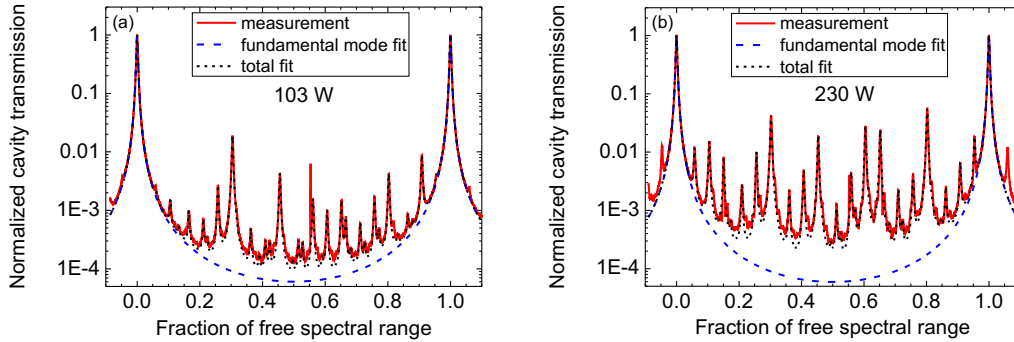


Figure 5.10: The best obtained mode scans at (a): 103 W and (b): 230 W of signal output power, corresponding to fundamental mode contents of 95 % and 81 % respectively. This difference can be clearly seen, comparing the height of the higher order cavity modes. Additionally it shows that the HOM, responsible for the decreased beam quality, was not matched to one particular cavity mode, but its power fraction was distributed among several higher order cavity modes.

experiments were carried out beyond this amplifier output power.

The presented experiments reveal an interesting feature of the drawing process. Although both fiber samples had not only the same design, but were drawn from the same preform, the HOM was much easier to excite and amplify for the latter sample. Apparently, the CCC fiber design concept is very sensitive to slight differences in drawing speeds and temperatures along one fiber spool.

Even though the fiber samples analyzed in particular in this Section are not suitable for future GWD application, the obtained experimental results indicate a general potential for this fiber design concept. The TEM_{00} mode scan results obtained for low-power seeding of the DC fiber, indicate at least that its fundamental fiber mode has an excellent overlap with the TEM_{00} mode. In terms of power scaling, 511 W of 1064 nm SF signal output have been demonstrated with a fiber sample of the same geometric design, but taken from another drawing spool [20]. Those amplifier experiments were apparently only limited by heating of the fiber, as the onset of SBS or TMI was not reported. Considering the results presented in this Section, such an amplifier should have a fundamental mode content of at least 80 % at the reported power level. Otherwise TMI should have set on. Unfortunately, that particular fiber sample was not available anymore.

The insufficient HOM suppression of the fiber samples analyzed in this Section was attributed to the drawing process [207]. It is still an open question, if this can be optimized to obtain full HOM suppression. Depending on the degree of HOM suppression, a SF amplifier deploying the presented fiber design will be limited between 200 W and 500 W, either by TMI or heating of the fiber. Both issues are of thermal origin, thus their impact can be reduced by decreasing the absorption. This in turn would require to utilize longer fiber lengths to obtain reasonable pump light absorption, and eventually SBS will be

an issue. Fine tuning of the fiber parameters to get the highest SF power scaling limit, considering critical fiber heating, SBS and TMI will need to be done. Thus, the CCC fiber technologies with core MFDs of about $30\ \mu\text{m}$ is facing the same limitations and trade-offs as the PCF design concept with roughly the same MFD size. From the current state of the art, to reach TEM_{00} mode power levels beyond 500 W, coherent beam combination of two amplifiers will be most likely the solution for both technologies.

Further increase of the MFD would allow for the utilization of longer fiber lengths, enabling a reduction in the absorption and pushing thermal issues to higher amplifier power levels. For the PCF design concept, however, the MFD of bendable fibers is restricted to about $30\ \mu\text{m}$. Increasing the core diameter yields only larger MFDs, if the fiber is kept straight. Otherwise, the bending induced mode area shrinking diminishes the advantages of the larger core size [206, 208]. Moreover, in order to ensure effective single-mode operation, PCFs with larger cores require very low NAs, which makes the fiber's FM very sensitive to bending induced loss [50]. Therefore, PCFs with core diameters of $70\ \mu\text{m}$ and larger are rod-type fibers, typically of length no longer than 1 m [199]. This design is very suitable for short-pulse amplification due to the high power thresholds for nonlinear effects and the short pulses deliver enough peak intensity to saturate the highly doped rods. Deploying such a rod-type fiber in a SF signal amplification system designed to deliver more than 500 W of TEM_{00} mode power would require seed power levels probably between 50 W and 100 W, resulting in increased amplifier system complexity. Additionally they are currently limited by TMI mostly below 500 W [177, 185]. For the CCC fiber design concept on the other hand, mode area scaling of bendable fibers is still investigated. A prototype fiber sample with a $55\ \mu\text{m}$ core diameter could be analyzed within the work for this thesis. The experimental results are presented and discussed in the Section below.

5.2.2 $55\ \mu\text{m}$ core diameter fibers

The active CCC fiber with the $55\ \mu\text{m}$ core diameter had the same core design as its passive counterpart presented in Section 4.2.3. It had an octagonal core shape and the nominal core NA was 0.072. The corresponding MFD at 1064 nm was calculated to be $42\ \mu\text{m}$. An image of the fiber's cross-section is depicted in Fig. 5.11, revealing 8 satellite cores instead of 1 for the $37\ \mu\text{m}$ core fibers. Further differences in the CCC structure can be found in the helix period and the edge-to-edge distance of central core and side cores, while satellite core diameter and NA were roughly the same as for the $37\ \mu\text{m}$ fibers. All fiber parameters of the $55\ \mu\text{m}$ fiber are listed in Table 5.3. It had a triple clad structure to obtain an NA of 0.22 for the $312\ \mu\text{m}$ diameter inner cladding. Its octagonal shape was chosen to disable the formation of helical pump rays. Both design parameters together led to a nominal absorption of 10 dB at 976 nm. The outer cladding had a slightly larger diameter of 368 nm and a higher NA of 0.46. The latter was due to the fact that the fiber was finally coated with an acrylate coating.

Experiments by the group of Prof. A. Galvanauskas from the University of Michigan had already revealed some issues regarding the power scaling potential of this prototype fiber.

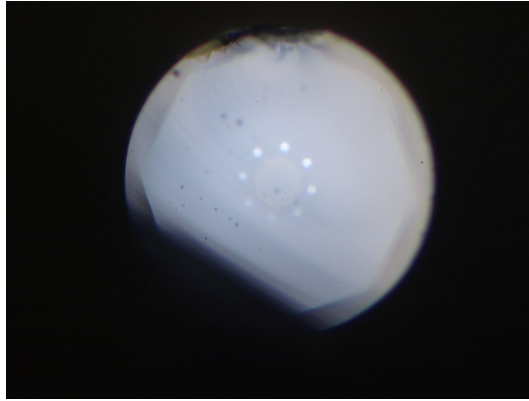


Figure 5.11: Cross-section of the 55 μm diameter core fiber. It had eight satellite cores and a triple-clad structure was used to obtain an NA of only 0.22 for the inner cladding. This had an octagonal shape to prevent the pump light from propagating as helical rays.

Table 5.3: Parameters of the active CCC fibers with a octagonal core of 55 μm diameter and a triple-cladding structure.

core diameter	55 μm	MFD	42 μm
core shape	octagonal	core NA	0.072
number of satellite cores	8	satellite core diameter	10 μm
satellite core NA	0.088	edge-to-edge distance of	
helix period	5.3 mm	central core and side cores	7 μm
recom. bend. diameter	40-50 cm	absorption at 976 nm	10 dB/m
inner cladding diameter	312 μm	inner cladding NA	0.22
outer cladding diameter	368 μm	outer cladding NA	0.46

Depending on the seed power and the coiling diameter, they had obtained a maximum differential optical-to-optical efficiency of only about 50 %, which is quite low for an ytterbium-doped fiber. Additionally, they have observed that about one third of the output power was emitted from the cladding. This value could not be significantly reduced by further optimizing the seed alignment or increasing the gain factor. Power scaling was limited to only a few tens of watts due to immense heating of the first few millimeters of fiber at the pump end. Thus, the experiments presented below were carried out by using the setup depicted in Fig. 5.1.2, but with the additional aluminum cold plate, as described for the 37 μm fibers. Only the 15 mm focal length lens was water-cooled, as the maximum expected pump power level did not exceed 100 W. Even though the fiber heated up very fast, neither the upper plate for the water-cooled copper v-groove, mounting the fiber end, nor the upper plate for the aluminum cold plate for the main fiber body, were used. Unfortunately, the fiber's efficiency was very prone to mechanical stress and damaging the

fiber by the weight of the plates was too risky at the beginning of the experiments.

The length of the operated fiber sample was 2.1 m and it was first coiled to 34 cm and tested with low-power seeding of 190 mW. Assuming a pump coupling efficiency of 70 %, the amplifier slope depicted in Fig. 5.12 (a) was obtained. With only 26 %, the optical-to-optical efficiency was very poor, but this can be attributed to the coiling diameter, which was smaller than the recommended range. About 30 % of the amplifier output power were emitted from the cladding and cut off, before a sample of the beam was taken for PER and mode content measurements. These values are plotted in Fig. 5.12 (b) versus the total amplifier output power. Turning the amplifier output from 0.8 W to 1.4 W led to a slight increase in the TEM₀₀ mode overlap from 92 % to 93 %. Meanwhile, the PER improved from 10 dB to 21 dB. Both observations can most likely be related to an improved seed coupling and mode-matching at the higher power level, which to a certain point alleviates the alignment. Between about 2 W and 3 W of amplifier output power, the PER and TEM₀₀ mode content remained approximately the same, being around 19 dB and 92 %, respectively. At a total amplifier output of 4.6 W, the TEM₀₀ mode overlap had decreased down to 89 %, while the PER was measured to be still 18 dB.

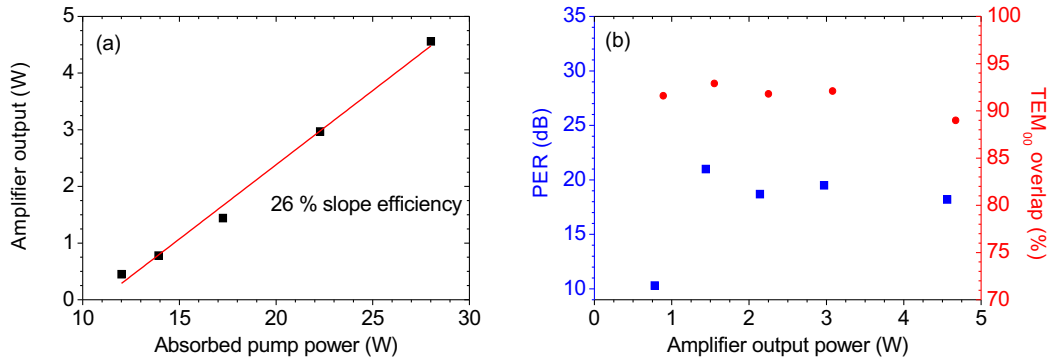


Figure 5.12: (a): Total amplifier output power versus absorbed pump, assuming a pump coupling efficiency of 70 %, for the 2.1 m long sample of the 55 μm diameter core CCC fiber. The seed power level and coiling diameter in this case were 190 mW and 34 cm, respectively. (b): Measured PER and TEM₀₀ mode overlap of the beam, for the same amplifier configuration. The presented values have been measured after the cladding light, containing about 30 % of the power, had been removed with an aperture.

Exemplary mode scans at 1.4 W and 4.6 W of amplifier output power are depicted in Fig. 5.13. Just as for the passive counterpart, the predominant higher order cavity mode is located at 0.61 FSR and can be traced back to excitement by the fiber's FM (Section 4.2.3). This is consistent with the experimental observation that the power fraction in the cavity mode at 0.61 FSR could not be influenced by seed-alignment or mode-matching, but was only sensitive to the size of the aperture, used to cut-off the cladding light. Unfortunately, the origin of the increasing amount of power, distributed over other higher order cavity modes for 4.6 W (Fig. 5.13 (b)) of amplifier output, compared

to the case of 1.4 W (Fig. 5.13 (a)) is ambiguous, which is a weakness of the measurement procedure. A higher order cavity mode content could be a result of an increased amount of power distributed among higher order core modes. Likewise, either the overall amount of cladding light or the fraction coupled into the cavity could have become higher with increasing amplifier power. Unfortunately, ensuring a constant fraction of coupled cladding light is quite difficult in a laboratory amplifier setup. Slight mechanical vibrations and thermal issues such as fiber end drifting and MFD shrinking can not be fully inhibited.

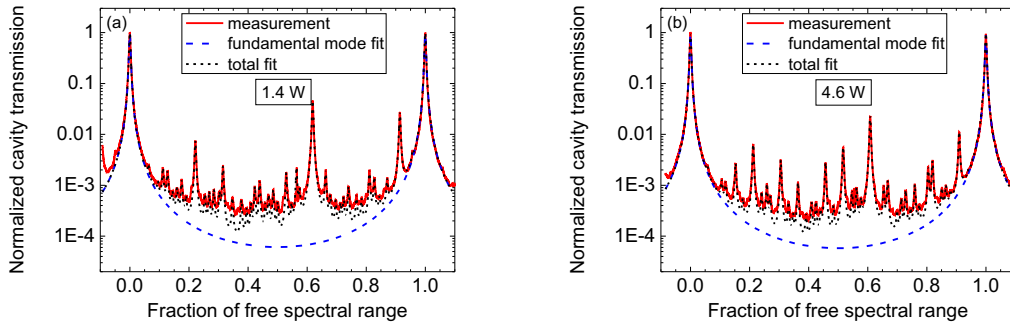


Figure 5.13: Representative mode scan results for 190 mW of amplifier seed power and a fiber coiling diameter of 34 cm, measured at (a): 1.4 W of total amplifier output, corresponding to 93 % fundamental mode content and (b): at 4.6 W of total amplifier output, corresponding to 89 % fundamental mode content. In all scans obtained for the 55 μm core diameter fiber sample, the cavity mode at ~ 0.61 FSR was the predominant HOM.

Yet, even the best results obtained for this fiber were not meeting the performance of its passive counterpart presented in Section 4.2.3. The most obvious explanation for this is related to the ytterbium doping. It raises the refractive index and aggravates the control of the index difference between core and cladding, which in turn affects the shape and size of the mode field. It is possible that the fundamental mode of the active fiber had a lower overlap with the TEM_{00} mode than the fundamental mode of the passive counterpart.

Increasing the seed power to 1 W did only improve the differential optical-to-optical efficiency to 40 %. The power fraction in the cladding as well as the PER and TEM_{00} mode overlap values were about the same as for the 190 mW seeding case. At 7.6 W of total amplifier output, TEM_{00} mode content measurement yielded 91 %, while a PER of 22 dB was obtained. The amplifier was tested up to 12.5 W, where the PER and TEM_{00} mode content were measured to be 19 dB and 89 %, respectively. Changing another setup parameter, however, did affect the modal power distribution. With a coiling diameter of 45 cm, which was now in the recommended range, the slope efficiency increased to ~ 45 %, but the best mode scan result (Fig. 5.14), obtained at 1.8 W of total amplifier output, corresponded to only 88 % fundamental cavity mode content. Additionally, the PER was measured to be only 15 dB. These observations can be most likely traced back to one or a combination out of the following scenarios. The larger coiling diameter could have increased the propagation losses due to side-core coupling for the fundamental

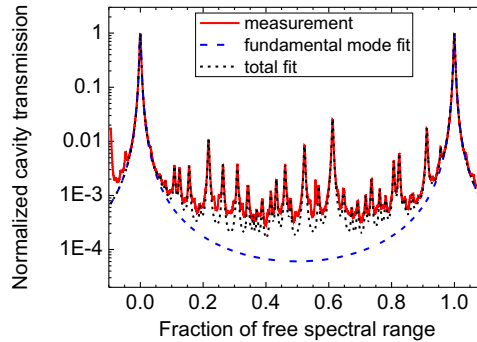


Figure 5.14: Representative mode scan results for 190 mW of amplifier seed power and a fiber coiling diameter of 45 cm, measured at 1.8 W of total amplifier output, corresponding to 88 % fundamental mode content. The cavity mode at ~ 0.61 FSR was still predominant, but the power fraction in some other cavity HOMs increased compared to the results obtained with a smaller coiling diameter.

mode. Furthermore, the losses caused by fiber bending and side-core coupling could have decreased for potentially emitted HOMs. Another possibility is that the smaller coiling diameter pushed these HOMs away from the fiber core center, decreasing the overlap with the doped region and thus their amplification.

A final conclusion about the suitability of $55\ \mu\text{m}$ core diameter CCC fibers for the application in future GWD laser systems can not yet be drawn. The experimental results presented in this Section revealed that still a lot of work needs to be done regarding fiber design and drawing process. In particular, the overlap of a fiber's FM with the TEM_{00} mode should be considered for design optimization of an active LMA fiber. Effects such as fiber bending influence on modal shapes, propagation constants and overlap with the fundamental mode or doped region need to be investigated in order to understand the origin of the described observations. Moreover, the effect of surrounding a particular core design with a double- or triple-structure to guide the pump-light on the modal properties has to be considered. This is true not only for CCC fibers, but for all LMA fiber technologies. For the latest designs of very large mode area rod-type PCFs (i.e. large pitch fibers (LPF) [185, 208]), the designers have already started to consider the whole mode-set for the fiber instead of distinguishing core and cladding modes. This enabled a straight-forward delocalization of HOMs from the doped region.

6 Conclusion and outlook

Conceptual design studies for the 3rd generation of earth-based interferometric gravitational wave detectors (GWDs) indicate that a linearly-polarized single-frequency (SF) signal at 1064 nm with more than 500 W in the TEM₀₀ mode will most likely be required. To allocate such a laser signal, fiber amplifier systems seem to be the most promising approach. The major challenge in achieving the targeted parameters arises from the fact that conventional step-index fibers can only be operated effectively single-mode (SM) at 1064 nm up to mode field diameters (MFDs) of about 21 μm . SF amplifiers employing these fibers are in turn limited to output powers levels of less than 300 W by the nonlinear effect of stimulated Brillouin scattering (SBS), even if external mitigation techniques are applied.

To overcome this issue, specialty fibers have been developed. The most promising candidates to obtain effective SM operation of LMA fibers were and still are bendable photonic crystal fibers (PCFs) and chirally coupled core (CCC) fibers. More than 500 W of SF amplifier output has been demonstrated with these fibers, but the overlap with the TEM₀₀ mode overlap had not been investigated, yet. In fact, the CCC fiber design concept had not been characterized with TEM_{*nm*}-modal decomposition measurements at all.

The main goal of this thesis was thus to analyze the TEM₀₀ mode power extraction at 1064 nm from these fiber design concepts. To get a general idea about their modal decomposition with respect to the TEM_{*nm*} modes, passive versions were tested first. Their performance is also of interest when all-fiber system integration or the utilization of delivery fibers is considered. The tested fibers have up to now the largest core diameters and MFDs available of their design concept. For the PCF these were about 40 μm and 30 μm , respectively. The CCC fiber under test had an even larger core diameter of 55 μm , corresponding to a MFD of 42 μm . TEM₀₀ mode contents of more than 96 % could be obtained for both fibers. Moreover, they behaved like truly SM fibers, as the TEM₀₀ mode overlap was insensitive to the launching condition of the transmitted signal. For comparison, a 30 μm -core-diameter standard step-index fiber was analyzed. In this case, HOMs could get easily excited through external perturbation of the launching conditions. While the beam quality of the PCF was sensitive to the fiber end preparation, the TEM_{*nm*}-modal decomposition of the beam transmitted through the CCC fiber was not affected by any external perturbations. Consequently, it's best suitable as possible beam delivery fiber.

In amplifier operation of active fibers, the implications of gain as well as thermal issues need to be considered. Therefore, the measured TEM₀₀ mode overlap of the beams transmitted through the passive fibers cannot be conferred to its active counterparts. Their performance was tested in SF amplifier experiments. The most promising results were obtained with the active counterpart of the PCF. The measured TEM₀₀ mode overlap of the beam emitted from the fiber core was 92 % at a total amplifier output of 33 W. This value decreased only slightly to 91% at a total amplifier output of 246 W, yielding a record

SF 203 W TEM₀₀ mode power in linear polarization, after subtracting the unexpected high amount of power (9.5%) emitted from the cladding. After carrying out additional tests, this could be related to fiber anisotropies, originating from a non-optimized drawing process. As a crucial parameter to influence the TEM₀₀ mode overlap for this fiber, the size and shape of the fibers boron-doped stress rods were identified. They induced high birefringence to ensure linear polarization output, if the seed signal was launched in the proper fiber axis, yielding a PER of more than 20 dB at all power levels. Several monitoring measurements confirmed SBS-free operation, even at the highest output power level at about 300 W. The power scaling limitation of this particular amplifier was parasitic lasing processes, which could not be inhibited despite a lot of experimental effort. Nevertheless, much higher power scaling with this fiber is not expected, as Robin et al. have by now identified the SBS-threshold of a similar fiber, incorporating the same core design, to be around 420 W in SF amplifier operation [205].

With respect to the CCC fiber design concept, active fibers with MFDs of about 37 μm and 55 μm at 1064 nm signal wavelength were available. Both designs were not optimized, especially regarding the production process. The active counterpart of the 55 μm fiber was a prototype and not suitable for high power extraction due to enormous heating. Moreover, even the best mode-scan result of 93 % TEM₀₀ mode content, measured at 1.4 W of total amplifier output, did not meet the performance of its passive counterpart. At 4.6 W of amplifier output, the TEM₀₀ mode overlap had already decreased down to 89 %. Altogether, the experimental results obtained with this fiber revealed that still a lot of work needs to be invested into fiber design and production process until a final conclusion about the suitability for the application in future GWD laser systems of 55 μm core diameter CCC fibers can be drawn. As the TEM₀₀ mode overlap of the fiber's fundamental mode is apparently very sensitive to the core NA, special attention has to be given to the active doping of the fiber core, as it alters the core's refractive index. Additionally, the impact of surrounding a particular core design with a double- or triple-structure to guide the pump-light on the modal properties has to be considered. Moreover, the obtained results indicate that effects such as fiber bending influence on modal shapes, propagation constants and overlap with the doped region need to be investigated.

The 37 μm fiber core guided one HOM, which could not be suppressed anymore at a certain power level. As a consequence, TEM₀₀ mode power scaling in linear polarization was in this case limited to 182 W (230 W of total amplifier output) by the onset of a nonlinear effect, commonly referred to as transverse modal instabilities (TMI). In fact, first experimental evidence of TMI occurrence in a CCC fiber was obtained during the work for this thesis. Nevertheless, at amplifier power levels up to 103 W, an excellent overlap of the fiber's fundamental mode with the TEM₀₀ mode (95 %) was demonstrated. This shows the general potential for this fiber design, if the drawing process can be sufficiently optimized. Furthermore, some features that contribute to the general understanding of this fiber design concept's properties and are thus very useful for future design and production optimization, were identified. While the HOM suppression for a double-clad version of the fiber was rather sensitive to the pump power level and corresponding absorption, the

tested air-clad version's beam quality was prone to the total gain and inversion.

The phenomenon of TMI was discovered by several research groups simultaneously during the time the work for this thesis was carried out, and is currently still not fully understood. It manifests itself in a threshold-like onset of modal power fluctuations and turned out to be a major power scaling limitation for all LMA fiber designs. Consequently, investigations to understand the characteristics of the threshold and dynamics of this effect were carried out within the framework of this thesis. The first key result was the observation of a transient behavior below the TMI threshold. This strongly indicates the presence of a static grating, which enables modal power transfer, if the equilibrium state is perturbed by a transient as e.g. increasing the pump power. Furthermore, it was shown that no relevant decrease in the TEM₀₀ mode overlap of the amplifier output beam occurs below the TMI threshold, once the transient has decayed. To characterize TMI beyond the threshold power, a modified version of the utilized nonconfocal scanning ring cavity needs to be developed. Additionally, the frequency resolved intensity noise spectra below and above the threshold were measured for the first time directly, revealing two more key results. First of all, no periodic transition region between stable and chaotic modal power oscillations were observed. These observations indicate that the appearance of periodic oscillations are rather a characteristic of TMI in particular amplifier configurations than a general feature of TMI, as was previously suggested by other research groups. Moreover, higher and higher frequencies in the RIN spectra were measured with increasing amplifier power. This feature has only been captured by models based on stimulated thermal Rayleigh scattering (STRS). Contrary to the static grating models, this process requires a thermal equilibrium state and is based on a moving grating. Consequently, the experimental results presented in this thesis clearly demonstrate that there are several contributors to TMI in real world amplifiers. They assist to identify the abilities and limitations of the numerical models and underlying physical theories, currently discussed by the scientific community. Finally it was demonstrated with a fully degraded fiber that there is an ultimate lower TMI threshold, which can not be further lowered by external perturbations such as additional amplitude modulation of the pump- or seed-signal.

In order to push the SBS-limit of SF PCF amplifiers to higher power levels, Robin et al. have spent a lot of effort by now into developing advanced fiber designs. They incorporated an acoustic-velocity segmentation into the 40 μm PCF core design. 500 W of SF amplifier output have been demonstrated with that fiber design [184]. Further power scaling was limited by the onset of TMI. To overcome this issue, the acoustically-segmented fiber design was modified by tailoring the Yb-doped core to reduce the overlap of the HOM with the doped region. This led to a reduced absorption per meter and increased the fiber length necessary for a reasonable overall absorption. Unfortunately, this was associated with a lowered SBS power threshold and about 990 W of amplifier output could only be obtained with a broadened signal linewidth of 300 MHz, which is not sufficiently narrow for interferometric GWDs. Consequently, the ultimate power scaling limit of a SF signal in a single PCF amplifier will be a trade-off between SBS and TMI. This also implies that even though the understanding of the SBS process is very sophisticated, it is

still an issue, at least for the amplification of kHz-linewidth signals. Therefore, one aspect of SBS that had not been investigated before was analyzed within the framework of this thesis, namely the impact of ASE. Using an established numerical model it was shown that the SBS threshold of an amplifier is lower, if a term accounting for ASE is included in the differential equation for the SBS power. Using a passive fiber, the effect that explains this observation was demonstrated. ASE within the Brillouin gain bandwidth (BGBW), counter-propagating to the signal to be transmitted, can seed the SBS process and hence lower its power threshold. On the other hand it was confirmed that Rayleigh backscattered ASE from a preamplifier is not sufficient to significantly decrease the SBS threshold of the following amplification stage, as long as the seed has a signal-to-noise ratio of more than 15 dB (OSA resolution set to 0.5 nm). Altogether, the obtained results demonstrated that ASE photons within the BGBW and co-propagating to the Stokes signal that are generated in a fiber amplifier are more likely to decrease the SBS threshold than Rayleigh backscattered ASE photons, injected from a preamplifier. Therefore it is advisable to use higher seed power levels to increase the SBS threshold of a high power fiber amplifier. This also incorporates the advantage of a decreased sensitivity towards parasitic lasing processes.

Given the fiber technology's state of the art, the most promising approach to obtain 1 kW of a kHz-linewidth signal at 1064 nm, suitable for application in the third generation of earth-based interferometric GWDs is coherent beam combination of two PCF amplifiers. The fiber design should be based on acoustic segmentation. Whether additional gain-tailoring is necessary, will depend on the exact amplifier configuration, including seed power and fiber length. From the results presented in this thesis it can be anticipated that a TEM_{00} mode content of more than 90 % is expected from such a fiber if it incorporates the analyzed 40 μm core design. Especially considering the decrease in TEM_{00} mode content with increasing amplifier output power of the analyzed PCF, no significant beam quality degradation should occur as long as the amplifier operates below the TMI threshold. Special attention has to be drawn to the stress-rod design and anisotropies in the core should be inhibited as good as possible during the fabrication process. All in all, this thesis contributes largely to design fiber amplifier system for the next generation of GWDs, with targeted laser signal parameters as given in the "Einstein Telescope" design study [12].

List of acronyms

aLIGO	advanced LIGO
ASE	amplified spontaneous emission
BGBW	Brillouin gain bandwidth
BPM	beam propagation method
CCC	chirally coupled core
CW	continuous wave
DBB	diagnostic breadboard
DC	double-clad
DCM	dichroic mirror
DMF	distributed mode filter
ET	Einstein Telescope
FM	fundamental mode
FSM	fundamental space filling mode
FWHM	full width at half maximum
FWM	four-wave mixing
GWD	gravitational wave detector
HR	highly-reflective
HOM	higher order mode
LIGO	Laser Interferometer Gravitational-Wave Observatory
LMA	large mode area
LPF	large pitch fiber
MCVD	modified chemical vapor deposition
MFD	mode field diameter
MOPA	master-oscillator power-amplifier
MI	modal instabilities
NA	numerical aperture
NL	nonlinear
NPRO	nonplanar ring oscillator
OSA	optical spectrum analyzer
OVD	outside vapor deposition

List of acronyms - continued

PANDA	polarization-maintaining and absorption-reducing
PBG	photonic bandgap
PBS	polarizing beam splitter
PCF	photonic crystal fiber
PCVD	plasma-activated chemical vapor deposition
PER	polarization extinction ratio
PM	polarization-maintaining
PMD	polarization mode dispersion
PR	partial reflector
QPM	quasi phase matched
RBW	resolution bandwidth
RIN	relative intensity noise
SF	single-frequency
SM	single-mode
SMF	single-mode fiber
SBS	stimulated Brillouin scattering
SRS	stimulated Raman scattering
SNR	signal-to-noise ratio
STRS	stimulated thermal Rayleigh scattering
TIR	total internal reflection
TMI	transverse modal instabilities
TSHB	transverse spatial hole burning
VAD	vapor axial deposition
Yb	ytterbium

Bibliography

- [1] B. C. Barish. The detection of gravitational waves with LIGO. In *Proceedings of the Los Angeles Meeting - Division of Particles and Fields of the APS*, (American Physical Society, 1999), talk 14-12.
- [2] L. M. Krauss, S. Dodelson, and S. Meyer. Primordial gravitational waves and cosmology. *Science* 21, 328(5981):989–992, 2010.
- [3] B. F. Schutz. Gravitational wave astronomy. *Classical and Quantum Gravity*, 16(12A): A131–A156, 1999.
- [4] D. Sigg. Gravitational waves. In *Proceedings of TASI 98 (Theoretical Advanced Study Institute in Elementary Particle Physics)*, Publication LIGO-P980007-00 – D, 1998.
- [5] S. Rowan and J. Hough. Gravitational wave detection by interferometry (ground and space). *Living Reviews in Relativity*, 3(3):1–41, 2000.
- [6] S. Hild, S. Chelkowski, A. Freise, J. Franc, N. Morgado, R. Flaminio, and R. DeSalvo. A xylophone configuration for third generation gravitational wave detector. *Classical and Quantum Gravity*, 27(1):0150031–0150038, 2009.
- [7] J. Abadie et al. (the LIGO scientific collaboration and the Virgo scientific collaboration). Search for gravitational waves from low mass binary coalescence in LIGO’s sixth science run and Virgo’s science runs 2 and 3. *Physical Review D*, 85(8):0820021–08200212, 2012.
- [8] B. Willke. Stabilized lasers for advanced gravitational wave detectors. *Laser Photonics Review*, 4(6):780–794, 2010.
- [9] T. J. Kane and R. L. Byer. Monolithic, unidirectional single-mode Nd:YAG ring laser. *Optics Letters*, 10(2):65–67, 1985.
- [10] B. Willke, K. Danzmann, M. Frede, P. King, D. Kracht P. Kwee, O. Puncken, R. L. Savage (Jr.), B. Schulz, F. Seifert, C. Veltkamp, S. Wagner, P. Weßels, and L. Winkelmann. Stabilized lasers for advanced gravitational wave detectors. *Classical and Quantum Gravity*, 25(11):114040–114048, 2008.
- [11] L. Winkelmann, O. Puncken, R. Kluzik, C. Veltkamp, P. Kwee, C. Poeld, C. Bogan, B. Willke, M. Frede, J. Neumann, P. Weßels, and D. Kracht. Injection-locked single-frequency laser with an output power of 220 W. *Applied Physics B*, 102(3):529–538, 2011.

- [12] M. Abernathy et al. (the ET Science Team). The einstein gravitational wave telescope conceptual design study (No. 4). (ET-0106C-10), 2011.
- [13] J. E. Curtis and D. G. Grier. Structure of optical vortices. *Physical Review Letters*, 90(13):1339011–1339014, 2003.
- [14] L. Carbone, C. Bogan, P. Fulda, A. Freise, and B. Willke. Generation of high-purity higher-order Laguerre-Gauss beams at high laser power. *Physical Review Letters*, 110:2511011–2511015, 2013.
- [15] C. Wirth, O. Schmidt, A. Kliner, T. Schreiber, R. Eberhardt, and A. Tünnermann. High-power tandem pumped fiber amplifier with an output power of 2.9 kW. *Optics Letters*, 36(16):3061–3063, 2011.
- [16] J. P. Koplow, D. A. V. Kliner, and L. Goldberg. Single-mode operation of a coiled multimode fiber amplifier. *Optics Letters*, 25(7):442–442, 2000.
- [17] M.-J. Li, X. Chen, A. Liu, S. Gray, J. Wang, D. T. Walton, and L. A. Zenteno. Effective area limit for large mode area laser fibers. In *Optical Fiber Communication Conference/ National Fiber Optic Engineers Conference*, OSA Technical Digest (CD), (Optical Society of America, 2008), paper OTuJ2.
- [18] T. Theeg, H. Sayinc, J. Neumann, and D. Kracht. All-fiber counter-propagation pumped single frequency amplifier stage with 300-W output power. *IEEE Photonics Technology Letters*, 24(20):1864–1867, 2012.
- [19] Y. Jeong, J. Nilsson, J. K. Sahu, D. N. Payne, R. Horley, L. M. B. Hickey, and P. W. Turner. Power scaling of single-frequency ytterbium-doped fiber master-oscillator power-amplifier sources up to 500 W. *IEEE Journal of Selected Topics in Quantum Electronics*, 13(3):546–551, 2007.
- [20] C. Zhu, I. Hu, X. Ma, and A. Galvanauskas. Single-frequency and single-transverse mode Yb-doped CCC fiber MOPA with robust polarization SBS-free 511 W output. In *Advanced Solid-State Photonics*, OSA Technical Digest (CD), (Optical Society of America, 2011), paper AMC5.
- [21] C. Robin, I. Dajani, and F. Chiragh. Experimental studies of segmented acoustically tailored photonic crystal fiber amplifier with 494 W single-frequency output. In *Proceedings of SPIE Volume 7914, Fiber Lasers VIII: Technology, Systems and Applications*, pages 79140B1–79140B8, 2011.
- [22] S. Wielandy. Implications of higher-order mode content in large mode area fibers with good beam quality. *Optics Express*, 15(23):15402–15409, 2007.
- [23] M. Hildebrandt, M. Frede, P. Kwee, B. Willke, and D. Kracht. Single-frequency master-oscillator photonic crystal fiber amplifier with 148 W output power. *Optics Express*, 14(23):11071–11076, 2006.

- [24] C. Gréverie, A. Brillet, C. N. Man, W. Chaibi, J. P. Coulon, and K. Feliksik. High power fiber amplifier for Advanced Virgo. In *Conference on Lasers and Electro-Optics*, OSA Technical Digest (CD), (Optical Society of America, 2010), paper JTuD36.
- [25] T. Eidam, C. Wirth, C. Jauregui, F. Stutzki, F. Jansen, H.-J. Otto, O. Schmidt, T. Schreiber, J. Limpert, and A. Tünnermann. Experimental observations of the threshold-like onset of mode instabilities in high power fiber amplifiers. *Optics Express*, 19(14):13218–13224, 2011.
- [26] F. Stutzki, H.-J. Otto, F. Jansen, C. Gaida, C. Jauregui, J. Limpert, and A. Tünnermann. High-speed modal decomposition of mode instabilities in high-power fiber amplifiers. *Optics Letters*, 36(23):4572–4574, 2011.
- [27] A. V. Smith and J. J. Smith. Mode instability in high power fiber amplifiers. *Optics Express*, 19(11):10180–10192, 2011.
- [28] C. Jauregui, T. Eidam, H.-J. Otto, F. Stutzki, F. Jansen, J. Limpert, and A. Tünnermann. Physical origin of mode instabilities in high-power fiber laser systems. *Optics Express*, 20(12):12912–12925, 2012.
- [29] K. R. Hansen, T. T. Alkesjold, J. Broeng, and J. Lægsgaard. Theoretical analysis of mode instability in high-power fiber amplifiers. *Optics Express*, 21(2):1944–1971, 2013.
- [30] D. Marcuse. *Theory of Dielectric Optical Waveguides*. Academic Press Inc., 2nd edition, 1991.
- [31] D. Gloge. Weakly guiding fibers. *Applied Optics*, 10(10):2252–2258, 1971.
- [32] Govind P. Agrawal. *Nonlinear Fiber Optics*. Academic Press Inc., 3rd edition, 2001.
- [33] John A. Buck. *Fundamentals of Optical Fibers*. Wiley - Interscience, 2nd edition, 2004.
- [34] P. S. J. Russell. Photonic-crystal fibers. *Journal of Lightwave Technology*, 24(12):4729–4749, 2006.
- [35] H. J. Eichler, A. Fleischer, J. Kross, M. Krystek, H. Lang, H. Niedrig, H. Rauch, G. Schmahl, H. Schoenebeck, E. Sedlmayr, H. Weber, and K. Weber. *Bergmann - Schäfer: Lehrbuch der Experimentalphysik Band 3 - Optik*. Walter de Gruyter, 9th edition, 1993.
- [36] A. Tegtmeier Pedersen, L. Grüner-Nielsen, and K. Rottwitt. Measurement and modeling of low-wavelength losses in silica fibers and their impact at communication wavelength. *Journal of Lightwave Technology*, 27(10):1296–1300, 2009.
- [37] Georg A. Reider. *Photonik - Eine Einführung in die Grundlagen*. Springer-Verlag, 1st edition, 1997.

- [38] E. Snitzer. Cylindrical dielectric waveguide modes. *Journal of the Optical Society of America*, 51(5):491–498, 1961.
- [39] N. A. Mortensen, J. R. Folkenberg, M. D. Nielsen, and K. P. Hansen. Modal cutoff and the V parameter in photonic crystal fibers. *Optics Letters*, 28(20):1879–1881, 2003.
- [40] http://www.nufern.com/pam/optical_fibers/.
- [41] D. Marcuse. Loss analysis of single-mode fiber splices. *The Bell System Technical Journal*, 56:703–718, 1977.
- [42] I. P. Kaminow. Polarization in optical fibers. *IEEE Journal of Quantum Electronics*, 17(1):15–22, 1981.
- [43] N. Shibata, Y. Sasaki, K. Okamoto, and T. Hosaka. Fabrication of polarization-maintaining and absorption-reducing fibers. *IEEE Journal of Lightwave Technology*, 1(1):38–43, 1983.
- [44] J. Noda, K. Okamoto, and Y. Sasaki. Polarization-maintaining fibers and their applications. *IEEE Journal of Lightwave Technology*, 4(8):1071–1089, 1986.
- [45] L. Zenteno. High-power double-clad fiber lasers. *Journal of Lightwave Technology*, 11(9):1435–1446, 1993.
- [46] P. Urquhart. Review of rare earth doped fibre lasers and amplifiers. *IEE Proceedings*, 135(6):385–407, 1988.
- [47] H. M. Pask, J. L. Archambault, D. C. Hanna, L. Reekie, P. St. Russell, J. E. Townsend, and A. C. Tropper. Operation of cladding-pumped Yb³⁺-doped silica fibre lasers in 1 μ m region. *Electronics Letters*, 30(11):863–865, 1994.
- [48] D. J. Ottaway, P. J. Veitch, M. W. Hamilton, C. Hollitt, and J. Munch. A compact injection-locked Nd:YAG laser for gravitational wave detection. *IEEE Journal of Quantum Electronics*, 34(10):2006–2009, 1998.
- [49] V. I. Kovalev and R. G. Harrison. Diffraction limited output from a CW Nd:YAG master-oscillator/ power amplifier with fibre phase conjugate SBS mirror. *Optics Communications*, 166(1):89–93, 1999.
- [50] J. Limpert, F. Röser, S. Klingebiel, T. Schreiber, C. Wirth, T. Peschel, R. Eberhardt, and A. Tünnermann. The rising power of fiber lasers and amplifiers. *IEEE Journal of Selected Topics in Quantum Electronics*, 13(3):537–545, 2007.
- [51] S. D. Jackson and T. A. King. Theoretical modeling of Tm-doped silica fiber lasers. *Journal of Lightwave Technology*, 17(5):948–956, 1999.

- [52] S. D. Jackson and Y. Li. High-power broadly tunable Ho^{3+} -doped silica fibre laser. *Electronics Letters*, 40(23):1474–1475, 2004.
- [53] B. J. Ainslie, S. P. Craig, and S. T. Davey. The absorption and fluorescence spectra of rare earth ions in silica-based monomode fiber. *Journal of Lightwave Technology*, 6(2):287–293, 1988.
- [54] R. Paschotta, J. Nilsson, A. C. Tropper, and D. C. Hanna. Ytterbium-doped fiber amplifiers. *IEEE Journal of Quantum Electronics*, 33(7):1049–1056, 1997.
- [55] T.C. Newell, P. Peterson, A. Gavrielides, and M.P. Sharma. Temperature effects on the emission properties of Yb-doped optical fibers. *Optics Communications*, 273(1):256–259, 2007. ISSN 0030-4018.
- [56] R. Paschotta, J. Nilsson, R. P. Barber, J. E. Caplen, A. C. Tropper, and D. C. Hanna. Lifetime quenching in Yb doped fibres. *Optics Communications*, 136(5):375–378, 1997.
- [57] Dieter Meschede. *Optik, Licht und Laser*. Vieweg + Teubner, 3rd edition, 2008.
- [58] S. Magne, Y. Ouerdane, M. Druetta, J. P. Goure, P. Ferdinand, and G. Monnom. Cooperative luminescence in an ytterbium-doped silica fibre. *Optics Communications*, 111(3):310–316, 1994.
- [59] B. Schaudel, P. Goldner, M. Prassas, and F. Auzel. Cooperative luminescence as a probe of clustering in Yb^{3+} doped glasses. *Journal of Alloys and Compounds*, 300:443–449, 2000.
- [60] S. Unger, A. Schwuchow, S. Jetschke, V. Reichel, A. Scheffel, and J. Kirchhoff. Optical properties of Yb-doped laser fibers in dependence on codopants and preparation conditions. In *Proceedings of SPIE Vol. 6890 - Optical Components and Materials V*, pages 6890161–68901611, 2008.
- [61] D. Kleppner. Inhibited spontaneous emission. *Physical Review Letters*, 47(4):233–236, 1981.
- [62] N. P. Barnes and B. M. Walsh. Amplified spontaneous emission - Application to Nd:YAG lasers. *IEEE Journal of Quantum Electronics*, 35(1):101–109, 1999.
- [63] M. Blazek, S. Hartmann, A. Molitor, and W. Elsaesser. Unifying intensity noise and second-order coherence properties of amplified spontaneous emission sources. *Optics Letters*, 36(17):3455–3457, 2011.
- [64] Katsunari Okamoto. *Fundamentals of Optical Waveguides*. Academic Press Inc., 2nd edition, 2006.

- [65] M. J. Damzen, V. I. Vlad, V. Babin, and A. Mocofanescu. *Stimulated Brillouin Scattering - Fundamentals and Applications*. Institute of Physics Publishing, 1st edition, 2003.
- [66] R. W. Boyd. *Nonlinear Optics*. Academic Press Inc., 2 edition, 2003.
- [67] M. Niklès, L. Thévenaz, and P. A. Robert. Brillouin gain spectrum characterization in single-mode optical fibers. *Journal of Lightwave Technology*, 15(10):1842–1851, 1997.
- [68] J. Toulouse. Optical nonlinearities in fibers: Review, recent examples, and systems applications. *Journal of Lightwave Technology*, 23(11):3625–3641, 2005.
- [69] G. W. Faris, L. E. Jusinski, M. J. Dyer, W. K. Bischel, and A. P. Hickman. High-resolution Brillouin gain spectroscopy in fused silica. *Optics Letters*, 15(12):703–705, 1990.
- [70] X. P. Mao, R. W. Tkach, A. R. Chraplyvy, R. M. Jopson, and R. M. Derosier. Stimulated Brillouin threshold dependence on fiber type and uniformity. *IEEE Photonics Technology Letters*, 4(1):66–69, 1992.
- [71] N. A. Brilliant. Stimulated Brillouin scattering in a dual-clad fiber amplifier. *Journal of the Optical Society of America B*, 19(11):2551–2557, 2002.
- [72] S. Höfer, A. Liem, J. Limpert, H. Zellmer, A. Tünnermann, S. Unger, S. Jetschke, H.-R. Müller, and I. Freitag. Single-frequency master-oscillator fiber power amplifier system emitting 20 W of power. *Optics Letters*, 26(17):1326–1328, 2001.
- [73] A. Liem, J. Limpert, H. Zellmer, and A. Tünnermann. 100-W single-frequency master-oscillator fiber power amplifier. *Optics Letters*, 28(17):1537–1539, 2003.
- [74] S. Gray, A. Liu, D. T. Walton, J. Wang, M.-J. Li, X. Chen, A. B. Ruffin, J. A. DeMerrit, and L. A. Zenteno. 502 W, single-transverse mode, narrow linewidth, bidirectionally pumped Yb-doped fiber amplifier. *Optics Express*, 15(25):17044–17050, 2007.
- [75] M. D. Mermelstein. SBS threshold measurements and acoustic beam propagation modeling in guiding and antiguiding single mode optical fibers. *Optics Express*, 17(18):16225–16237, 2009.
- [76] I. Dajani, C. Vergien, C. Robin, and C. Zeringue. Experimental and theoretical investigations of photonic crystal fiber amplifier with 260 W output. *Optics Express*, 17(26):24317–24333, 2009.
- [77] A. Liu. Suppressing stimulated Brillouin scattering in fiber amplifiers using nonuniform fiber and temperature gradient. *Optics Express*, 15(3):977–984, 2007.

- [78] M. Hildebrandt, S. Büsche, P. Weßels, M. Frede, and D. Kracht. Brillouin scattering spectra in high-power single-frequency ytterbium doped fiber amplifiers. *Optics Express*, 16(20):15970–15979, 2008.
- [79] T. Kurashima, T. Horiguchi, and M. Tateda. Thermal effects of Brillouin gain spectra in single-mode fibers. *IEEE Photonics Technology Letters*, 2(10):718–720, 1990.
- [80] S. Le Floch and P. Cambon. Study of Brillouin gain spectrum in standard single-mode optical fiber at low temperatures (1.4–370 K) and high hydrostatic pressures (1–250 bars). *Optics Communications*, 219(1):395 – 410, 2003.
- [81] J. Hansryd, F. Dross, M. Westlund, P. A. Andrekson, and S. N. Knudsen. Increase of the SBS threshold in a short highly nonlinear fiber by applying a temperature distribution. *Journal of Lightwave Technology*, 19(11):1691–1697, 2001.
- [82] M. D. Mermelstein, A. D. Yablon, and C. Headley. Suppression of stimulated Brillouin scattering in an Er-Yb fiber amplifier utilizing temperature-segmentation. In *Optical Amplifiers and Their Applications*, OSA Technical Digest (CD), (Optical Society of America, 2005), paperTuD3.
- [83] N. Yoshizawa. Stimulated Brillouin scattering suppression by means of applying strain distribution to fiber with cabling. *Journal of Lightwave Technology*, 11(10):1518–1522, 1993.
- [84] L. Zhang, S. Cui, C. Liu, J. Zhou, and Y. Feng. 170 W, single-frequency, single-mode, linearly-polarized, Yb-doped all-fiber amplifier. *Optics Express*, 21(5):5456–5462, 2013.
- [85] K. Shiraki, M. Ohashi, and M. Tateda. SBS threshold of a fiber with a Brillouin frequency shift distribution. *Journal of Lightwave Technology*, 14(1):50–57, 1996.
- [86] P. D. Dragic, C. H. Liu, G. C. Papen, and A. Galvanauskas. Optical fiber with an acoustic guiding layer for stimulated Brillouin scattering suppression. In *Conference on Lasers and Electro-Optics (CLEO)*, OSA Technical Digest (CD), (Optical Society of America, 2005), paper CThZ3.
- [87] M.-J. Li, X. Chen, J. Wang, S. Gray, A. Liu, J. A. Demeritt, A. B. Ruffin, A. M. Crowley, D. T. Walton, and L. A. Zenteno. Al/Ge co-doped large mode area fiber with high SBS threshold. *Optics Express*, 15(13):8290–8299, 2007.
- [88] <http://www.laserline.de/LDM-diodenlaser-module-kompakt.html>.
- [89] E. Snitzer, H. Po, F. Hakimi, R. Tumminelli, and B. C. McCollum. Double clad, offset core Nd fiber laser. In *Optical Fiber Sensors*, Vol. 2 of OSA Technical Digest Series, (Optical Society of America, 1988), paper PD5.

- [90] K. Tankala, D. Guertin, J. Abramczyk, and N. Jacobson. Reliability of low-index polymer coated double-clad fibers used in fiber lasers and amplifiers. *Optical Engineering*, 50(11):1116071–1116078, 2011.
- [91] H. Zellmer, A. Tünnermann, H. Welling, and V. Reichel. Double-clad fiber laser with 30 W output power. In *Optical Amplifiers and Their Applications*, Vol. 16 of OSA Trends in Optics and Photonics Series, (Optical Society of America, 1997), paper FAW18.
- [92] C.-H. Liu, B. Ehlers, F. Doerfel, S. Heinemann, A. Carter, K. Tankala, J. Farroni, and A. Galvnauskas. 810W continuous-wave and single-transverse-mode fibre laser using 20 μm core Yb-doped double-clad fibre. *Electronics Letters*, 40(23):1471–1472, 2004.
- [93] A. A. Stolov, D. A. Simoff, and J. Li. Thermal stability of specialty optical fibers. *Journal of Lightwave Technology*, 26(20):3443–3451, 2008.
- [94] <http://www.fiberguide.com/product/high-power-fiber>.
- [95] <http://www.verrillon.com/products-optical-fiber-coatings.htm>.
- [96] J. K. Sahu, C. C. Renaud, K. Furusawa, R. Selvas, J. A. Alvarez-Chavez, D. J. Richardson, and J. Nilsson. Jacketed air-clad cladding pumped ytterbium-doped fibre laser with wide tuning range. *IEEE Electronics Letters*, 37(18):1116–1117, 2001.
- [97] W. J. Wadsworth, R. M. Percival, G. Bouwmans, J. C. Knight, T. A. Birks, T. D. Hedley, and P. St. J. Russell. Very high numerical aperture fibers. *IEEE Photonics Technology Letters*, 16(3):843–845, 2004.
- [98] W. J. Wadsworth, R. M. Percival, G. Bouwmans, J. C. Knight, and P. St. J. Russell. High power air-clad photonic crystal fibre laser. *Optics Express*, 11(1):48–53, 2003.
- [99] V. Kozlov and K. Bennett. Acrylate coated optical fibers for up to 200°C application temperatures. In *Advanced Photonics Congress*, OSA Technical Digest (online), (Optical Society of America, 2012), paper SW1E.2.
- [100] *Corning Mid-Temperature Specialty Optical Fibers Datasheet*. URL <http://www.corning.com/CMS/PictureDetail.aspx?id=15877>.
- [101] J. Limpert, T. Schreiber, A. Liem, S. Nolte, H. Zellmer, T. Peschel, V. Guyenot, and A. Tünnermann. Thermo-optical properties of air-clad photonic crystal fiber lasers in high power operation. *Optics Express*, 11(22):2982–2990, 2004.
- [102] D. Machewirth, V. Khitrov, U. Manyam, K. Tankala, A. Carter, J. Abramczyk, J. Farroni, D. Guertin, and N. Jacobson. Large mode area double clad fibers for pulsed and CW lasers and amplifiers. In *Proceedings of SPIE Volume 5335, Fiber Lasers: Technology, Systems and Applications*, pages 140–150, 2004.

- [103] M. E. Fermann. Single-mode excitation of multimode fibers with ultrashort pulses. *Optics Letters*, 23(1):52–54, 1998.
- [104] D. Marcuse. Field deformation and loss caused by curvature of optical fibers. *Journal of the Optical Society of America*, 66(4):311–320, 1976.
- [105] J. Sakai and T. Kimura. Bending loss of propagation modes in arbitrary-index profile optical fibers. *Applied Optics*, 17(10):1499–1506, 1978.
- [106] M.-Y. Cheng, K.-C. Hou, A. Galvanauskas, D. Engin, R. Changkakoti, and P. Mamidipudi. High average power generation of single-transverse mode MW-peak power pulses using 80- μm core Yb-doped LMA fibers. In *Conference on Lasers and Electro-Optics/ Quantum Electronics and Laser Science Conference (CLEO/QELS)*, Technical Digest (CD), (Optical Society of America, 2006), paper CThAA3.
- [107] Z. Jiang and J. R. Marciante. Impact of transverse spatial hole burning on beam quality in large-mode-area Yb-doped fibers. *Journal of the Optical Society of America B*, 25(2):247–254, 2008.
- [108] J. C. Knight, T. A. Birks, P. St. J. Russell, and D. M. Atkin. All-silica single-mode optical fiber with photonic crystal cladding. *Optics Letters*, 21(19):1547, 1996.
- [109] J. C. Knight, J. Broeng, T. A. Birks, and P. St. J. Russell. Photonic band gap guidance in optical fibers. *Science*, 282:1476–1478, 1998.
- [110] T. A. Birks, J. C. Knight, and P. St. J. Russell. Endlessly single-mode photonic crystal fiber. *Optics Letters*, 22(13):961–963, 1997.
- [111] N. A. Mortensen, M. D. Nielsen, J. R. Folkenberg, A. Petersson, and H. R. Simonsen. Improved large-mode-area endlessly single-mode photonic crystal fibers. *Optics Letters*, 28(6):393–395, 2003.
- [112] M. Koshiba and K. Saitoh. Applicability of classical optical fiber theories to holey fibers. *Optics Letters*, 29(15):1739–1741, 2004.
- [113] M. Kashiwagi, K. Saitoh, K. Takenaga, S. Tanigawa, S. Matsuo, and M. Fujimaki. Effectively single-mode all-solid photonic bandgap fiber with large effective area and low bending loss for compact high-power all-fiber lasers. *Optics Express*, 20(14):15061–15070, 2012.
- [114] S. Février, D. A. Gaponov, P. Roy, M. E. Likhachev, E. M. Dianov, M. Y. Salganskii, M. V. Yashkov, A. N. Guryanov, L. Daniault, M. Hanna, F. Druon, and P. Georges. All-silica photonic bandgap fiber oscillators and amplifiers. In *Proceedings of Optical Fiber Communication Conference/ National Fiber Optic Engineers Conference*, OSA Technical Digest (CD), (Optical Society of America, 2011), paper OTuC4.

- [115] C. Lecaplain, A. Hideur, S. Février, and P. Roy. Mode-locked Yb-doped Bragg fiber laser. *Optics Letters*, 34(18):2879–2881, 2009.
- [116] S. Février, R. Jamier, J.-M. Blondy, S. L. Semjonov, M. E. Likhachev, M. M. Bubnov, E. M. Dianov, V. F. Khopin, M. Y. Salganskii, and A. N. Guryanov. Low-loss single-mode large mode area all-silica photonic bandgap fiber. *Optics Express*, 14(2):562–569, 2006.
- [117] D. A. Gaponov, S. Février, M. Devautour, P. Roy, M. E. Likhachev, S. S. Aleshkina, M. Y. Salganskii, M. V. Yashkov, and A. N. Guryanov. Management of the high-order mode content in large (40 μm) core photonic bandgap Bragg fiber laser. *Optics Letters*, 35(13):2233–2235, 2010.
- [118] M. Kashiwagi, K. Saitoh, K. Takenaga, S. Tanigawa, S. Matsuo, and M. Fujimaki. Low bending loss and effective single-mode all-solid photonic bandgap fiber with an effective area of 650 μm^2 . *Optics Letters*, 37(8):1292–1294, 2012.
- [119] O. N. Egorova, D. A. Gaponov, N. A. Harchenko, A. F. Kosolapov, S. A. Letunov, A. D. Pryamikov, S. L. Semjonov, E. M. Dianov, V. F. Khopin, M. Y. Salganskii, A. N. Guryanov, and D. V. Kuksenkov. All-solid photonic bandgap fiber with large mode area and high order modes suppression. In *Conference on Lasers and Electro-Optics/Quantum Electronics and Laser Science Conference (CLEO/QELS)*, OSA Technical Digest (CD), (Optical Society of America, 2008), paper CTuMM3.
- [120] A. Baz, L. Bigot, G. Bouwmans, and Y. Quiquempois. Single-mode, large mode area, solid-core photonic bandgap fiber with hetero-structured cladding. *Journal of Lightwave Technology*, 31(5):830–835, 2013.
- [121] F. Kong, K. Saitoh, D. McClane, T. Hawkins, P. Foy, G. Gu, and L. Dong. All-solid photonic bandgap fiber with record mode area. In *Optical Fiber Communication Conference/National Fiber Optic Engineers Conference*, OSA Technical Digest (online), (Optical Society of America, 2013), paper OTh1J.2.
- [122] A. Tünnermann, S. Höfer, A. Liem, J. Limpert, M. Reich, F. Röser, T. Schreiber, H. Zellmer, T. Peschel, and V. Guyenot. Power scaling of high-power fiber lasers and amplifiers. *Laser Physics*, 15(1):101–117, 2005.
- [123] K. Saitoh, Y. Tsuchida, M. Koshihara, and N. A. Mortensen. Endlessly single-mode holey fibers: the influence of core design. *Optics Express*, 13(26):10833, 2005.
- [124] J. C. Knight, T. A. Birks, P. St. J. Russell, and J. P. de Sandro. Properties of photonic crystal fiber and the effective index model. *Optics Letters*, 15(3):748–751, 1998.
- [125] A. Ferrando, E. Silvestre, J. J. Miret, P. Andrés, and M. V. Andrés. Full-vector analysis of a realistic photonic crystal fiber. *Optics Letters*, 24(5):276–278, 1999.

- [126] K. Saitoh and M. Koshiba. Full-vectorial imaginary-distance beam propagation method based on a finite element scheme: Application to photonic crystal fibers. *IEEE Journal of Quantum Electronics*, 38(7):927–933, 2002.
- [127] K. Saitoh and M. Koshiba. Empirical relations for simple design of photonic crystal fibers. *Optics Express*, 13(1):267–274, 2005.
- [128] *Datasheet Corning HI 1060 FLEX*. URL http://www.corning.com/specialtymaterials/products_capabilities/specialty_fiber/high_index.aspx.
- [129] F. Poli, A. Cucinotta, D. Passaro, S. Selleri, J. Lægsgaard, and Jes Broeng. Single-mode regime in large-mode-area rare-earth-doped rod-type PCFs. *IEEE Journal of Selected Topics in Quantum Electronics*, 15(1):54–60, 2009.
- [130] X. Zhao, Y. Zheng, X. Liu, G. Zhou, Z. Liu, and L. Hou. Design of large-core single-mode Yb³⁺-doped photonic crystal fiber. *Optoelectronics Letters*, 8(3):0212–0215, 2012.
- [131] J. Limpert, A. Liem, M. Reich, T. Schreiber, S. Nolte, H. Zellmer, A. Tünnermann, J. Broeng, A. Petersson, and C. Jakobsen. Low-nonlinearity single-transverse-mode ytterbium-doped photonic crystal fiber amplifier. *Optics Express*, 12(7):1313–1319, 2004.
- [132] X. Zhao, Y. Zheng, X. Liu, S. Li, Y. Han, Z. Hou, N. Wang, and L. Hou. Modal cutoff in rare-earth-doped photonic crystal fibers with multi-layer air-holes missing in the core. *Optoelectronics Letters*, 9(3):0201–0203, 2013.
- [133] J. Limpert, T. Schreiber, S. Nolte, H. Zellmer, A. Tünnermann, R. Iliew, F. Lederer, J. Broeng, G. Vienne, A. Petersson, and C. Jakobsen. High-power air-clad large-mode-area photonic crystal fiber laser. *Optics Express*, 11(7):818–823, 2003.
- [134] J. C. Knight, T. A. Birks, R. F. Cregan, P. St. J. Russell, and J.-P. de Sandro. Large mode area photonic crystal fibre. *Electronics Letters*, 34(13):1347–1348, 1998.
- [135] J. Limpert, A. Liem, T. Schreiber, S. Nolte, H. Zellmer, A. Tünnermann, J. Broeng, A. Petersson, C. Jacobsen, H. Simonsen, and N. A. Mortensen. Extended large-mode-area single-mode microstructured fiber laser. In *Conference on Lasers and Electro-Optics/ International Quantum Electronics Conference and Photonic Applications Systems Technologies*, OSA Technical Digest (CD), (Optical Society of America, 2004), paper CMS6.
- [136] W. J. Wadsworth, J. C. Knight, and P. St. J. Russell. Large mode area photonic crystal fibre laser. In *Conference on Lasers and Electro-Optics (CLEO)*, Trends in Optics and Photonics Series Vol. 56, (Optical Society of America, 2001), paper CWC1.

- [137] N. A. Mortensen and J. R. Folkenberg. Low-loss criterion and effective area considerations for photonic crystal fibres. *Journal of Optics A: Pure Applied Optics*, 5(3): 163–167, 2003.
- [138] X. Ma, C.-H. Liu, G. Chang, and A. Galvanauskas. Angular-momentum coupled optical waves in chirally-coupled-core fibers. *Optics Express*, 19(27):26515–26528, 2011.
- [139] C.-H. Liu, G. Chang, N. Litchinitser, D. Guertin, N. Jacobsen, K. Tankala, and A. Galvanauskas. Chirally coupled core fibers at 1550-nm and 1064-nm for effectively single-mode core size scaling. In *Conference on Lasers and Electro-Optics/ Quantum Electronics and Laser Science Conference and Photonic Applications Systems Technologies*, OSA Technical Digest Series (CD), (Optical Society of America, 2007), paper CTuBB3.
- [140] U. Peschel, T. Peschel, and F. Lederer. A compact device for highly efficient dispersion compensation in fiber transmission. *Applied Physics Letters*, 67(15):2111–2113, 1995.
- [141] R. A. Beth. Mechanical detection and measurement of the angular momentum of light. *Physical Review Letters*, 50(2):115–125, 1936.
- [142] L. Allen, M. W. Beijersbergen, R. J. C. Spreeuw, and J. P. Woerdman. Orbital angular momentum of light and the transformation of Laguerre-Gaussian laser modes. *Physical Review A*, 45(11):8185–8190, 1992.
- [143] C.-H. Liu, G. Chang, N. Litchinitser, A. Galvanauskas, D. Guertin, N. Jacobsen, and K. Tankala. Effectively single-mode chirally-coupled core fiber. In *Advanced Solid-State Photonics*, OSA Technical Digest Series (CD) (Optical Society of America, 2007), paper ME2.
- [144] I. V. Basistiy, M. S. Soskin, and M. V. Vasnetsov. Optical wavefront dislocations and their properties. *Optics Communications*, 119(5):604–612, 1995.
- [145] L. Marrucci, C. Manzo, and D. Paparo. Optical spin-to-orbital angular momentum conversion in inhomogeneous anisotropic media. *Physical Review Letters*, 96(16): 1639051–1639054, 2006.
- [146] J. F. Nye and M. V. Berry. Dislocations in wave trains. *Proceedings of the Royal Society of London A - Mathematical and Physical Sciences*, 336(1605):165–190, 1974.
- [147] V. Y. Bazhenov, M. V. Vasnetsov, and M. S. Soskin. Laser beams with screw dislocation in their wavefronts. *JETP Letters*, 52(8):429–431, 1990.
- [148] N. B. Baranova, A. V. Mamaev, N. F. Pilipetsky, V. V. Shkunov, and B. Y. Zel'dovich. Wave-front dislocations: topological limitations for adaptive systems with phase conjugation. *Journal of the Optical Society of America*, 73(5):525–528, 1983.

- [149] C. N. Pannell, P. St. Russell, and T. P. Newson. Stimulated Brillouin scattering in optical fibers: the effects of optical amplification. *Journal of the Optical Society of America B*, 10(4):684–690, 1993.
- [150] A. A. Fotiadi and R. V. Kiyani. Cooperative stimulated Brillouin and Rayleigh backscattering process in optical fiber. *Optics Letters*, 23(23):1805–1807, 1998.
- [151] R. G. Smith. Optical power handling capacity of low loss optical fibers as determined by stimulated raman and brillouin scattering. *Applied Optics*, 11(11):2489–2494, 1972.
- [152] P. Kwee, F. Seifert, B. Willke, and K. Danzmann. Laser beam quality and pointing measurements with an optical resonator. *Review of Scientific Instruments*, 78(7):0731031–07310310, 2007.
- [153] A. E. Siegman. New developments in laser resonators. In *Proceedings of SPIE Vol. 1224, Optical Resonators*, pages 2–14, 1990.
- [154] J. W. Nicholson, A. D. Yablon, S. Ramachandran, and S. Ghalimi. Spatially and spectrally resolved imaging of modal content in large-mode-area fibers. *Optics Express*, 16(10):7233–7243, 2008.
- [155] Y. Z. Ma, Y. Sych, G. Onishchukov, S. Ramachandran, U. Peschel, B. Schmauss, and G. Leuchs. Fiber-modes and fiber-anisotropy characterization using low-coherence interferometry. *Applied Physics B*, 96(2–3):345–353, 2009.
- [156] D. B. S. Soh, J. Nilsson, S. Baek, C. Codemard, Y. Jeong, and V. Philippov. Modal power decomposition of beam intensity profiles into linearly polarized modes of multimode optical fibers. *Journal of the Optical Society of America A*, 21(7):1241–1250, 2004.
- [157] T. Kaiser, D. Flamm, S. Schröter, and M. Duparré. Complete modal decomposition for optical fibers using CGH-based correlation filters. *Optics Express*, 17(11):9347–9356, 2009.
- [158] M. Paurisse, Louis Lévêque, M. Hanna, F. Druon, and P. Georges. Complete measurement of fiber modal content by wavefront analysis. *Optics Express*, 20(4):4074–4084, 2012.
- [159] A.E. Siegman. *Lasers*. University Science Books, 1st edition, 1986.
- [160] H. Tünnermann, J. H. Pöld, J. Neumann, D. Kracht, B. Willke, and P. Weßels. Beam quality and noise properties of coherently combined ytterbium doped single frequency fiber amplifiers. *Optics Express*, 19(20):19600–19606, 2011.
- [161] H. Tünnermann, M. Karow, D. Kracht, J. Neumann, and P. Weßels. Fiber modes in non-confocal cavities. Accepted for *SPIE Photonics West 2014, Fiber Lasers XI: Technology, Systems, and Applications*, paper 8916-116.

- [162] *Datasheet DC-200/40-PZ-Si*. URL <http://nktphotonics.com/side5319.html>.
- [163] Z. Jiang and J. R. Marciante. Impact of transverse spatial-hole burning on beam quality in large-mode-area yb-doped fibers. *Journal of the Optical Society of America B*, 25(2):247–254, 2008.
- [164] N. Andermahr and C. Fallnich. Interaction of transverse modes in a single-frequency few-mode fiber amplifier caused by local gain saturation. *Optics Express*, 16(12):8678–8684, 2008.
- [165] A. S. Smith and J. J. Smith. Mode competition in high power fiber amplifiers. *Optics Express*, 19(12):11318–11329, 2011.
- [166] C. A. Codemard, J. K. Sahu, and J. Nilsson. Tandem cladding-pumping for control of excess gain in ytterbium-doped fiber amplifiers. *IEEE Journal of Quantum Electronics*, 46(12):1860–1869, 2010.
- [167] T. Eidam, S. Hädrich, F. Jansen, F. Stutzki, J. Rothhardt, H. Carstens, C. Jauregui, J. Limpert, and A. Tünnermann. Preferential gain photonic-crystal fiber for mode stabilization at high average powers. *Optics Express*, 19(9):8656–8661, 2011.
- [168] J. W. Arkwright, P. Elango, G. R. Atkins, T. Whitbread, and M. J. F. Digonnet. Experimental and theoretical analysis of the resonant nonlinearity in ytterbium doped fiber. *Journal of Lightwave Technology*, 16(5):798–806.
- [169] M. K. Davis, M. J. F. Digonnet, and R. H. Pantell. Thermal effects in doped fibers. *Journal of Lightwave Technology*, 16(6):1013–1023.
- [170] F. Jansen, F. Stutzki, H.-J. Otto, T. Eidam, A. Liem, C. Jauregui, J. Limpert, and A. Tünnermann. Thermally induced waveguide changes in active fibers. *Optics Express*, 20(4):3997–4008, 2012.
- [171] K. R. Hansen, T. T. Alkeskjold, J. Broeng, and J. Lægsgaard. Thermo-optical effects in high-power ytterbium-doped fiber amplifiers. *Optics Express*, 19(24):23965–23980, 2011.
- [172] J. M. Fini. Large mode area fibers with asymmetric bend compensation. *Optics Express*, 19(22):21866–21873, 2011.
- [173] C. Wirth, T. Schreiber, M. Rekas, I. Tsybin, T. Peschel, R. Eberhardt, and A. Tünnermann. High-power linear-polarized narrow linewidth photonic crystal fiber amplifier. In *Proceedings of SPIE Vol. 7580*, pages 75801H1–75801H6, 2010.
- [174] O. Schmidt, M. Rekas, C. Wirth, J. Rothhardt, S. Rhein, A. Kliner, M. Strecker, T. Schreiber, J. Limpert, R. Eberhardt, and A. Tünnermann. High power narrow-band fiber-based ASE source. *Optics Express*, 19(5):4421–4427, 2011.

- [175] T. Eidam, S. Hanf, E. Seise, T. V. Andersen, T. Gabler, C. Wirth, T. Schreiber, J. Limpert, and A. Tünnermann. Femtosecond fiber CPA system emitting 830 W average output power. *Optics Letters*, 35(2):94–96, 2010.
- [176] C. Jauregui, H.-J. Otto, F. Jansen, F. Stutzki, T. Eidam, J. Limpert, and A. Tünnermann. Mode instabilities: physical origin and mitigation strategies. In *Proceedings of SPIE Vol. 8601, Fiber Lasers X: Technology, Systems, and Applications*, pages 8601F1–8601F6, 2013.
- [177] M. Laurila, M. M. Jørgensen, K. R. Hansen, T. T. Alkeskjold, J. Broeng, and J. Lægsgaard. Distributed mode filtering rod fiber amplifier delivering 292 W with improved mode stability. *Optics Express*, 20(5):5742–5753, 2012.
- [178] M. M. Jørgensen, M. Laurila, D. Noordegraaf, T. T. Alkeskjold, and J. Lægsgaard. Thermal-recovery of modal instability in rod fiber amplifiers. In *Proceedings of SPIE Volume 8601, Fiber Lasers IX: Technology, Systems and Applications*, pages 86010U1–86010U8, 2013.
- [179] H.-J. Otto, C. Jauregui, F. Stutzki, F. Jansen, J. Limpert, and A. Tünnermann. Mitigation of mode instabilities by dynamic excitation of fiber modes. In *Proceedings of SPIE Vol. 8601, Fiber Lasers X: Technology, Systems and Applications*, pages 86010A1–86010A7, 2013.
- [180] N. Haarlammert, O. de Vries, A. Liem, A. Kliner, T. Peschel, T. Schreiber, R. Eberhardt, and A. Tünnermann. Build up and decay of mode instability in a high power fiber amplifier. *Optics Express*, 20(12):13274–13283.
- [181] H.-J. Otto, F. Stutzki, F. Jansen, T. Eidam, C. Jauregui, J. Limpert, and A. Tünnermann. Temporal dynamics of mode instabilities in high-power fiber lasers and amplifiers. *Optics Express*, 20(14):15710–15722, 2012.
- [182] F. Jansen, F. Stutzki, H.-J. Otto, C. Jauregui, J. Limpert, and A. Tünnermann. High-power thermally guiding index-antiguinding-core fibers. *Optics Letters*, 38(4):510–512, 2013.
- [183] B. Ward, C. Robin, and I. Dajani. Origin of modal instabilities in large mode area fiber amplifiers. *Optics Express*, 20(10):11407–11422, 2012.
- [184] C. Robin, I. Dajani, C. Zeringue, B. Ward, and A. Lanari. Gain-tailored SBS suppressing photonic crystal fibers for high power applications. In *Proceedings of SPIE Volume 8237, Fiber Lasers IX: Technology, Systems and Applications*, pages 82371D1–82371D9, 2012.
- [185] F. Stutzki, F. Jansen, T. Eidam, A. Steinmetz, C. Jauregui, J. Limpert, and A. Tünnermann. High average power large-pitch fiber amplifier with robust single-mode operation. *Optics Letters*, 36(5):689–691, 2011.

- [186] C. Jauregui, T. Eidam, J. Limpert, and A. Tünnermann. The impact of modal interference on the beam quality of high-power fiber amplifiers. *Optics Express*, 19(4):3258–3271, 2011.
- [187] K. R. Hansen, T. T. Alkesjkold, J. Broeng, and J. Lægsgaard. Thermally induced mode coupling in rare-earth doped fiber amplifiers. *Optics Letters*, 37(12):2382–2384, 2012.
- [188] C. Jauregui, T. Eidam, H.-J. Otto, F. Stutzki, F. Jansen, J. Limpert, and A. Tünnermann. Temperature-induced index gratings and their impact on modal instabilities in high-power fiber laser systems. *Optics Express*, 20(11):440–451, 2012.
- [189] A. V. Smith and J. J. Smith. Increasing mode instability thresholds of fiber amplifiers by gain saturation. *Optics Express*, 21(13):15168–15182, 2013.
- [190] S. Naderi, I. Dajani, T. Madden, and C. Robin. Investigations of modal instabilities in fiber amplifiers through detailed numerical simulations. *Optics Express*, 21(13):16111–16129, 2013.
- [191] B. G. Ward. Modeling of transient modal instability in fiber amplifiers. *Optics Express*, 21(10):12053–12067, 2013.
- [192] A. V. Smith and J. J. Smith. Influence of pump and seed modulation on the mode instability thresholds of fiber amplifiers. *Optics Express*, 20(22):24545–24558, 2012.
- [193] A. Smith and J. J. Smith. Review of models of mode instability, 2013. URL www.as-photonics.com.
- [194] L. Dong. Stimulated thermal Rayleigh scattering in optical fibers. *Optics Express*, 21(3):2642–2656, 2013.
- [195] A. V. Smith and J. J. Smith. Mode instability thresholds of fiber amplifiers. In *Proceedings of SPIE Vol. 8601, Fiber Lasers X: Technology, Systems and Applications*, pages 8601081–8601086, 2013.
- [196] I.-N. Hu, C. Zhu, C. Zhang, A. Thomas, and A. Galvanauskas. Analytical time-dependent theory of thermally-induced modal instabilities in high power fiber amplifiers. In *Proceedings of SPIE Vol. 8601, Fiber Lasers X: Technology, Systems and Applications*, pages 8601091–8601099, 2013.
- [197] A. V. Smith and J. J. Smith. Modeled fiber amplifier performance near the mode instability threshold. arXiv:1301.4278, 2013. URL <http://arxiv.org/abs/1301.4278>.
- [198] H.-J. Otto, F. Stutzki, F. Jansen, T. Eidam, C. Jauregui, J. Limpert, and A. Tünnermann. Experimental study of mode instabilities in high power fiber amplifiers. In

Lasers, Sources, and Related Photonic Devices, OSA Technical Digest (CD), (Optical Society of America, 2012), paper AM4A.5.

- [199] <http://www.nktphotonics.com>.
- [200] H. Tünnermann, J. Neumann, D. Kracht, and P. Weßels. Gain dynamics and refractive index changes in fiber amplifiers: a frequency domain approach. *Optics Express*, 20(12):13539–13550, 2012.
- [201] H.-J. Otto, C. Jauregui, F. Stutzki, F. Jansen, J. Limpert, and A. Tünnermann. Controlling mode instabilities by dynamic mode excitation with an acousto-optic deflector. *Optics Express*, 21(14):17285–17298, 2013.
- [202] C. Robin. personal communication.
- [203] A. V. Smith and J. J. Smith. Frequency dependence of mode coupling gain in Yb doped fiber amplifiers due to stimulated thermal Rayleigh scattering. arXiv:1301.4277, 2013. URL <http://arxiv.org/abs/1301.4277>.
- [204] T. Theeg, H. Sayinc, J. Neumann, L. Overmeyer, and D. Kracht. Fiber integrated ytterbium single frequency amplifier with a measured fundamental mode power content of 91 % at 215 W. In *Workshop on Specilaty Optical Fibers and their Applications*, OSA Technical Digest (CD), (Optical Society of America, 2013), paper W3.33.
- [205] C. Robin, I. Dajani, C. Vergien, C. Zeringue, and T. M. Shay. Experimental and theoretical studies of single frequency PCF amplifier with output of 400 W. In *Proceedings of SPIE Volume 7580, Fiber Lasers VII: Technology, Systems and Applications*, pages 75801I1–75801I11, 2010.
- [206] T. T. Alkeskjold. personal communication.
- [207] A. Galvanauskas. personal communication.
- [208] J. Limpert, F. Stutzki, F. Jansen, H.-J. Otto, T. Eidam, C. Jauregui, and A. Tünnermann. Yb-doped large pitch fibres: effective single-mode operation based on higher-order mode delocalisation. *Light: Science & Applications*, 1(4):e8, April 2012. URL <http://www.nature.com/lisa/journal/v1/n4/full/lisa20128a.html>. published online.

Publications in peer-reviewed journals

- [209] M. Schultz, H. Karow, O. Prochnow, D. Wandt, U. Morgner, and D. Kracht. All-fiber ytterbium femtosecond laser without dispersion compensation. *Optics Express*, 16(24):19562–19567, 2008.
- [210] M. Schultz, H. Karow, D. Wandt, U. Morgner, and D. Kracht. Ytterbium femtosecond fiber laser without dispersion compensation tunable from 1015 nm to 1050 nm. *Optics Communications*, 282(13):2567–2570, 2009.
- [211] M. Karow, C. Basu, D. Kracht, J. Neumann, and P. Weßels. TEM₀₀ mode content of a two stage single-frequency Yb-doped PCF MOPA with 246 W of output power. *Optics Express*, 20(5):5319–5324, 2012.
- [212] M. Karow, J. Neumann, D. Kracht, and P. Weßels. Impact of amplified spontaneous emission on Brillouin scattering of a single-frequency signal. *Optics Express*, 20(10):10572–10582, 2012.
- [213] M. Karow, H. Tünnermann, J. Neumann, D. Kracht, and P. Weßels. Beam quality degradation of a single-frequency Yb-doped photonic crystal fiber amplifier with low mode instability threshold power. *Optics Letters*, 37(20):4242–4244, 2012.

Publications in conference proceedings

- [214] H. Karow, M. Schultz, D. Wandt, and D. Kracht. Ytterbium Kurzpulsfaserlaser ohne Dispersionskompensation. In *DPG Frühjahrstagung - Fachverband Quantenoptik und Photonik*, (Deutsche Physikalische Gesellschaft, 2008), paper Q39.5.
- [215] M. Schultz, H. Karow, D. Wandt, U. Morgner, and D. Kracht. Wavelength tunable ytterbium fs-fiber-laser without dispersion compensation. In *3rd EPS-QEOD Europhoton Conference on Solid-State, Fiber and Waveguided Light Sources*, (European Physical Society, 2008), paper TUoD.6.
- [216] D. Kracht, M. Schultz, H. Karow, O. Prochnow, D. Wandt, and J. Neumann. Femtosecond Yb fiber lasers. In *LEOS 2009, 22nd annual meeting of the IEEE Lasers & Electro-Optics Society*, paper TuEE1 (invited).
- [217] H. Karow, M. Schultz, D. Wandt, U. Morgner, D. Kracht, and J. Neumann. Pulse dynamics of all-normal dispersion mode-locked ytterbium lasers. In *CLEO/Europe and EQEC*, OSA Technical Digest (CD), (Optical Society of America, 2009), paper CF-P25.
- [218] M. Karow, C. Basu, D. Kracht, J. Neumann, and P. Weßels. Single-frequency Yb-doped PCF MOPA with 294 W of output power for gravitational wave detection. In *CLEO/Europe and EQEC*, OSA Technical Digest (CD), (Optical Society of America, 2011), paper CJ7-4.
- [219] M. Karow, J. Neumann, D. Kracht, and P. Weßels. Investigations on the impact of amplified spontaneous emission on the Brillouin scattering of a single-frequency signal. In *Lasers, Sources, and Related Photonic Devices*, OSA Technical Digest (CD), (Optical Society of America, 2012), paper AM4A.7.
- [220] M. Karow, H. Tünnermann, J. Neumann, D. Kracht, and P. Weßels. Beam quality degradation of a strongly pumped Yb-doped photonic crystal fiber amplifier. In *5th EPS-QEOD Europhoton Conference on Solid-State, Fibre and Waveguide Coherent Light Sources*, (European Physical Society, 2012), paper ThP.29.
- [221] M. Karow, J. Neumann, D. Kracht, and P. Weßels. TEM₀₀ mode content measurements on a large core passive CCC fiber. In *5th EPS-QEOD Europhoton Conference on Solid-State, Fibre and Waveguide Coherent Light Sources*, (European Physical Society, 2012), paper TuP.27.
- [222] M. Karow, C. Zhu, D. Kracht, J. Neumann, A. Galvanauskas, and P. Weßels. Fundamental gaussian mode content measurements on active large core CCC fibers. In

- CLEO/Europe and EQEC*, OSA Technical Digest (CD), (Optical Society of America, 2013), paper CJ-1.6.
- [223] P. Weßels, M. Karow, V. Kuhn, M. Steinke, H. Tünnermann, D. Kracht, and J. Neumann. Single-frequency fiber amplifiers for gravitational wave detection. In *Conference on Lasers and Electro-Optics (CLEO)*, OSA Technical Digest (online), (Optical Society of America, 2013), paper CW3M.5 (invited).
- [224] P. Weßels, M. Karow, V. Kuhn, M. Steinke, H. Tünnermann, D. Kracht, and J. Neumann. Fiber amplifiers for gravitational wave detection. In *Conference on Lasers and Electro-Optics Pacific Rim (CLEO-PR)*, (IEEE, 2013), paper MA1-1 (invited).
- [225] H. Tünnermann, M. Karow, D. Kracht, J. Neumann, and P. Weßels. Fiber modes in non-confocal cavities. Accepted for *SPIE Photonics West 2014, Fiber Lasers XI: Technology, Systems, and Applications*, paper 8916-116.

Curriculum vitae

Personal Data

Name: Malte Karow
Date of birth: 25.06.1983
Place of birth: Stadthagen, Germany
Nationality: German

Education

07/1989 – 06/1993 Grundschule (elementary school) Garbsen-Mitte
07/1993 – 06/2002 Integrierte Gesamtschule
(integrated comprehensive school) Garbsen
06/2002 Abitur (German university entrance diploma)

University Education

10/2002 – 11/2008 Physics at the Leibniz Universität Hannover
11/2008 Degree “Diplom-Physiker”, title of the thesis
“Ytterbium-dotierte Ultrakurzpulsfaserlaser
ohne Dispersionskompensation mit spektralem Filter”

Professional Affiliations

04/2007 – 11/2008 Research assistant at the Laser Zentrum Hannover e. V.
12/2008 – 03/2009 Research scientist at the Laser Zentrum Hannover e. V.
Ultrafast photonics group
03/2009 – present Research scientist at the Laser Zentrum Hannover e. V.
Single-frequency lasers group

Studies Abroad

08/1999 – 07/2000 High-school year in Brockport, New York (USA)
08/2005 – 06/2006 2 semesters at the University of Bergen, Norway
within the European Socrates/Erasmus programs

Acknowledgement

I would like to take this chance to thank all the people, who have supported me on my way to realize my project and thus contributed to this thesis.

First of all, I recognize Prof. Karsten Danzmann for the supervision and evaluation of my work. Furthermore, I'd like to thank Prof. Uwe Morgner for the evaluation of this thesis as second examiner and Prof. Detlev Ristau for taking the chairmanship of the examination.

I acknowledge Dr. Dietmar Kracht for offering the opportunity to carry out my research at the Laser Zentrum Hannover e.V. Moreover, I recognize Dr. Jörg Neumann for the amendment of this thesis and all my publications, which highly improved my works.

Very special thanks go to Dr. Peter Weßels for being my advisor and scientific mentor, his patience and support, the acquisition of new fibers, the organization of the collaboration with the research group of Prof. Almantas Galvanauskas from the University of Michigan, and finally for giving freedom to my research activities to a large extent. I recognize Prof. Almantas Galvanauskas for the collaboration and the provision of the CCC fibers. Besides, I'd like to thank Dr. Dietmar Kracht, Dr. Jörg Neumann und Dr. Peter Weßels for enabling the participation at international conferences and for the visit of the Air Force Research Lab in Albuquerque, New Mexico. The discussions carried out at AFRL and the conferences truly inspired and motivated me anew.

Additional thanks go the whole development department of the Laser Zentrum for the good cooperation, the interesting discussions, the convenient working atmosphere and the commendable handling of a very personal issue. For explicit support in the laboratory, the provision of fiber components, the enjoyable working atmosphere in the office, as well as the amendment of publications and parts of this thesis I acknowledge Katharina Hausmann, Cheng Zhu, Xia Ruan, Henrik Tünnermann, Michael Steinke, Chandrajit Basu, Raphael Kluzik and Philipp Jahn.

Furthermore, I recognize all the people, who have been involved in accomplishing the promotion of the excellence cluster "Centre for Quantum Engineering and Space-Time Research" (QUEST). The work for this thesis was carried out within the framework of this project.

Besides, I'd like to acknowledge the people, whose contribution to this thesis was indirectly, but just as important. First of all, I thank my parents Elke und Uwe Karow for enabling my physics studies, my studies abroad and for their advise and support considering all important aspects of my life. Moreover, I thank my family and friends for their advise and encouragement, their exceptional handling of a special situation and the awesome times together. Finally, I thank my brother for being my brother.

Danksagung

Diese Stelle möchte dazu nutzen, mich bei allen Menschen zu bedanken, die mich auf meinem etwas ungewöhnlichen Weg zur Promotion begleitet und daher zum Gelingen dieser Dissertation beigetragen haben.

Zuerst gilt mein Dank Prof. Karsten Danzmann für die Betreuung und Begutachtung dieser Arbeit. Des Weiteren danke ich Prof. Uwe Morgner für die Übernahme des Korreferats und Prof. Detlev Ristau für Übernahme des Prüfungsvorsitzes.

Bei Dr. Dietmar Kracht möchte ich mich für die Möglichkeit zur Durchführung meiner Arbeiten am Laser Zentrum Hannover e.V. bedanken. Dr. Jörg Neumann danke ich für das Korrekturlesen dieser Dissertation und all meiner Veröffentlichungen, was sehr zum Gelingen dieser Arbeiten beigetragen hat.

Ein ganz besonderer Dank gilt Dr. Peter Weißels für die lehrreichen Diskussionen, seine Unterstützung und Geduld, die Beschaffung neuer Fasern, die Organisation einer Zusammenarbeit mit der Arbeitsgruppe von Prof. Almantas Galvanauskas der Universität Michigan, und letztlich für die doch weitestgehende Freiheit bei meinen Forschungsaktivitäten. Prof. Almantas Galvanauskas danke ich für die Zusammenarbeit und das Bereitstellen der CCC-Fasern.

Ferner danke ich Dr. Dietmar Kracht, Dr. Jörg Neumann und Dr. Peter Weißels für die Möglichkeit zur Teilnahme an internationalen Konferenzen, sowie den Besuch der Airforce Research Labs in Albuquerque, New Mexico. Die dort und auf den Konferenzen geführten Diskussionen haben mich immer wieder neu inspiriert und motiviert.

Der gesamten Entwicklungsabteilung des Laser Zentrums danke ich für die gute Zusammenarbeit, die interessanten Diskussionen, die angenehme Arbeitsatmosphäre und schließlich für den nicht selbstverständlichen und vorbildlichen Umgang mit einer sehr persönlichen Entscheidung. Für explizite Unterstützung im Labor, die Versorgung mit Faserkomponenten, die angenehme Büroatmosphäre, sowie das Korrekturlesen von Veröffentlichungen und einzelnen Abschnitten dieser Dissertation möchte ich mich bei Katharina Hausmann, Cheng Zhu, Xia Ruan, Henrik Tünnermann, Michael Steinke, Chandrajit Basu, Raphael Kluzik und Philipp Jahn bedanken.

Zudem bedanke ich mich bei allen, die zum Zustandekommen des Exzellenzclusters "Centre for Quantum Engineering and Space-Time Research" (QUEST) beigetragen haben, in dessen Rahmen diese Arbeiten durchgeführt wurden.

Während all die oben aufgeführten Menschen direkt zum Gelingen meiner Promotion beitragen konnten, haben einige Menschen einen indirekten und dennoch genauso wichtigen Beitrag dazu geleistet. Allen voran möchte ich meinen Eltern Elke und Uwe Karow für das Ermöglichen meines Studiums und der Auslandsaufenthalte, sowie ihren Rat und Rückhalt bei allen wichtigen Entscheidungen danken. Meiner Familie, meinen Freunden und insbesondere meinem Bruder danke ich für ihren Rat und ihre Motivation, ihren großartigen Umgang mit meiner ungewöhnlichen Situation und die schöne Freizeitgestaltung.